Graphene Travelling Wave Amplifier for Integrated Millimeter-Wave/Terahertz Systems

by

Naimeh Ghafarian

A thesis
presented to the University of Waterloo
in fulfillment of the
thesis requirement for the degree of
Doctor of Philosophy
in
Electrical and Computer Engineering

Waterloo, Ontario, Canada, 2018

Examining Committee Membership

The following served on the Examining Committee for this thesis. The decision of the Examining Committee is by majority vote.

External Examiner:	Mona Jarrahi Professor, Dept. of Electrical and Computer Engineering, University of California Los Angeles
Supervisor:	Safieddin Safavi-Naeini Professor, Dept. of Electrical and Computer Engineering, University of Waterloo
Supervisor:	Amir Hamed Majedi Professor, Dept. of Electrical and Computer Engineering, University of Waterloo
Internal Member:	Dayan Ban Professor, Dept. of Electrical and Computer Engineering, University of Waterloo
Internal Member:	Simarjeet Saini Associate Professor, Dept. of Electrical and Computer Engineering, University of Waterloo
Internal-External Member:	Zoran Miskovic Professor, Dept. of Applied Mathematics, University of Waterloo

I hereby declare that I am the sole author of this thesis. This is a true copy of the thesis, including any required final revisions, as accepted by my examiners.

I understand that my thesis may be made electronically available to the public.

Abstract

Terahertz (THz) technology offers exciting possibilities for various applications, including high resolution biomedical imaging, long-wavelength spectroscopy, security monitoring, communications, quality control, and process monitoring. However, the lack of efficient high power easy-to-integrate sources and highly sensitive detectors has created a bottleneck in developing THz technology. In an attempt to address this issue, this dissertation proposes a new type of graphene-based solid state travelling wave amplifier (TWA).

Inspired by the unique properties of electrons in graphene two-dimensional (2D) fluid, the author proposes a new type of TWA in which graphene acts as the sheet electron beam. These properties include higher mobility and drift velocity at room temperature, zero effective mass, relativistic behavior, and a truly 2D configuration. Since the plasma properties of 2D electron fluid become more pronounced as the effective mass of electrons decreases and electron mobility increases, THz devices based on graphene with massless quasiparticles significantly outperform those made of relatively standard semiconductor heterostructures. Another significant advantage of graphene over semiconductors is that while the high drift velocity and electron mobility of semiconductors 2D electron gas (2DEG) are achieved only at very low temperatures, graphene has high mobility and drift velocity at room temperature.

This thesis describes the theoretical and practical methods developed for the analysis, design, and fabrication of a graphene-based THz TWA. It investigates the interaction between the electromagnetic wave and the drifting plasma wave in graphene by two methods. In the first approach, electrons in graphene are modelled as a 2D Fermi liquid, and the hydrodynamic model derived from a relativistic fluid approach is used to find the conductivity. In the second approach, the travelling wave interaction is analyzed using a quantum mechanical model. The drifting Fermi distribution function is applied to the linear conductivity response function of graphene obtained from random phase approximation. The conductivity of graphene is obtained as a function of frequency, wave number, chemical potential, and drift velocity. The result is consistent with the hydrodynamic approach. Both methods show that negative conductivity, and thus gain, is obtained when the drift velocity is slightly greater than the phase velocity. It is shown that the two methods produce comparable results.

In the next step, a slow-wave grating structure is designed and an estimate of the actual gain is obtained for the proposed graphene TWA structures. The Floquet mode analysis of top grated slab and rectangular silicon waveguides is presented. Here, a new theoretical method is developed to accurately estimate the field distribution of the first

order space harmonic of a hybrid mode inside a periodic top-grated rectangular dielectric waveguide. This method gives explicit expressions for the interaction impedance of the slow wave grating structures that are then used to design the waveguide and the grating. To verify the proposed approximation method, the results obtained with this approach are compared with the simulation results.

Finally, a prototype structure is fabricated. The recipes developed for different parts of the structure are presented. These parts include: a nanometer size grating, a sub-millimeter dielectric waveguide, and biasing contacts on top of the graphene layer. The developed recipes ensure reliable fabrication processes for large-area graphene devices. In addition, two different methods used to fabricate long uniform gratings are compared. This work ends by showing the measurement results obtained for the fabricated devices.

Acknowledgements

I would like to thank my supervisors, Prof. Safieddin Safavi-Naeini and Prof. Hamed Majedi, for their patience, guidance and support. I would especially like to express my gratitude to Prof. Safavi-Naeini whose diverse and deep knowledge and intuition made my PhD studies a highly enriching experience. He gave me motivation and enough freedom to try and explore my ideas and pushed me forward in times of disappointment and when I doubted my work would have a successful outcome.

It is also my pleasure to thank my PhD committee members, Prof. Zoran Miskovic, Prof. Dayan Ban, Prof. Simarjeet Saini, and Prof. Sujeet Chauhuri. I sincerely appreciate Prof. Mona Jarrahi (University of California Los Angeles) for agreeing to be my external examiner.

I spent much of my PhD working at the Quantum Nano Center (QNC) fabrication facility. Starting with no experience, I learned a great deal from Dr. Nathan Fitzpatrik, Brian Goddard and Rod Salandanan. I am especially indebted to Dr. Mohsen Raeiszadeh who gave me far more help than I expected, and is the source for almost all I now know about fabrication. I am also indebted to Dr. Anita Fadavi, Dr. Hadi Amarloo and Dr. Nazy Ranjkesh for helping me through the fabrication challenges by sharing their valuable experiences.

I also would like to thank all of my friends and colleagues at the Center for Intelligent Antenna and Radio Systems (CIARS) with special thanks to: Dr. Aidin Taeb and Dr. Ahmad Ehsandar who kindly supported me not only technically with the VNA and milling machine systems and the design of the measurement holder, respectively but also by acting as my living reference book with their advices; Dr. Suren Gigoyan who kindly help me in the measurements; Dr. Behrooz Semnani for the fruitful discussions we have; Ardeshir Palizban and Mohammad Fereidani for their help and advice in the packaging; and Dr. Arash Rohani for the experience I gained in practical optics through projects we did together.

I also want to thank Mary McPherson not only for revising my thesis but also, and more importantly, for giving me the courage and confidence I needed for writing. Last but not least I want to thank all the friends who created joyful moments for me during the course of this PhD and made my life in Waterloo pleasant. Special thanks to my dearest friends Farinaz Forouzannia, Maryyeh Chehresaz, Elnaz Barshan, and Neda Mohammadizadeh.

Words cannot express the deep gratitude I have to my parents for the sacrifice they have made for me. I owe all my success and happiness to them. Then, there is the joy of my life and warm center of our family, my brother. Thank you for being there, Mehdi.

Dedicated to my parents;

Tayebeh Abdellahi and Mahmood Ghafarian.

Table of Contents

List of Figures

Chapter 1

Introduction

1.1 THz gap

The terahertz (THz) range of frequencies (0.1 to 10 THz; wavelengths of 3 mm down to 30μm) is a part of the electromagnetic spectrum that lies between microwave and infrared light. THz waves have unique properties. For example, THz radiation is non-ionizing, meaning that THz-radiation does not cause any changes in chemical structures. In addition, its absorption coefficient depends on the type of tissue and water concentration through which it is passed. Therefore, THz waves can be used instead of harmful X-rays for non-invasive medical and biological diagnostics. The unique THz spectral fingerprints of different explosives, and the semi-transparency of most non-metallic materials in the THz frequency region, make THz waves suitable for non-intrusive detection of explosives and metallic weapons. Moreover, THz waves can be used for secure high-speed telecommunications due to their high atmospheric absorption and wide bandwidth. THz waves are also attractive in astronomy. Atoms and molecules that are central to the understanding of star and planet formation as well as the evolution of matter in galaxies and the chemistry of interstellar clouds, have strong spectral signatures at THz frequencies [4]. Also, more than half of the cosmic background from the Big Bang is in the THz band. THz waves have been applied to identify explosives, reveal hidden weapons, check for defects in tiles on the space shuttle, and screen for skin cancer and tooth decay (Fig. 1.1).

Despite all of these fascinating features and potentially transformative applications, the THz band still remains largely out of reach for commercial applications. The main reasons are the lack of low cost and low complexity sources, amplifiers, and low noise receiver technology. At lower frequencies, oscillating circuits using high-speed transistors can efficiently

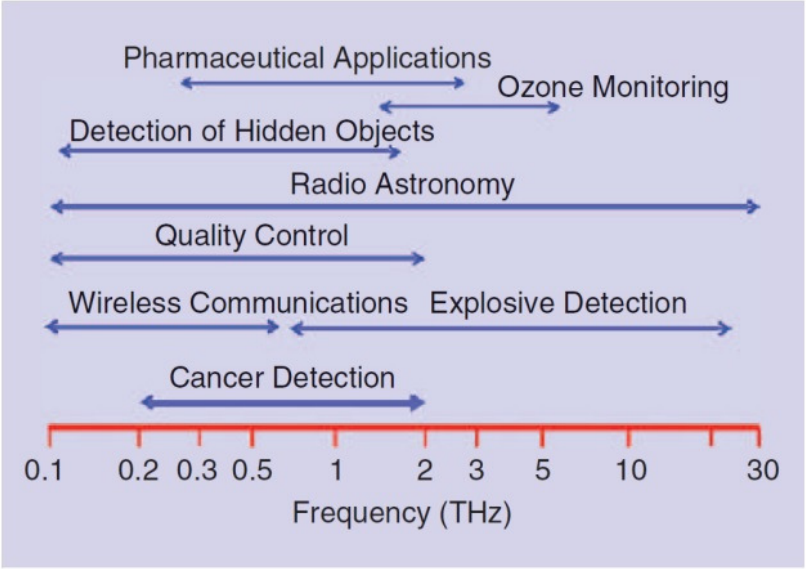

Figure 1.1: Applications of THz technology [1].

generate microwave radiation; however, transistors and other quantum devices based on electron transport have poor signal generation and low noise amplification performance. In addition, they become highly complex and costly at the sub-THz range of frequencies. In the infrared range of frequencies and higher, semiconductor lasers are satisfactory sources. The frequency of semiconductor lasers can be extended down to only around 30 THz [5]. Between these two well established technologies lies the so-called THz gap, where no semiconductor technology can efficiently convert electrical power into electromagnetic radiation.

1.2 THz sources

Currently available THz sources fall into four broad categories (Fig. 1.2):

1) Vacuum electronic devices (VEDs), including backward-wave oscillators, klystrons, grating-vacuum devices, travelling-wave tubes (TWTs), and gyrotrons. VEDs provide the highest power at lower THz frequencies ($< 0.7THz$). Realization of THz VED sources requires high bias voltages, precise and complex electromagnetic circuit fabrication, and high-quality electron beam generation and control. Thus, the highly complex fabrication process and large-vacuum packaging are the main challenges.

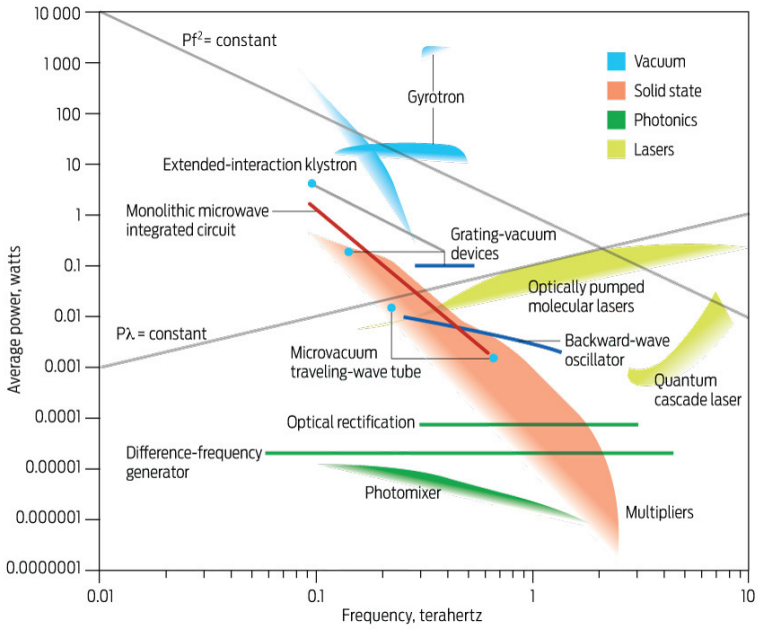

Figure 1.2: Compact THz sources. The Pf^2=constant line is the power-frequency slope expected for radio frequency devices; and the $P\lambda$=constant line is the expected slope for some commercial lasers [2].

2) Lasers, including free electron lasers, optically pumped molecular lasers (OPMLs), and quantum cascade lasers (QCLs). Lasers exhibit the highest average power at the upper THz frequencies. Free electron lasers are ideal THz sources because of their large bandwidth coherent high-power output. However, they are not portable, and large facilities are required. OPMLs are used for applications that require coherent radiation at the frequency range of 0.25 to 7.5 THz. Using advanced CO_2 lasers, radio frequency (RF) excitation, and cavity folding techniques, shoe-box sized reliable OPMLs can be constructed [6]. Since the majority of the pump radiation in OPMLs is converted to heat, the inherent efficiency of OPMLs is very low, typically $\sim 0.2\%$. The best efficiency reported is 1% [7]. OPMLs can work at room temperature. An output THz power of 100 mW is achievable with high power pump lasers.

QCLs provide narrow band high output power at frequencies above 2 THz. They require cryogenic cooling to achieve continuous wave operation. As a semiconductor laser, QCLs can be categorized as solid-state sources, with their size measured in millimeters. However, the overall packaging size is predominantly determined by cryogenic cooling requirements

[8, 9].

3) Semiconductor sources include harmonic frequency multipliers such as gallium arsenide (GaAs) Schot- tky diodes, Heterostructure Barrier Varactors (HBVs) and transistor-based frequency multipliers. Planar GaAs Schottky diode frequency multipliers can produce tens and even hundreds of microwatts of power at frequencies up to 2.7 THz [10] [11]. HBV-diode-based sources are the ones generally used at the lower end of the THz band. They can be used at the initial stages of a THz frequency multiplier chain. An output power and efficiency of 9.5 mW and 8%, respectively, at 300 GHz was reported for a tripler in [12]. With recent advances in device technologies, semiconductor integrated circuit amplifiers have reached operating frequencies of 1 THz [13]. These amplifiers include high electron mobility transistors (HEMTs), metamorphic HEMTs (mHEMTs), and heterojunction bipolar transistors (HBTs). The availability of THz transistors also means that one can design frequency multipliers with integrated power amplifiers working at THz frequencies.

4) Photonic sources use photodiodes and photoconductors, such as Uni-Travelling- Carrier (UTC) photodiodes and low-temperature-grown GaAs (LTG-GaAs) based photoconductors, as mixers to downconvert the optical signal to the THz band. Of the four main categories of THz sources, photonic sources have the lowest output level. However, very wide frequency bandwidth can be achieved with photonic approaches [14–17](Fig. 1.2).

The aforementioned sources each have their own advantages and disadvantages. Some are limited by their size, cost, or complexity; many are limited in output power or require cryogenic cooling and dedicated facilities. For example, THz tube sources have been the most important laboratory source at THz frequencies for high output powers and wide tuning ranges. However, they cannot be exploited in commercial applications mainly due to their size, cost and complexity. In terms of compactness and ease of integration, solid state and photonic sources are the best options. However, unlike lasers and VED sources, their output power levels are low, especially at frequencies close to or above 1 THz (Fig. 1.2).

Frequencies handled by traditional semiconductor amplifiers have been remarkably enhanced by the scaling of feature sizes, and are now approaching THz frequencies. The maximum frequency obtained to date in a conventional device is 1 THz, reached by a superscaled 25nm gate-length Indium phosphide (InP)HEMT. However, fundamental physical limitations mean the end of further scaling. Devices with small gate lengths show severe short-channel effects and large leakage currents. Therefore, smaller device feature sizes, required for higher frequency operation, reduce available power output. Thus, it is unlikely that transit time devices will achieve operation in the THz region with acceptable

performance. This limitation can be avoided by utilizing travelling wave interactions.

1.3 Semiconductor travelling wave amplifiers

The essential principle of TWA operation lies in the interaction between electron beams and EM waves. The EM waves must be slowed down to the same velocity as the electron beam. The electromagnetic field modulates the speed of the electrons in the electron beam; the electrons are no longer uniform and form electron bunches. The electron bunches react with the EM field, resulting in a net transfer of energy from the beam to the signal and thus amplification.

In TWTs, the electron beam is generated by an electron gun and then accelerated in a vacuum by a high electrical potential. Either solenoid electromagnets or permanent magnets are used around the tube to focus the electron beam. TWTs are characterized by high gain, high power capability, low noise, wide bandwidth, and large size.

Inspired by the success of TWTs , researchers investigated the amplification of electromagnetic waves by utilizing the coupling between an electromagnetic wave propagating in slow-wave circuits and the drifting plasma wave of carriers in semiconductors realized a semiconductor TWA [18–23]. A simple analysis of this device was introduced by Solymar et al. in 1966 [18]. This was a one-dimensional (1D) coupled mode analysis based on earlier analyses of vacuum TWTs presented by Pierce (1950) [24]. A three-dimensional (3D) analysis was presented by Sumi [20]. The first experimental evidence of this kind of interaction using n-type Indium Antimonide (InSb) semiconductors at 77K was reported in [25]. Another experiment using InSb and germanium (Ge) at 4.2K, was reported by Freeman et al. in 1973 [26].

In the first proposed semiconductor TWAs, the current-conducting semiconductor was placed in close proximity to an external slow-wave structure (usually a helix or metallic meander line) electrically insulated from the semiconductor. In these structures, the extremely small mechanical period of the external slow-wave circuit required for very high frequency operation is hard to achieve. In addition, the coupling between the current and the electromagnetic wave in such a structure is very weak. In 1974, Gover and Yariv proposed a different structure in which the current medium and the external slow-wave structure were integrated together in one monolithic semiconductor structure [27, 28]. The role of the external slow-wave structure is played by the semiconductor periodic corrugation. To obtain acceptable coupling, the current-conducting layer should be formed close to the corrugated surface. In [29], this structure was realized, and a 4 dB/cm electronic gain in a 1200 V/cm electric field at V-band was reported.

These studies conducted in the 1960s and 1970s did not lead to remarkable success, mainly due to the poor semiconductor technology available at that time. More recently, motivated by great successes in semiconductor technologies, similar solid-state TWAs were reconsidered [22] [23].

In [22] an interdigital-gated AlGaAs/GaAs HEMT structure was used to investigate the interaction between drifting carrier plasma waves and electromagnetic waves. In this structure, a two-dimensional (2D) electron gas (2DEG) is formed at the interface of an n-doped AlGaAs layer and an undoped GaAs layer. The interdigital slow-wave circuit is placed on top of the thin AlGaAs layer close to the current-conducting layer. The measured two-terminal admittance of the interdigital gate indicates the effect of interactions between the surface plasma waves of 2DEG carriers and EM waves at 5 and 10 GHz. Although the real part of the admittance tends to zero (no loss) if a biased voltage is applied, no actual gain (negative conductance) is observed in measurements, unlike in theoretical results. This inconsistency comes from ignoring the metallic loss and non-uniformity of drift velocity in the theoretical analysis.

In [23], an AlGaAs/GaAs heterostructure was made in a small chip that was then inserted into a GaAS rod waveguide. The slow-wave periodic structure was built monolithically on the top of the heterostructure device. The structure is very similar to what was proposed by Gover et al. [27]. A maximum gain of 8 dB/cm was measured in a 150 V/cm electric field at 70.2 GHz with a 2.6 mm-long chip with a 0.3 μm grating period.

In this thesis, a new TWA is proposed, in which a graphene layer is used instead of a heterostructure semiconductor to generate 2DEG. To explain the advantages of graphene as a promising material for THz TWAs, an introduction to graphene and its properties is provided below. Chapter 2 presents a thorough comparison between semiconductor 2DEGs and graphene 2DEGs.

1.3.1 Graphene

Graphene is a monolayer allotrope of carbon atoms with a 2D honeycomb lattice. Although graphene (or 2D graphite) has been studied theoretically for more than sixty years, it was only in 2004 that Novoselov et al. produced single layer graphene from the micromechanical cleavage of graphite. Graphene is the building block of other carbon allotropes such as nondimensional (0D) fullerenes, 1D nanotubes and 3D graphite. Its characteristics form the basis for understanding the electronic properties in these allotropes.

The dispersion relation of electrons in graphene was first calculated within tight-binding approximation in 1947 [30]. As a consequence of the high symmetry of honeycomb lattice,

the band structure for graphene at low energies has a linear conical shape. Moreover, in graphene, the conduction and valence bands touch each other at the Dirac points. Therefore, graphene can be considered as a zero-band-gap semiconductor. Its linear band structure is considerably different from the parabolic-band structures in conventional semiconductors. The most important graphene properties originate from this linear electronic band structure. While in standard conductors, charge carriers obey Schrodingers equation, the electron transport in graphene is governed by the Dirac equation. The charge carriers in graphene mimic chiral relativistic particles with zero rest mass and an energy-independent Fermi velocity that is approximately 300 times smaller than the speed of light.

Graphene is a zero overlap semimetal in which the charge carriers with concentrations of up to $10^{13} cm^{-2}$ and a room temperature carrier mobility of $\sim 20,000 cm^2/Vs$ are routinely observed. The carrier mobility in graphene is weakly temperature-dependent. Therefore, if impurity scattering was reduced, a high mobility of $\sim 200,000 cm^2/Vs$ could be achieved. This mobility is higher than that of any other known material [31,32]. A carrier mobility of up to 120,000 cm^2/Vs has been observed in suspended graphene samples at 240 K [33]. The absence of backscattering, weak electron-acoustic-phonon coupling, and the near-absence of point disorder in the graphene lattice contribute to graphene's high mobility [34]. Graphene can sustain current densities of $5 \times 10^8 A/cm^2$, and has extremely high thermal conductivity, up to 5000 W/m K at room temperature, 20 times higher than that of copper [35]. Despite being only one atomic layer thick, graphene is the strongest material ever tested due to its robust symmetric network of σ bonds [36]. Furthermore, this single atomic layer can absorb nearly 2.3% of light in the visible range. Graphene shows remarkable optical nonlinearities [37, 38], with ultrafast response times and a broadband spectral range.

Having all these remarkable properties makes graphene a unique material. Since 2004, its study has become an active field of research with many promising applications, including as an energy storage material in supercapacitors, for flexible transparent conducting electrodes in touchscreens and photovoltaic cells, and in low-loss tunable plasmonic devices in THz frequency. It can also be used in the realization of very high frequency transistors, ultra-wide band photodetectors, high speed modulators, and highly efficient electronic mixers. Many of these applications and even more are discussed in [39–41]. A brief introduction to graphene is presented in Chapter 2.

There are different methods for fabricating graphene: micromechanical cleavage, liquid-phase exfoliation, Chemical Vapour Deposition (CVD), carbon segregation, and chemical synthesis [42]. Micromechanical cleavage was the first method used to produce graphene. This method involves peeling off graphite by means of adhesive tape [43], and gives the best samples in terms of purity, defects, mobility and optoelectronic properties. Therefore, micromechanical cleavage provides a promising method to perform research on graphene prop-

erties. However, large-scale samples are not feasible with this method, and the graphene sheets obtained are less than a millimeter in size. Among the various methods, CVD is more often used to obtain large scale graphene sheets [44, 45].

1.4 Newly proposed graphene-based device

Inspired by the heightened properties of electrons in graphene 2DEG versus electrons in semiconductor 2DEG (e.g., higher mobility and drift velocity at room temperature, zero effective mass, truly 2D configuration), the author is proposing a new type of TWA in which graphene acts as the 2DEG medium. Since the plasma properties of 2DEG become more pronounced with a decreased effective mass of electrons and increased electron mobility, THz devices based on graphene with massless 2DEG significantly outperform those made of relatively standard semiconductor heterostructures. Another advantage of graphene over conventional semiconductor 2DEGs is that while the latter achieve high drift velocity and electron mobility only at very low temperatures, graphene 2DEGs have high mobility and drift velocity at room temperature.

The charged carriers in solid-state TWAs have a very low drift velocity and the phase velocity of the slow wave in the TWA should be matched with this low drift velocity. The low phase velocity results in a large propagation constant and consequently a large lateral decay constant. Therefore, decreasing the distance between the conducting layer (where the interaction and the energy exchange between the electromagnetic field and charged carriers occurs), and the grating surface (where the maximum field occurs), significantly increases the coupling and overall gain of the TWA. The monolithic semiconductor TWA proposed by Gover et al. is so far the best design in terms of the coupling between the electromagnetic wave and the conducting layer. In the new TWA proposed in this thesis, stronger coupling can be achieved by placing the conducting graphene layer right on top of the grating. Furthermore, the proposed structure has better performance and can work at room temperature.

In the proposed device, a silicon waveguide-based technology is adopted, newly developed for millimeter (mm)-wave and THz applications [46, 48]. It is integrated with a nano-scale grating etched on its top surface and covered with a DC-biased graphene sheet.

The fabrication of this structure consists of fabricating three integrated main structures: the grating [49–51], the graphene layer attached to DC bias contacts [52–55], and the silicon waveguide [56]. For each of these devices, different fabrication procedures have been introduced. In this thesis, for each of these three parts reliable fabrication recipes

are developed and combined to fabricate the first graphene TWA integrated in a mm-wave silicon waveguide.

1.5 Analysis of the grating structure

In the proposed TWA, the slow-wave field is generated by a dielectric grating waveguide. Therefore, part of this thesis is focused on developing a method for analysing and designing the grating structure. Gratings are present in many applications, ranging from microwave to optical frequencies. Based on the specific application, the gratings are designed to support either bounded surface waves (as in slow-wave structures, microwave or optical filters and distributed feedback reflectors in lasers), or to support unbounded leaky waves (as in travelling-wave antennas and optical periodic couplers). Therefore, various methods have been developed to study grating structures.

These methods can be divided mainly into two categories: numerical methods such as Finite Difference Time Domain (FDTD) [57], Finite Element Method (FEM) [58, 59], and Method of Moment (MoM) [60]; and semi-analytical methods such as transverse resonance technique [61–64], modal analysis [65–67], and coupled-mode theory [68, 69]. Accurate evaluation of practical grating configurations requires a full-wave numerical approach. However, rigorous numerical methods are computationally complex (CPU time and memory requirement). Both FDTD and FEM require the entire solution space to be discretized, whereas, the MoM method requires discretization of only surface unknown quantities (equivalent surface sources). To efficiently evaluate the spectral integrals in the MoM approach, and to reduce the computational effort required, a number of methods such as steepest descent and extrapolation methods have been introduced [70–72].

Despite their lack of accuracy and generality, analytical and semi-analytical methods can provide significant insight into the behavior of grating structures. For example, the Floquet-Bloch approach is specifically useful for energy band analysis. The Floquet mode plays the same role in a periodical structure as the guided modes in a waveguide and can be used to describe many interesting physical phenomena in grating structures.

Using the Floquet-Bloch approach, a modal analysis is applied to determine the space harmonics in corrugated gratings on top of dielectric waveguides. This method was previously applied for analyzing Transverse Electric (TE) and Transverse Magnetic (TM) modes in gratings on slab waveguides [73]. In this thesis, the analysis is extended to hybrid space-harmonics in gratings on rectangular dielectric waveguides. The Floquet mode analysis is then used to design the silicon waveguide grating, and to optimize the interaction impedance for the proposed TWA.

1.6 Objectives and research overview

In Chapter 2, a brief introduction of graphene with a thorough comparison between semiconductor 2DEGs and graphene 2DEGs is presented.

This thesis research develops two analytical methods for the study of travelling wave amplification in graphene. It is shown that under certain circumstances, wherein the carrier drift velocity slightly exceeds the phase velocity of the electromagnetic wave, the interaction between the electromagnetic wave and the drifting plasma wave leads to amplification of the electromagnetic wave. Although the frequency range where amplification occurs is from microwave to THz, the THz range of frequencies is the main focus in this research.

Travelling wave amplification in graphene is investigated by two methods: quantum mechanical method (Chapter 3) and classical hydrodynamic method (Chapter 4). In Chapter 3, a quantum mechanical approach is applied to obtain the conductivity of graphene for drifting charge and for slow electromagnetic waves. Kubo's formula expressions for graphene conductivity [74] are only valid for small spatial dispersion, $kv_f << \hbar\omega$, in steady state graphene, under local equilibrium condition. Neither of these assumptions is applicable for travelling wave amplification conditions in graphene. The conductivity response function of graphene for drifting charge carriers is derived using the drifting Fermi distribution function and random phase approximation. In the expressions derived in this thesis, the frequency and wave number dependent conductivity of graphene is obtained as a function of chemical potential and drift velocity.

In Chapter 4, electrons in graphene are modelled as a 2D Fermi liquid, and the classical hydrodynamic model is applied to them. Electrons in graphene behave like massless relativistic particles with an effective light speed of $v_f = c/300$. The maximum drift velocity of graphene is around $0.3v_f$. Therefore, to analyze graphene with drifting carriers we use the hydrodynamic description derived from a relativistic fluid approach [75]. Based on this hydrodynamic model, the induced current is calculated for a harmonic perturbation of both stationary and uniformly moving charged carriers, and the conductivity is obtained in the linear regime.

Methods presented in Chapters 3 and 4, show how the negative conductivity, and thus gain, is obtained for drift velocities slightly greater than the phase velocity. The results obtained from both methods are consistent in behavior; even having the same order of magnitude. Even though some parameters such as graphene viscosity and the damping factor are approximated with typical values given in the literature, the values obtained for conductivity have the same order of magnitude, confirming the validity of the results.

Chapters 3 and 4 demonstrate the possibility of travelling wave amplification in graphene.

In Chapter 5, a slow-wave grating structure is designed, and an estimation of the actual gain is obtained for the proposed graphene TWA structure. The travelling wave interaction with the space charge wave in graphene can be described as a coupled wave problem [73]. With this approach, the interaction impedance of the proposed slow-wave structure is calculated. In this chapter, a new method is developed for analyzing hybrid space harmonics in gratings on rectangular dielectric waveguides.

The final step is to experimentally verify the developed theories and computational results by fabricating and measuring a proof of concept prototype structure. Chapter 6 presents the proposed fabrication process and the measurement setup. For each step of fabrication, different tested methods are discussed and reliable fabrication recipes are developed. The measurement results confirm that graphene can be used for travelling wave amplification.

Chapter 7 summarizes the achievements of this research and provides directions for possible future work.

Chapter 2

Introduction to graphene

This chapter first briefly introduces graphene and its band structure. Then, the properties of graphene 2DEGs are compared with those of semiconductor 2DEG to explain why graphene TWAs can outperform other solid state semiconductor TWAs. The SPP waves of graphene are explored in the last section. These SPP waves can be applied to excite the slow waves in the grating structure of the proposed Graphene TWA.

Graphene is a 2D allotrope of carbon atoms with a honeycomb lattice. It is known as a building block for other carbon materials: graphite (3D), nanotubes (1D) and fullerenes (0D). It was believed that 2D crystals were unstable and could not exist, until 2004, when Novoselov and his co-workers produced a single layer graphene by means of a simple mechanical exfoliation technique [76].

2.1 Graphene lattice structure

The carbon atoms in graphene are arranged in a hexagonal structure (Fig. 2.1(a)). Assuming a basis of two atoms as a primitive unit cell, the graphene lattice can be represented as a triangular Bravaice lattice with the primitive lattice vectors of

$$\begin{aligned} \mathbf{a_1} &= \tfrac{3a'}{2}\left(1, 1/\sqrt{3}\right) \\ \mathbf{a_2} &= \tfrac{3a'}{2}\left(1, -1/\sqrt{3}\right) \end{aligned} \tag{2.1}$$

where $a' = 1.42\,A^\circ$ is the distance between two adjacent carbon atoms. Correspondingly, the reciprocal-lattice vectors are given by

$$\begin{array}{l} \mathbf{b_1} = \frac{2\pi}{3a'}\left(1, \sqrt{3}\right) \\ \mathbf{b_2} = \frac{2\pi}{3a'}\left(1, -\sqrt{3}\right) \end{array} \tag{2.2}$$

Fig. 2.1(b) shows the Brillouin zone with the three high symmetry points of Γ, M and K. The two points K and K' at the corner of the Brillouin zone are known as the Dirac points and have particular importance in the physics of graphene.

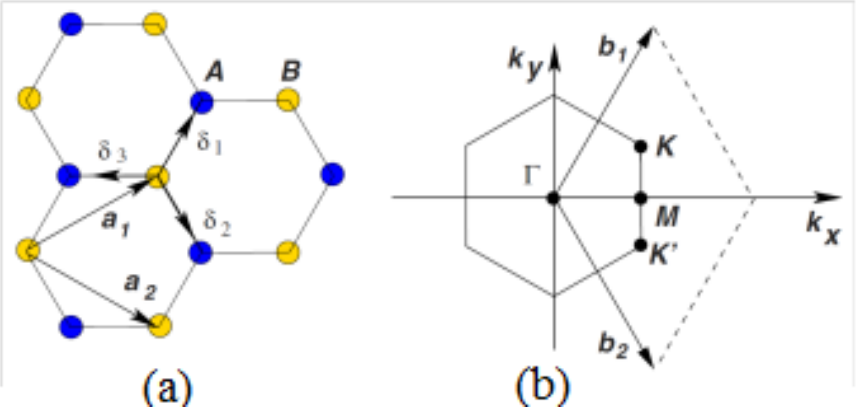

Figure 2.1: (a) Honeycomb lattice. a1 and a2 are the lattice unit vectors. (b) Brillouin zone. b1 and b2 are reciprocal-lattice vectors [3].

2.2 Graphene Hamiltonian and energy band structure

The basis of electron states contains two states belonging to the atoms from sublattices A and B (Fig. 2.1 (a)). Therefore, the Hamiltonian is described by the 2×2 matrix. The Hamiltonian of the graphene layer, derived from the tight-binding method, is [77]:

$$\begin{array}{l} H = t\begin{pmatrix} 0 & tf\left(\mathbf{k}\right) \\ tf^*\left(\mathbf{k}\right) & 0 \end{pmatrix} \\ f\left(\mathbf{k}\right) = e^{j\mathbf{k}.\delta_\mathbf{1}} + e^{j\mathbf{k}.\delta_\mathbf{2}} + e^{j\mathbf{k}.\delta_\mathbf{3}} \end{array} \tag{2.3}$$

where t is the hopping integral, and δ_i $i = 1, 2, 3$ are the nearest-neighbour vectors (Fig. 2.1 (a)). The energy obtained from this Hamiltonian is

$$\begin{aligned} E_{\pm}(\mathbf{k}) &= \pm t\sqrt{3 + g(\mathbf{k})} \\ g(\mathbf{k}) &= 2\cos\left(\sqrt{3}k_y a\right) + 4\cos\left(\tfrac{\sqrt{3}}{2}k_y a\right)\cos\left(\tfrac{3}{2}k_x a\right) \end{aligned} \tag{2.4}$$

A detailed discussion of tight binding method and the derivation of the Hamiltonian and the band-structure of graphene are presented in Appendix A. In Fig. 2.2, the full band structure of the graphene obtained from eq. 2.4 is plotted [3]. As shown in this diagram, if we limit ourselves to low energies, the band structure forms cone pairs touching at the Dirac points; therefore, the linear dispersion relation of low energy electrons is seen.

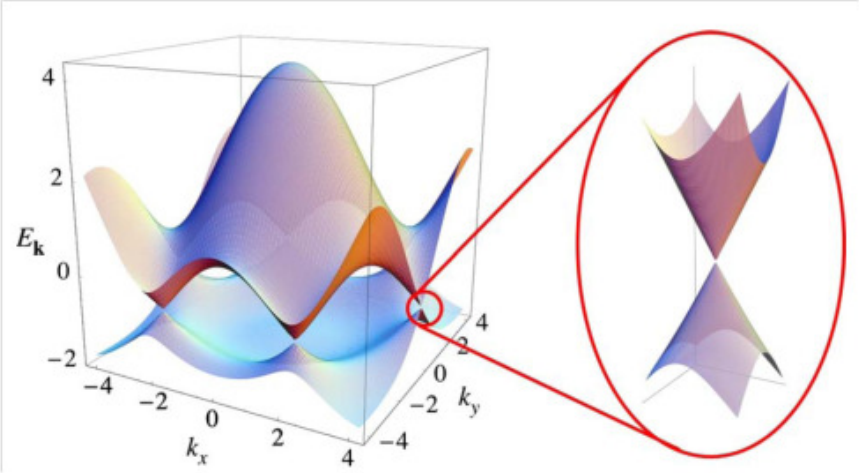

Figure 2.2: Energy band diagram of graphene. The insert is an expanded band diagram close to a Dirac point [3].

2.3 Relativistic Dirac equation

In the previous section, we saw that, near Dirac points, the electrons in graphene have a linear dispersion. This dispersion can be obtained by expanding the Hamiltonian matrix near one of the Dirac points $\mathbf{K}$ (or $\mathbf{K}'$) as $\mathbf{k} = \mathbf{K} + \mathbf{q}$ ($|\mathbf{q}| \ll |\mathbf{K}|$), where $\mathbf{q}$ is the momentum defined relative to the Dirac points [78]:

$$H = \hbar v_f \begin{pmatrix} 0 & q_x - iq_y \\ q_x + iq_y & 0 \end{pmatrix} = \hbar v_f \sigma.\mathbf{q} \tag{2.5}$$

where σ is the vector of the 2×2 Pauli matrices. This Hamiltonian is a relativistic Dirac Hamiltonian, in which v_f is the Fermi velocity:

$$v_f = 3at/(2\hbar) \tag{2.6}$$

Since there are two sublattices, A and B, in the graphene structure, and as the electronic states near neutrality points are composed of two different sublattice states, the wavefunction is described by two-component spinors. The two-component description for graphene is similar to the one for spinor wavefunctions in QED, but the spin index for graphene indicates sublattices rather than the real spin of electrons. Therefore, here, σ refers to psedospin. The comparison of the energy of electrons in graphene, $E = v_f p$, with the energy of relativistic particles, $E = \sqrt{m^2c^4 + p^2c^2}$, implies that electrons in graphene behave like massless Dirac fermions.

2.4 Comparison between Graphene 2DEG and semiconductor 2DEG

In order to use graphene as a natural 2DEG, it is conceptually useful to compare and contrast graphene with the 2DEG in conventional 2D semiconductor structures such as the Si inversion layers in MOSFETs, 2D GaAs heterostructures, and quantum wells. Transport in 2D semiconductor systems has a number of similarities and key dissimilarities with graphene.

The following features are the conceptual differences between 2D graphene and 2D semiconductors:

(i) First, 2D semiconductor systems typically have a very large (> 1 eV) band gaps. Therefore to provide 2D electrons and 2D holes, completely different electron-doped or hole-doped structures are required. By contrast, in graphene, changing the polarity of the gate voltage results in reversing the polarity of the carriers in the graphene. This property is due to the gapless band structure of graphene. Another direct consequence of graphene's gapless nature is the always-conductive nature of 2D graphene, since the chemical potential (Fermi level) is always in the conduction or the valence band. By

contrast, the 2D semiconductor becomes insulating below a threshold voltage, as the Fermi level enters the band gap.

(ii) Monolayer graphene dispersion is linear, whereas 2D semiconductors have quadratic energy dispersion, leading to substantial quantitative differences in the transport properties of the two systems.

(iii) The carrier confinement in 2D graphene is ideally two dimensional. In 2D semiconductor structures, the quantum dynamics is two dimensional by virtue of the confinement provided by an external electric field. Therefore, 2D semiconductors are quasi-2D systems and always have an average thickness of $h_z \approx 5$ to 50 nm with $h_z < \lambda_F$, where λ_F is the 2D Fermi wavelength.

(iv) Graphene systems are chiral, whereas 2D semiconductors are non-chiral. The unit cell of the graphene contains two atoms from two different sublattices. Because of these two sublattices, graphene quasiparticles are described by two-component wavefunctions, similar to the description of spinor wavefunctions. However, in graphene, the spin index indicates sublattices rather than the real spin of electrons. Therefore, it called pseudospin. This pseudospin is linked to the propagation direction, a property that leads to introduction of chirality in graphene [79]. The chirality of graphene leads to some dissimilarities between the transport behaviors of electrons in graphene and those in 2D semiconductor structures.

(v) Since the plasma properties of 2DEG become more pronounced with a decreasing effective mass of electrons and increasing electron mobility, THz devices based on graphene heterostructures with massless 2DEG can significantly surpass those made of relatively standard semiconductor heterostructures in longer mean free and lower collision frequency.

(vi) The bonding of electrons to a graphene plane is stronger than the bonding of semiconductor electrons to a quantum well. Therefore, electrons in graphene remain two-dimensional up to room temperature, and beyond to the melting point of graphene. Chemical doping or electrostatic gating can induce and tune net carrier densities over a very large range (more than $\pm 10^{13} cm^2$, equivalent to Fermi energy shifts of ± 350 meV). Thus, graphene behaves like a two-dimensional metal even at room temperature. The maximum achievable semiconductor based 2DEG is in the order of $\pm 10^{11} cm^{-2}$. [80]

2.5 Graphene surface plasmon polariton waveguide

The slow wave of the proposed graphene travelling wave amplifier is a confined surface wave at the grating surface beneath the graphene; therefore, surface plasmon polariton

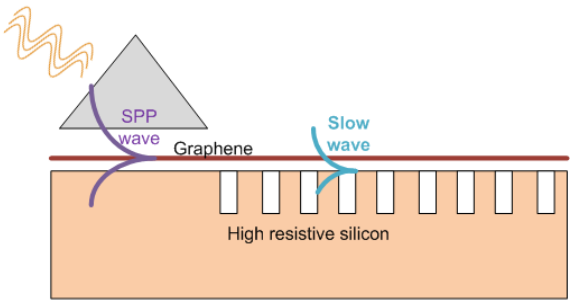

Figure 2.3: Proposed structure

wave of graphene can be used to excite this surface slow wave (Fig. 2.5). This section studies surface plasma waves guided by simple graphene structures and discusses its basic properties.

Graphene can support surface plasmons (SP) similar to those on metal/dielectric interfaces. The structures made from noble metals like Au and Ag are the most typical structures carrying SPPs at optical frequencies. However, these SPP waveguides suffer from large Ohmic losses and nontunability. Moreover, they cannot confine THz SPP waves as efficiently as they confine optical SPP waves.

Doped semiconductors are conventionally regarded as THz SPP waveguides. In order to qualify as low-loss plasmonic materials, such semiconductors must have bandgaps and plasma frequencies larger than the frequency range of interest. A large plasma frequency ensures a negative real permittivity, and a large bandgap ensures almost no interband transition losses. Graphene is a promising plasmonic material for THz applications. In zero band-gap graphene the interband transitions occur above Fermi energy level, which can be tuned by the amount of doping or back gate voltage and shifted to frequencies beyond the region of interest. Below the interband threshold, losses are primarily due to impurity scattering, excitation of optical phonons, and intraband transitions of electrons. Analysis of these loss mechanisms shows that graphene can have lower losses than conventional metal/dielectric interfaces up to frequencies corresponding to 0.2 eV ($\sim$ 50 THz) [81]. The density of electrons or holes and consequently the Fermi level can be tuned easily by the application of a back gate voltage. Graphene essentially behaves like a metallic structure due to its gap-less electronic band-structure. Therefore, conductivity is the most appropriate parameter for characterizing its electromagnetic properties. Moreover, due to its mono-atomic thickness, graphene is essentially a 2D material. It must consequently be modelled by surface conductivity, which relates the surface current to the tangential electric field in the graphene plane.

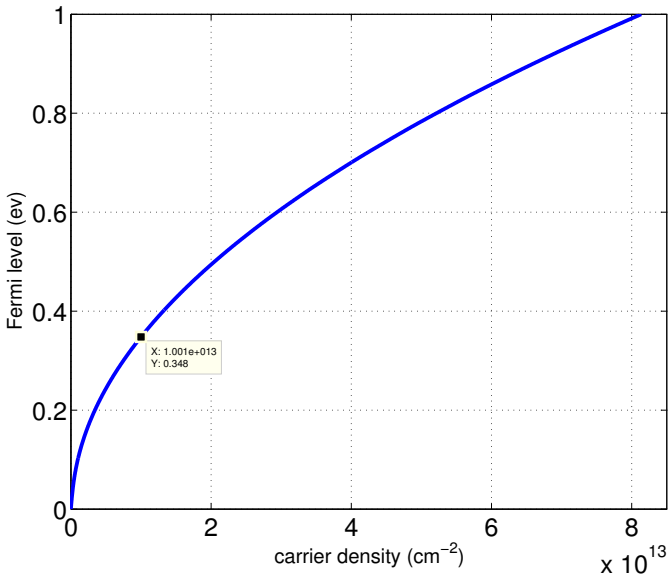

Figure 2.4: Fermi level versus surface carrier density

Different methods, mainly random phase approximation and Kubo method, for calculating the dielectric constant and conductivity of graphene have been discussed in several recent works. [82–86]. Here we use the results obtained from the Kubo formula [84]. For high frequencies, $\omega \gg kv_f, \tau^{-1}$, the dynamical conductivity, $\sigma = \sigma' + j\sigma''$, can be written as:

$$\begin{aligned}\sigma(\omega) = \frac{ie^2 k_B T}{\pi\hbar^2}\frac{1}{\omega - i\Gamma}\left(\frac{\mu_c}{k_B T} + 2\ln\left(e^{-\mu_c/k_B T}+1\right)\right) + \\ \frac{e^2}{4\hbar}\left(G(\omega) - i\frac{2\omega}{\pi}\int_0^\infty \frac{G(\omega') - G(\omega)}{\omega^2 - \omega'^2}d\omega\prime\right) \\ G(\omega) = \frac{sinh(\hbar\omega/2k_B T)}{cosh(\mu_c/k_B T) + cosh(\hbar\omega/2k_B T)}\end{aligned} \tag{2.7}$$

where μ_c is the chemical potential, $\Gamma = 1/\tau$ is a phenomenological scattering rate, T is temperature, k_B is the Boltzmann constant, and e is the charge of an electron. There is no external magnetic field, and so the local conductivity is isotropic.

For an isolated graphene sheet, the chemical potential, μ_c, is determined by the carrier

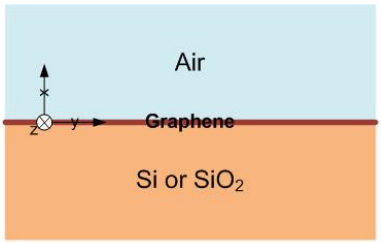

Figure 2.5: The graphene SPP waveguide

density n_s:

$$n_s = \frac{2}{\pi\hbar^2 v_f^2}\int_0^\infty \varepsilon\left(f(\varepsilon-\mu_c)-f(\varepsilon+\mu_c)\right)d\varepsilon, \tag{2.8}$$

in which $f(\varepsilon) = \left(e^{\varepsilon/k_BT}+1\right)^{-1}$ is the Fermi-Dirac distribution and $v_f \cong 10^6$ m/s is the Fermi velocity. The carrier density can be controlled via chemical doping or electrical gating. The plot of chemical potential versus carrier density obtained from eq. 2.8 is shown in Fig. 2.4.

The first term in Eq.2.7 corresponds to the intraband electron-photon scattering processes, and is similar to the Boltzmann-Drude expression. The second term in Eq.2.7 corresponds to the direct interband electron transitions. The interband transition occurs above the frequency threshold $\hbar\omega \approx 2\mu_c$.

The structure under consideration is shown in Fig. 2.5. The propagation direction is along z, and the structures are assumed to be infinite and invariant along the y axis.

Since the structure is two dimensional, we have TE and TM modes. The field distribution for the TM mode is:

$$\begin{cases}(E_{x1}, E_{z1}, H_{y1})e^{-\alpha_0 x}e^{-j\beta_z z} & x>0\\ (E_{x2}, E_{z2}, H_{y2})e^{\alpha_{Si} x}e^{-j\beta_z z} & x<0\end{cases} \tag{2.9}$$

where $\alpha_0 = \sqrt{\beta_z^2 - k_0^2}$ and $\alpha_{Si} = \sqrt{\beta_z^2 - \epsilon_{Si}k_0^2}$. The TE mode has a similar field distribution for its H_z, H_x and E_y field components. The dispersion equation for the propagation constant of each mode is obtained from the solution of Maxwell's equations in each medium and the following boundary conditions at the graphene interface.

$$\hat{n}\times(\mathbf{H_1}-\mathbf{H_2}) = \sigma\mathbf{E}_t \tag{2.10}$$

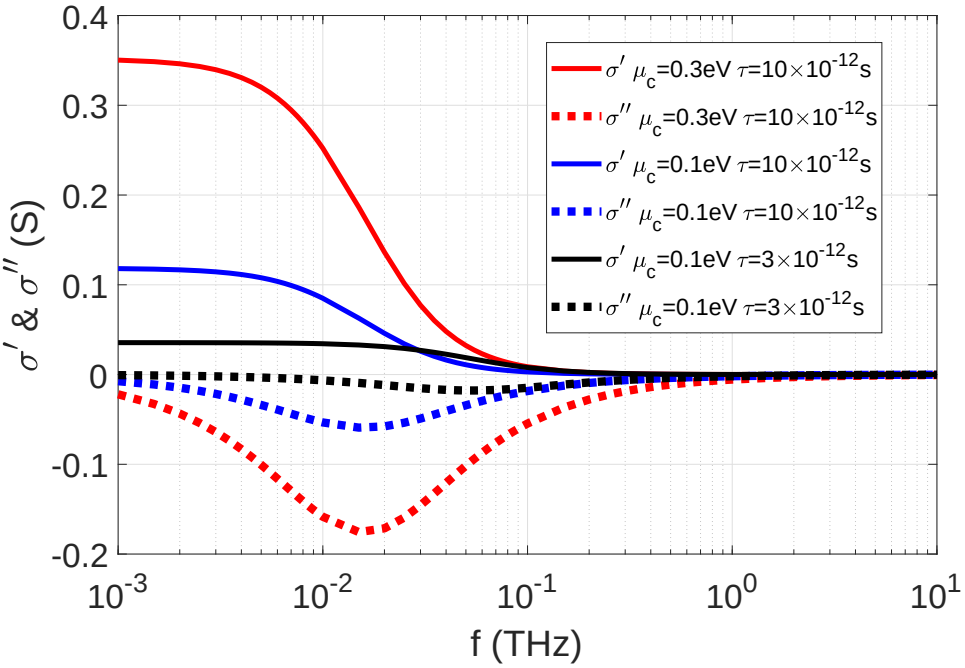

Figure 2.6: The real and imaginary parts of conductivity versus frequency for different values of chemical potential and relaxation time.

The dispersion equation obtained for TE surface waves is:

$$\frac{\alpha_0}{\omega\mu_0} + \frac{\alpha_{Si}}{\omega\mu_0} = -j\sigma \tag{2.11}$$

and for TM waves is:

$$\frac{\omega\epsilon_0}{\alpha_0} + \frac{\omega\epsilon_{Si}}{\alpha_{Si}} = j\sigma \tag{2.12}$$

From the above two dispersion equations it is clear that the imaginary part of dynamic conductivity $\sigma = \sigma' + j\sigma''$, determines which type of surface wave, TE or TM, can propagate. When σ'' is positive, graphene guides the TE SPP wave, and when the σ'' is negative, graphene behaves like a thin metal film capable of supporting TM SPP surface waves.

The sign of σ'' depends on which of the internand and intraband terms in the conductivity relation is dominant. The imaginary part of conductivity, corresponding to intraband

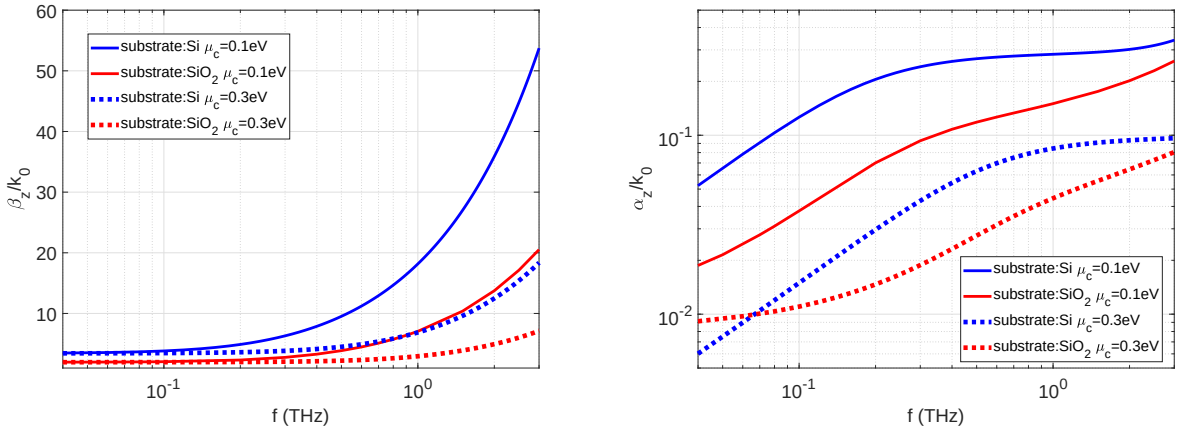

(a) propagation constant (b) attenuation constant

Figure 2.7: Normalized (a) propagation constant and (b) attenuation constant of TM wave carried by graphene layer on top of Si and SiO_2 substrate. The solid and dotted lines are plotted for graphene chemical potention 0.1 eV and 0.3 respectively. The $\tau = 10 \times 10^{-12}s$ for all curves.

transitions, is negative, but is positive for the conductivity, corresponding to interband transitions. In graphene with non-zero Fermi energy, the Boltzmann-Drude intraband term is dominant in the THz frequency range when $\hbar\omega/2 < |\mu|$. On the other hand, the interband term is dominant at higher frequencies when $|\mu| < \hbar\omega/2$. Therefore, for Fermi energies greater than 0.2 meV, graphene can support TM SPP waves at the THz frequency range. Figure 2.6 shows the real and imaginary parts of the conductivity for different values of Fermi level versus frequency.

2.5.1 Two-layer structure

The simplest graphene based SPP waveguide is a graphene layer on top of a Si or SiO_2 substrates. The relative dielectric constants of Si and SiO_2 at THz range of frequency are $\epsilon_{si} = 11.7 - j0.0014$ and $\epsilon_{sio_2} = 3.84 - j0.0314$, obtained from experimental values [87]. The propagation and attenuation constants of TM plasmonic waves obtained by solving equation 2.12 are depicted in Figure 2.7 for two values of chemical potential. The large propagation constant of $50k_0$ is obtained for an SPP wave of graphene on a silicon substrate for $\mu_c = 0$ eV and $\tau = 10 \times 10^{-12}$ s at 1 THz. The propagation constants of slow waves of

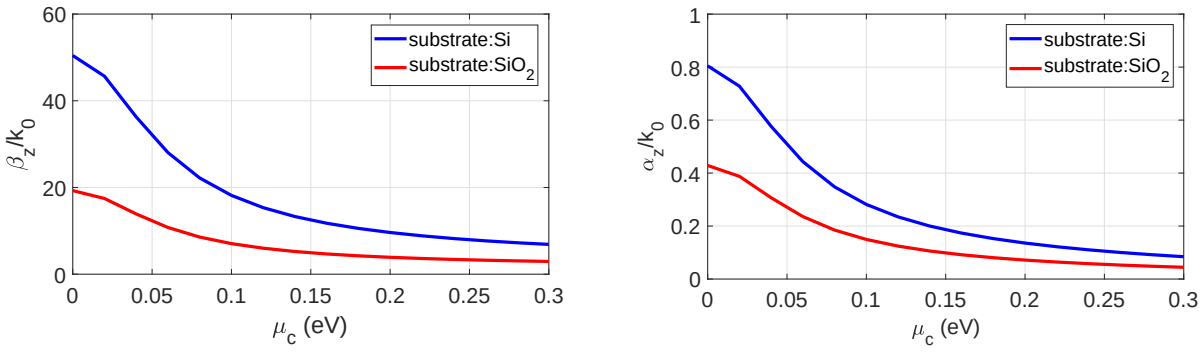

(a) propagation constant

(b) attenuation constant

Figure 2.8: Normalized (a) propagation constant and (b) attenuation constant of TM wave versus chemical potentioal of the graphene layer for $\tau = 10\mu s$ at f=1 THz. The blue and red curves are for TM wave carried by graphene layer on top of Si and SiO_2 substrate respectively.

the grating structures are big. Therefore, SPP waves can be used to excite these waves.

The attenuation constant of the SPP wave is determined by two factors: the graphene loss and the substrate loss. When the SPP wave is more confined to the graphene layer, the graphene loss plays the dominant role, and when it is less confined to the graphene layer and more spread out, the loss of the substrate plays the dominant rule. The normalized propagation constant and thus the confinement of the electromagnetic field to the graphene layer is higher at larger frequencies. The refractive index of Si is higher than that of SiO_2. Therefore, on the Si substrate, the field is more confined to the graphene layer and the attenuation constant is higher. However, for $\mu_c = 0.3ev$, at frequencies lower than $f \approx 0.07THz$ the attenuation constant for the SiO_2 substrate is higher. At these frequencies, the field is less confined to the graphene layer and penetrates more into the substrate. Therefore, the loss of the substrate playes the dominant role, and since SiO_2 has higher intrinsic loss than Si, the attenuation constant for the SiO_2 substrate is higher.

Figure 2.8 shows that the normalized propagation constant and attenuation constant decrease by increasing the chemical potential. Increasing the chemical potential of the graphene increases σ' and $|\sigma''|$ (see Fig. 2.6). Moreover, it can be seen in eq. 2.12, that increasing $|\sigma''|$ decreases the real part of $\alpha_{0,si}$, resulting in an increase of the real part of the propagation constant ($\alpha_{Si,0} = \sqrt{\beta_z^2 - \epsilon_{Si,0}k_0^2}$). Thus, for larger chemical potential, the field propagates with the lower phase velocity and is more confined to the graphene layer. Since graphene is a lossy medium, more confinement to the graphene layer, results in a

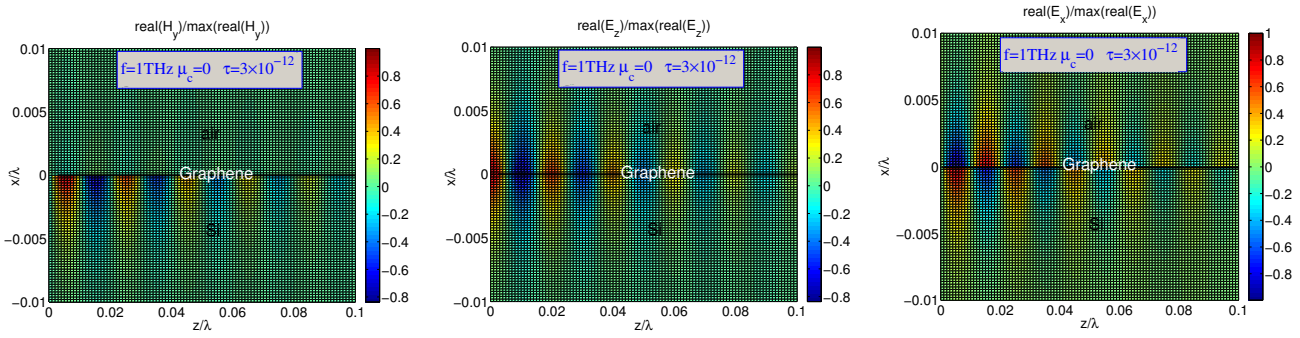

(a) Re(H_y)

(b) Re(E_z)

(c) Re(E_x)

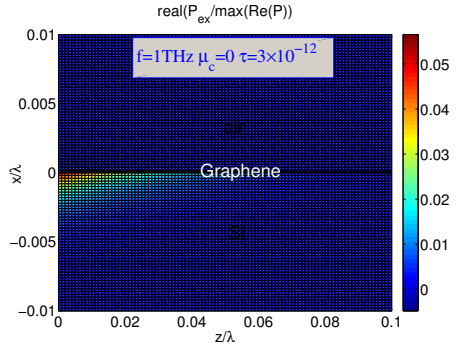

(d) Re(P_x)

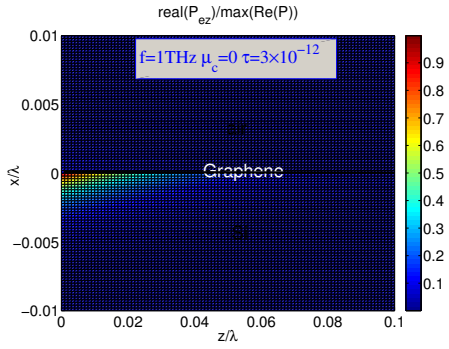

(e) Re(P_z)

Figure 2.9: The profile of normalized real part of (a)Re(H_y) (b)Re(E_z) (c)Re(E_x) (d)Re(P_{ex}) (e)Re(P_{ez}) in the xz plane at f=1THz for μ_c=0ev and τ=3×10^{-12}.

larger attenuation constant. The carrier density and thus the chemical potential can be controlled easily by a gate voltage.

The normalized real part of non-zero components of the TM surface field in an xz plane, where z aligns with the propagation direction, is depicted in Fig. 2.9. It is assumed that the graphene strip is wide enough to neglect the variation of the field along the y axis far from the edges. These figures show the surface nature of SPP-waves and the capability of graphene to effectively suppress the magnetic field and prevent it penetrating to the top layer with a lower refractive index. These results show that, despite being just one atom layer thick, graphene acts like a good conductor, shielding the magnetic field. The transverse component of the electric field has a symmetric profile, and the perpendicular component has an antisymmetric profile. As a general rule, there is a trade off between a larger propagation distance and stronger confinement. We show the tunability of prop-

agation and attenuation constants via electrical gating. This feature can be exploited in realization of phase delays or modulators based on a monolayer of graphene.

Chapter 3

Quantum mechanical analysis of travelling wave amplification in graphene

In this chapter, a quantum mechanical method is developed to analyze the travelling wave amplification in graphene. First a qualitative description of the gain mechanism and gain conditions is presented. Then quantitative analysis is presented by calculating the conductivity of graphene.

In the previous chapter, the graphene conductivity obtained from Kubo formula [74] was presented (eq. 2.7) This expresion is given for a small spatial dispersion, $kv_f << \hbar\omega$, under local equilibrium condition. Neither of these assumptions is applicable for travelling wave amplification conditions in graphene. In TWAs, the charged carriers are biased to have a drift velocity, and the electromagnetic waves are slowed down to have a phase velocity smaller than the drift velocity of carriers. For graphene with drifting carriers, the equilibrium condition is not applicable. Also for very slow electromagnetic waves, the wavenumber, $k = 2\pi/V_{ph}$, cannot be assumed to be negligible any more. Therefore, in this chapter, the conductivity of graphene for drifting charge carriers is obtained by applying the drifting Fermi distribution function to the conductivity response function of graphene. The frequency and wavenumber dependent conductivity of graphene is obtained for drifting charge carriers as a function of chemical potential and drift velocity.

The travelling wave interaction can be described as a stimulated intraband radiative transition of electrons. In contrast to the mechanism of radiation in lasers, wherein the electrons transit from the conduction to the valence band to emit photons. In travelling wave

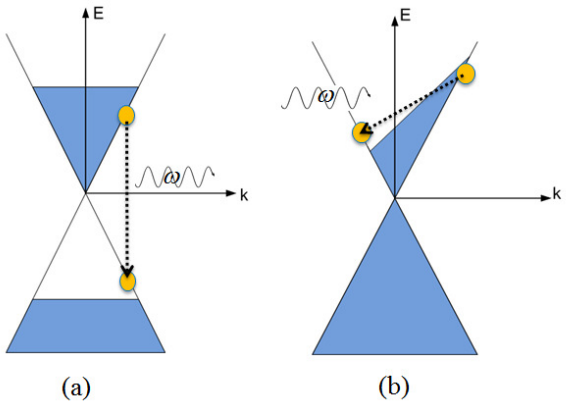

Figure 3.1: (a) Direct interband radiative transition, (b) indirect intraband transition

amplifiers, the radiative intraband transitions play the dominant role in electromagnetic amplification. Amplification can be achieved when there is a large electron population at the higher energy states. In travelling wave amplifiers, this population inversion is achieved by applying a drift DC current and increasing the average momentum of the electrons.

During transitions, three waves interact: the electron wave function in the both initial and final states, and the electromagnetic wave. The energy and momentum should be conserved during the transition. Considering an electromagnetic wave with a frequency of ω and wavevector of $\mathbf{q}$, in a radiative transition, we should have

$$E_i - E_f = \hbar\omega \tag{3.1}$$

$$\mathbf{k}_i - \mathbf{k}_f = \mathbf{q} \tag{3.2}$$

where E_i and E_f are the energy of the electron states at the initial and final states respectively; ω and $\mathbf{q}$ are the frequency and wave number of the electromagnetic wave, and $\mathbf{k}_i$ and $\mathbf{k}_f$ are the electron wave numbers of the initial and final states, respectively.

Figure 3.1 shows that if the transition occurs in a vacuum or in a homogeneous medium, the two conditions of 3.1 and 3.2 can be satisfied simultaneously only for interband transitions. However, for intraband transition, the wavenumber of the electromagnetic wave should be increased to a value greater than ω/V_f. This increase can be achieved in a periodic structure where one of the space harmonics has a large enough propagation constant to balance the momentum equation 3.2.

Figure 3.2 illustrates schematically how the population inversion is induced in travelling wave amplifiers. In this figure, the picture on the right is the top view of the left one. In a

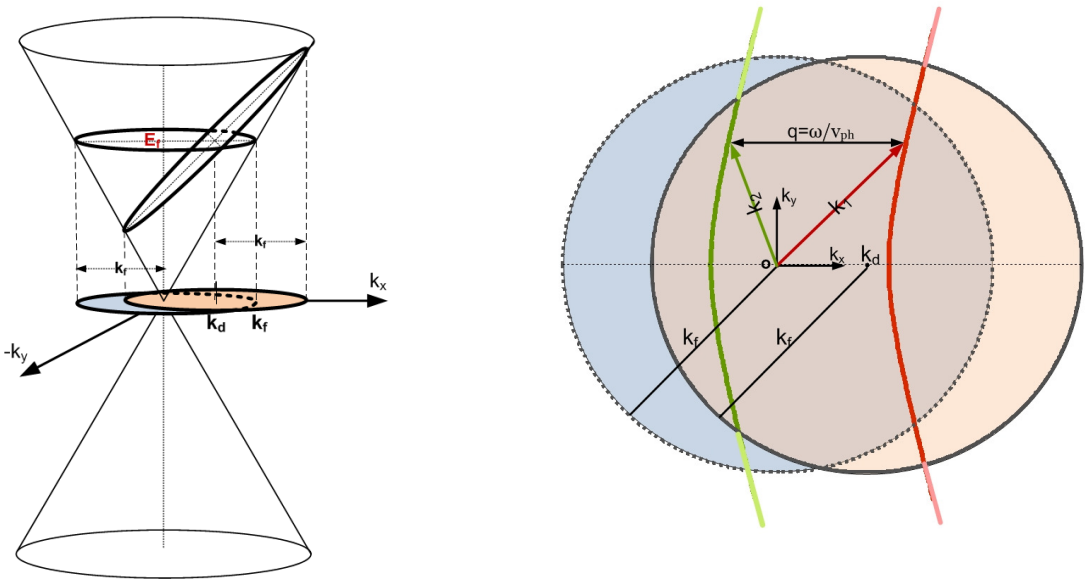

Figure 3.2: Schematic demonstration of population inversion in graphene by increasing the average momentum of electrons. The blue and orange circles are the Fermi circles of filled states in k-space of an unbiased and biased graphene, respectivly at T=0. The green and red curves denote, respectively, the lower and upper energy states in k-space that satisfy both energy and momentum conservation equations (eq. 3.1 and 3.2).

travelling wave amplifier, instead of injecting carriers electrically or optically, the electrons are accelerated to a high drift velocity, equivalent to increasing the average momentum of electrons in the solid. Therefore, the whole electron density distribution will be shifted in the k-space by the value of k_d, which is a function of the drift velocity of electrons, V_d.

Figure 3.2(b) shows schematically how increasing the value of k_d will eventually lead to population inversion. In this figure, it is assumed that the temperature, T, is zero. The states inside the circle with the radius of $k_f = E_f/\hbar V_f$ are full, and the states outside of this circle are empty. The density of electrons is not changed in a moving frame. Therefore, the radius of the Fermi circle remains constant. The red and green curves denote the states in k-space that satisfy both equations 3.1 and 3.2. As shown in Fig. 3.2, by increasing the value of k_d, more higher-energy states (red curve) are filled and, simultaneously, lower energy states (green curve) are emptied until, for a sufficiently large value of V_d, the length of the red curve covered by the Fermi circle becomes greater than that for the green one. In this case, the population inversion has occurred, and a net gain is achieved.

The above discussion has only described qualitatively the gain mechanism in travelling wave amplifiers. We next apply linear response theory to drive the conductivity of graphene.

The Hamiltonian equation of a system with a small perturbation can be written as in [88]

$$\hat{H}(t) = \hat{H}_0 + F(t)\hat{B} \tag{3.3}$$

where H_0 is a time-independent diagonal matrix, and $F(t)$ is the external time-dependent field that couples linearly to an observable $\hat{B}$. $F(t)$ is assumed to be a small time dependent perturbation expressed as $e^{i(\omega - i\delta)t}$. Then, the perturbation of an observable $\hat{A}$ ($A(t) = A_0 + A_1 e^{i(\omega - i\delta)t}$) is

$$\langle \hat{A}_1 \rangle(\omega) = \chi_{AB}(\omega) F(\omega) \tag{3.4}$$

where $\chi_{AB}(\omega)$ is the linear response function of the system and defined as [88]

$$\chi_{AB}(\omega) = \sum_{mn} \frac{f_m - f_n}{\hbar\omega + E_n - E_m - i\hbar\delta} B_{mn} A_{nm} \tag{3.5}$$

A complete discussion and derivation of the linear response function is given in [88]. The Hamiltonian of Dirac electrons in the presence of an electromagnetic field is

$$\hat{H} = \hat{H}_0 + \hat{\mathbf{J}} \cdot \mathbf{A}(\mathbf{r}, t) \tag{3.6}$$

where $\mathbf{A}(\mathbf{r}, t) = \mathbf{A_0} e^{i(\omega t - \beta z)}$ is the vector potential, and $\hat{\mathbf{J}}$ is the current operator. By comparing this Hamiltonian (eq. 3.6) with the general form of the Hamiltonian of a system under perturbation (eq. 3.3), the current induced by the external vector potential is obtained as

$$\mathbf{J}(\omega, \mathbf{q}) = \bar{\chi}_{\mathbf{JJ}}(\omega, \mathbf{q}) \mathbf{A}(\omega, \mathbf{q}), \tag{3.7}$$

where $\chi_{\mathbf{JJ}}$, a 2×2 matrix, is the current-current response function of the graphene. The current operator of graphene is [89]

$$\mathbf{J} = e v_f \bar{\sigma} \tag{3.8}$$

in which $\bar{\sigma}$ is the Pauli matrices vector. Therefore, the current-current response function element can be written as

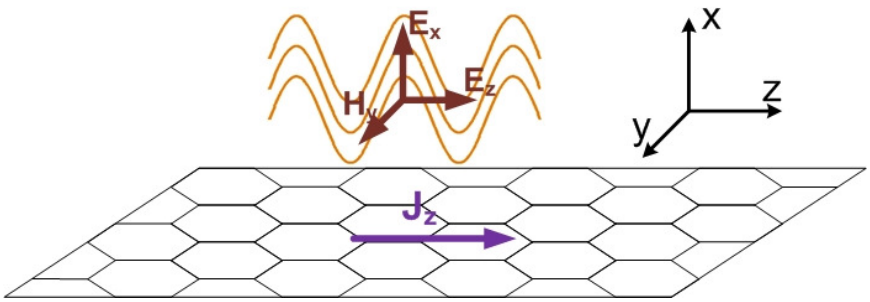

Figure 3.3: Graphene sheet; lying in the y-z plane, illuminated with a TM_z electromagnetic field

$$\chi_{J_\alpha J_\beta}(\mathbf{q},\omega) = g_s g_v e^2 v_f^2 \sum_{ss'} \sum_{\mathbf{k}} \lambda_{ss'}^{\alpha\beta}(\mathbf{k},\mathbf{q}) \frac{f(E_{\mathbf{k},s}) - f(E_{\mathbf{k}+\mathbf{q},s'})}{E_{\mathbf{k}+\mathbf{q},s'} - E_{\mathbf{k},s} + \hbar(\omega - i\delta)} \tag{3.9}$$

where

$$\lambda_{ss'}^{\alpha\beta}(\mathbf{k},\mathbf{q}) = \langle \mathbf{k}, s|\hat{\sigma_\alpha}|\mathbf{k}+\mathbf{q}, s'\rangle\langle \mathbf{k}+\mathbf{q}, s'|\hat{\sigma_\beta}|\mathbf{k}, s\rangle \tag{3.10}$$

is the overlap of states which includes particular chirality properties of graphene. In eq. 3.9, $g_s = g_v = 2$ denotes the spin and valley degeneracy, and $f(E_{\mathbf{k},s})$ is the Fermi distribution function. The energy dispersion relation of graphene is $E_{\mathbf{k},s} = s\hbar v_f|\mathbf{k}|$. $\chi_{J_\alpha J_\beta}$ is the response function of the current in the α direction induced by a vector potential in the β direction. For a graphene layer in the yz plane $\alpha, \beta = z, y$ and the $\hat{\sigma_z}$ and $\hat{\sigma_y}$ equal $\hat{\sigma_1}$ and $\hat{\sigma_2}$ respectively, where $\hat{\sigma_1} = \left(\begin{smallmatrix} 0 & 1 \\ 1 & 0 \end{smallmatrix}\right)$ and $\hat{\sigma_2} = \left(\begin{smallmatrix} 0 & -j \\ j & 0 \end{smallmatrix}\right)$ are the Pauli matrices.

In equations 3.9 and 3.10, the terms for $s = s' = \pm 1$ represent the electron-electron ($s = 1$) and hole-hole ($s = -1$) intraband transitions, and the $s \neq s'$ represent the interband transitions. In equation 3.10, $|\mathbf{k}_s\rangle$ are the electron and hole wave vectors that diagonalize the independent electron Hamiltonian, H_0, of graphene.

$$|\mathbf{k}, s\rangle = \frac{1}{\sqrt{2}} \begin{pmatrix} e^{-i\theta_{\mathbf{k}}} \\ \pm e^{-i\theta_{\mathbf{k}}} \end{pmatrix} e^{i\mathbf{k}\cdot\mathbf{r}}. \tag{3.11}$$

We assume that a TM_z electromagnetic field illuminates the graphene sheet lying in the y-z plane (see Fig. 3.3). Therefore, the vector potential and the electric field in the plane of graphene are in the z-direction. We are interested exclusively in the longitudinal z-component of the induced current, which is the only component that can be coupled to the incident electromagnetic field. By substituting eq. 3.11 in eq. 3.10 for $\lambda_{ss'}^{zz}$, we obtain

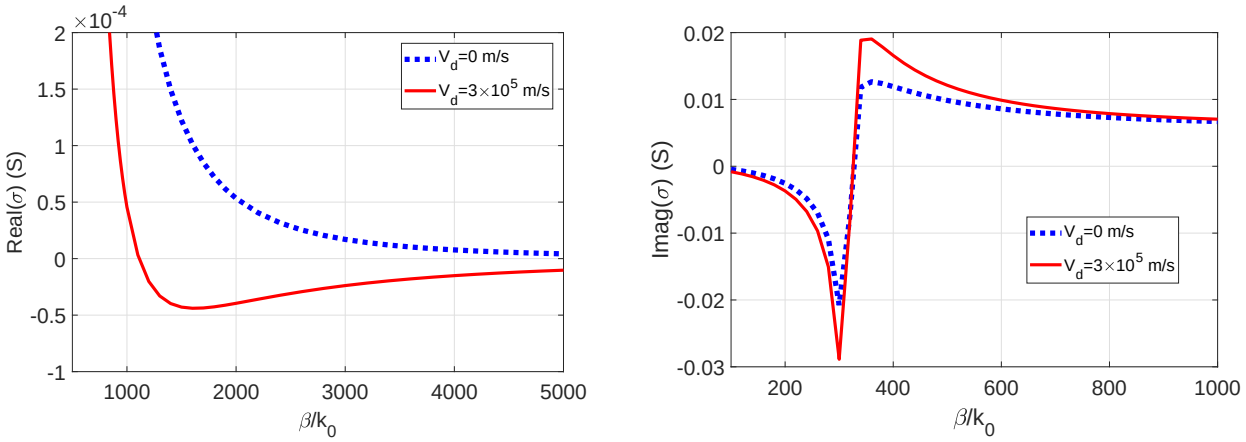

Figure 3.4: Real and imaginary parts of the conductivity versus β at $f = 1$ THz for $\mu_c = 0.3$ eV and two values $V_d = 0$ m/s(dotted line) and $V_d = 3 \times 10^5$ m/s (solid line).

$$\lambda_{ss'}^{zz}(\mathbf{k},\mathbf{q}) = \frac{1 + ss'\cos(\theta_{\mathbf{k}} + \theta_{\mathbf{k}+\mathbf{q}})}{2}$$
$$= \frac{1}{2} + \frac{ss'}{2}\left(\frac{k\cos(2\theta_{\mathbf{k}}) + q\cos(2\theta_{\mathbf{k}})\cos(\theta_{\mathbf{k}})}{\sqrt{k^2+q^2+2kq\cos(\theta_{\mathbf{k}})}} + \frac{q\sin(\theta_{\mathbf{k}})sin(2\theta_{\mathbf{k}})}{\sqrt{k^2+q^2+2kq\cos(\theta_{\mathbf{k}})}}\right) \tag{3.12}$$

where $k = |\mathbf{k}|$, and $\theta_{\mathbf{k}}$ is the angle of $\mathbf{k}$ from z axis. To obtain the second expression, the wavevector $\mathbf{q}$ is assumed to be in the z direction, $\theta_{\mathbf{q}} = 0$.

To analyze the response of drifting carriers, the Fermi distribution function of electrons with the average drift velocity of V_d is substituted in eq. 3.9, which is [90]

$$f(E_{\mathbf{k},s}) = \frac{1}{1 + e^{\left((E_{\mathbf{k},s} - \mathbf{P}\cdot\mathbf{V_d} - \mu_c)/k_BT\right)}} \tag{3.13}$$

To calculate eq. 3.9 numerically, the summation over $\mathbf{k}$, $\sum_{\mathbf{k}}$, is replaced by 2D integration $\int\int \frac{|\mathbf{k}|}{(2\pi)^2} d\theta_{\mathbf{k}} dk$ using 2D density of states in the k-space. The second expression in eq.3.12, which gives $\lambda_{ss'}^{zz}$ explicitly as a function of $\theta_{\mathbf{k}}$ and $|\mathbf{k}|$, is used to numerically calculate the 2D integral in the cylindrical coordinate system.

The conductivity of graphene is $\sigma_{zz} = i\chi_{J_zJ_z}/\omega$ ($J_z = \sigma_{zz}E_z$ and $\mathbf{E} = -i\omega\mathbf{A}$). The real part of the conductivity shows whether we have gain or loss. The real part of conductivity is positive for lossy materials and negative for materials with gain.

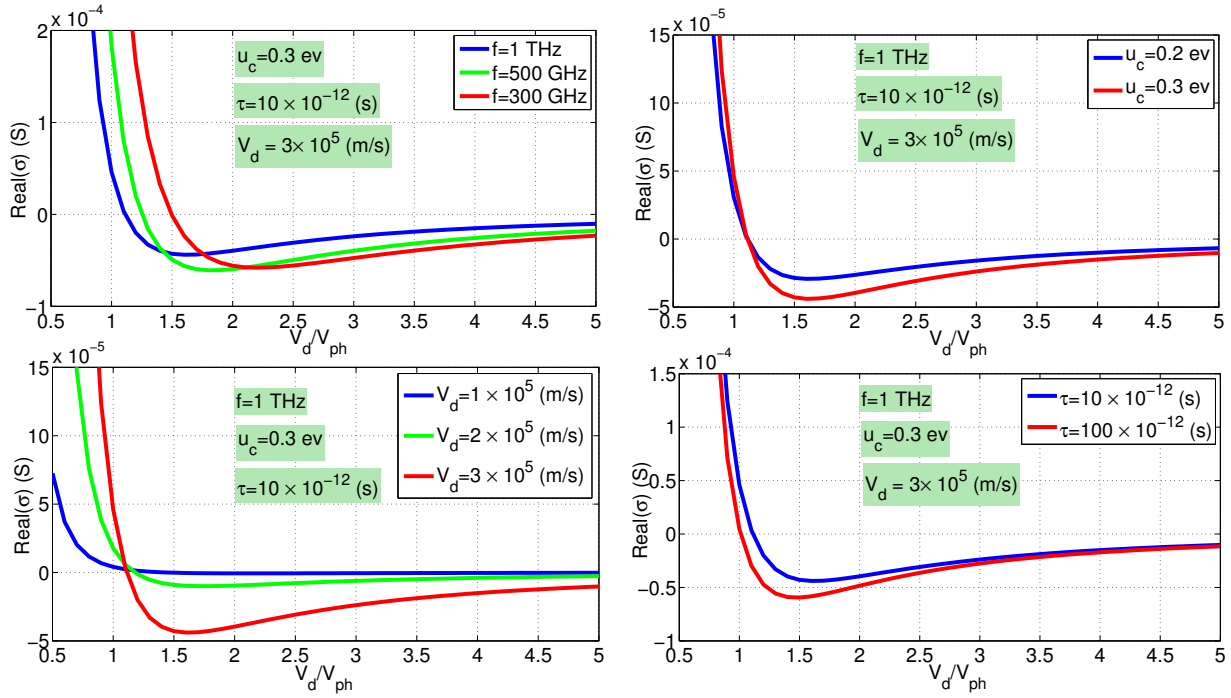

Figure 3.5: Real part of conductivity versus V_d/V_{ph} for different values of the frequency given $V_d = 3 \times 10^5$ m/s, $\tau = 10^{-11}$ and $u_c = 0.3$ eV (top left); the chemical potential given $V_d = 3 \times 10^5$ m/s and $\tau = 10^{-11}$ s at the frequency of 1THz (top right); the drift velocity given $u_c = 0.3$ eV and $\tau = 10^{-11}$ s at the frequency of 1THz (bottom left); and the collision relaxation time given $V_d = 3 \times 10^5$ m/s and $u_c = 0.3$ eV (bottom right).

In Fig. 3.4, the real and imaginary parts of the conductivity versus $\beta = q$ are plotted at $f = 1$ THz for $\mu_c = 0.3$ eV, $\tau = 10 \times 10^{-12}$ s, and two values: $V_d = 0$ (dotted line) and $V_d = 3 \times 10^5$ m/s (solid line). The real part of the conductivity is negative for $V_d = 3 \times 10^5$ m/s and for $\beta > 1112k_0$ which corresponds to $V_{ph} < 0.9V_d$ ($\beta = \omega/V_{ph}$). Here, the calculated conductivity also confirms that in order to have gain, a drift velocity should be applied and the electromagnetic wave should be slowed down to phase velocities smaller than the drift velocity of electrons.

In the previous chapter it was shown that the imaginary part of the graphene conductivity for $\beta \approx 0$ and $V_d = 0$, is negative (Fig. 2.6). Consistent with this result, in Fig. 3.4(b), the imaginary part of the conductivity is also negative for small values of $\beta < 320k_0$ and both $V_d = 0$ and $V_d = 3 \times 10^5$ m/s.

In the proposed TWA, graphene acts as a current source. Therefore, the real part of

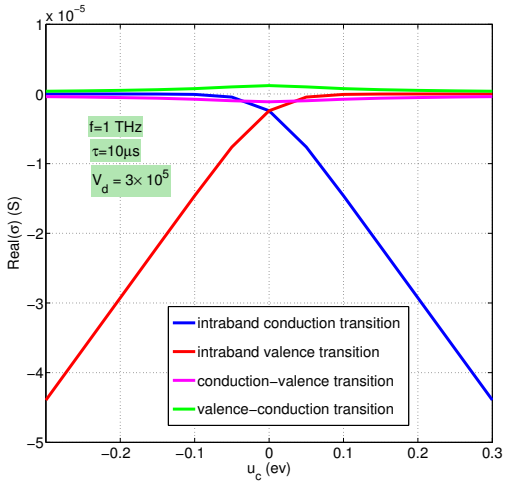

Figure 3.6: The real part of four different interband and intraband conductivity terms versus chemical potential

the conductivity is more important for the analysis (see Chapter 5). The effect of the imaginary part of the conductivity is to change the real part of the dielectric constant. Since graphene is a zero thickness conductor, this effect is insignificant.

in Fig. 3.5 a-d, the real part of the conductivity is plotted versus V_d/V_{ph} for different values of frequency, chemical potential, drift velocity, and collision relaxation time ($\tau = 1/\delta$). The maximum negative conductivity is increased by increasing the chemical potential or equivalently electron density, and the drift velocity. Figure 3.5(a) shows that the electromagnetic wave should be slowed down more for higher frequencies to achieve the maximum gain.

In Figure 3.6 the four different interband and intraband conductivity terms versus chemical potential are plotted separately to show the contribution of each individually (eq. 3.9). This figure shows that, for a positive chemical potential, the radiative electron-electron intaraband transitions in the conduction band cause amplification (s=s'=+1), and for a negative chemical potential, the hole-hole transitions in the valence band are the source of amplification. Except for chemical potential values close to zero, the effect of interband transitions are negligible with respect to the intraband terms. As expected, the transitions from valence band to conduction band, during which a photon is absorbed, gives positive conductivity, and the transition from conduction to valence band involving photon emission gives negative conductivity.

3.1 Conclusion

In this chapter, the travelling wave amplification in graphene is explored both qualitatively and quantitatively. The quantum mechanical approach is applied to obtain the frequency and wave number dependent conductivity of graphene with drifting charge carriers under a non-equilibrium condition. The conductivity relations show that for a slow electromagnetic field with the phase velocity smaller than the drift velocity of carriers, graphene changes from a lossy propagating medium to a gain medium that converts power from the DC source to the electromagnetic field. This result shows that graphene can be used in solid state travelling wave amplifiers.

The quantum mechanical approach gives significant insight into the physical mechanism of traveling wave interactions inside graphene. It is a very precise model for an ideal system with no defects and disorder and for small source perturbation. However, it is extremely hard to model all macroscopic phenomena, quantum mechanically. Therefore, in the next chapter, a more classical approach based on the hydrodynamic model of graphene is presented.

Chapter 4

Hydrodynamic model of graphene

It is reasonable to use a hydrodynamic approach to describe the dense electron-hole plasma in semiconductor systems in which the electron-electron, electron-hole, and hole-hole collisions predominate over collisions between electrons and holes with disorder. These collisions can occur in intrinsic graphene at room temperature, in gated graphene at sufficiently high gate voltages, and in graphene under strong optical pumping. Hydrodynamic models of electron-hole systems in semiconductors with parabolic energy spectra of electrons and holes are widely used. However, for graphene, such models need to be revised due to the linear energy spectra of electrons and holes. The hydrodynamic model of graphene was used to describe the stationary transport processes in graphene [91]. It was also used to analyze electron (or hole) plasma waves in gated graphene in a state in which the Fermi level was far from the Dirac point and quasi-neutral electron-hole sound waves in bipolar electron-hole plasma [92]. Based on this model, the DC conductivity and frequency dependent ac conductivity of graphene were calculated [93,94]. In this chapter, the hydrodynamic model is used for the first time to obtain the frequency and wave number dependent conductivity of the harmonic perturbation of moving charged carriers in graphene [95].

Electrons in graphene behave like a Dirac fluid of massless quasi-particles, propagating at a Fermi speed of about $v_f \simeq 10^6 m/s$. Therefore, the electrons in graphene mimic zero mass relativistic particles with an effective light speed of $v_f = c/3000$. The maximum drift velocity of graphene is $V_{sat} \sim 10^5 m/s$ [91]. Thus, to analyze graphene with drifting carriers, the hydrodynamic description derived from a relativistic fluid approach can be used [75]. Since electron-phonon and electron-impurity scattering have a negligible impact on the linear response of graphene over substrate at room temperature, the analyzed model is based only on electron-electron elastic scattering. Therefore, only the electron-electron

collisions are considered in the collision integral term of the Boltzman equation.

$$\frac{\partial f}{\partial t} + \mathbf{v} \cdot \nabla f + \mathbf{F} \cdot \nabla \frac{\partial f}{\partial \mathbf{p}} = \left(\frac{\partial f}{\partial t} \right)_{coll} \tag{4.1}$$

where f is the density function, F is the external force, $\mathbf{p}$ is the momentum and $\mathbf{v}$ is the particle velocity. The electrons in doped or gated graphene are modelled as a two-dimensional Fermi liquid. Graphene can be analyzed in a collision-dominated regime, $\hbar\omega << k_B T$, where collisions establish local equilibrium and the fluid is strongly correlated. The assumption of local equilibrium allows for a reduction of the Boltzmann kinetic equation for the distribution function to the hydrodynamic equations for the macroscopic variables: local density and velocity. The conservation laws for the charge density

$$\frac{\partial \rho}{\partial t} + \nabla \cdot (\mathbf{j}) = 0, \tag{4.2}$$

and the momentum density [94]

$$\frac{\mathcal{H}}{v_f^2} \left[\frac{\partial \mathbf{V}}{\partial t} + (\mathbf{V} \cdot \nabla)\mathbf{V} \right] + \nabla p + \frac{\mathbf{V}}{v_f^2} \frac{\partial p}{\partial t} - \eta \nabla^2 \mathbf{V} = \rho \mathbf{E} \tag{4.3}$$

are derived from the zeroth and first moments of the distribution function, respectively. ρ is the surface charge density, $\mathbf{V}$ is the flow velocity of the electron fluid, $\mathbf{j}$ is the surface current density, p is the pressure, $\mathcal{H} = \mathcal{E} + p$ is the enthalpy density, $\mathcal{E}$ is the energy density, and η is the shear viscosity. The Coulomb interactions between electrons are included in the viscosity of the fluid. Electrons in doped graphene with $k_B T << E_F$ behaves like a degenerate Fermi liquid with $\eta \sim \hbar\rho(\frac{E_F}{k_B T})^2$ [75].

The set of continuity (4.4) and relativistic Navir-Stocks (4.3) equations is not closed, as it contains the pressure term. The energy conservation equation which relates the energy density and the pressure to each other is obtained from the third moment of the Boltzmann equation.

$$\frac{\partial \mathcal{E}}{\partial t} + \nabla \cdot [(\mathcal{E} + p)\mathbf{V}] = 0 \tag{4.4}$$

However, this set of three hydrodynamic equations is not sufficient; an expression must be found for the energy density. In order to obtain a closed analytical expression for the conductivity only the first two hydrodynamic equations are considered. An equation of state is used to obtain approximate relations between the pressure and charge density, velocity field and other parameters.

The relativistic Navir-Stocks (4.3) equation is similar to that for the incompressible elec-

tron liquid in semiconductors [96], $\rho m_e^* \left[\frac{\partial \mathbf{V}}{\partial t} + (\mathbf{V}\cdot\nabla)\mathbf{V}\right] + \nabla p - \eta\nabla^2\mathbf{V} = \rho\mathbf{E}$, except for an extra relativistic term $\frac{\mathbf{V}}{v_f^2}\frac{\partial p}{\partial t}$. m_e^* is the effective electron mass of the semiconductor. For massless electrons in graphene, this term is replaced by $\mathcal{H}/\rho v_f^2$ which can be considered as effective electron mass of graphene. The electrons in doped graphene act like a degenerate Fermi gas. The pressure of degenerate Fermi gas can be written as

$$p = p_0 + O(\left(\frac{k_B T}{E_F}\right)^2) \tag{4.5}$$

where p_0 is the electron degeneracy pressure at zero temperature. Since in our application we are mainly interested in the high density of electrons and thus high Fermi energies ($k_B T << E_F$), the pressure is approximated with its value at zero temperature. With the aid of thermodynamic relation $U = TS + pV$ and employing the condition $T = 0$, the pressure can be obtained from this equation of state [97]

$$p = -\left(\frac{\partial U_0}{\partial A}\right)_N \tag{4.6}$$

where the subscript N is the total number of charged particles, which is assumed to remain constant during the process, A is the area of the graphene and U_0 is the internal energy at $T = 0$. This assumption is valid when the power of electromagnetic wave is not high in a way that the system remains in equilibrium (or so-called quasi-equilibrium). The internal energy is the mean value of the total energy of the system given by $U = A\int Eg(E)f(E)dE$, where $f(E)$ is the Fermi-Dirac distribution function and $g(E) = g_s g_v |E|/(2\pi(\hbar v_f)^2)$ is the energy density of states in graphene. Here, the spin and valley degeneracy are accounted by $g_s = g_v = 2$. For graphene 2DEG with linear band dispersion equation (4.6) for the pressure yields [93]

$$p = \frac{1}{3}\sqrt{\pi}\hbar v_f \rho^{2/3}(r,t) = \frac{1}{3}E_F\rho(r,t). \tag{4.7}$$

where the Fermi energy of the graphene is $E_F = \hbar v_f\sqrt{\pi\rho}$.

To find the conductivity of graphene as a function of frequency, ω, and propagation constant, β, an infinite graphene sheet lying in the y-z plane illuminated with a $\mathrm{TM_z}$ electromagnetic field is assumed, with a propagation constant of β in the z direction (Fig. 3.3), $\mathbf{E} = (E_x, E_z)e^{i\omega t}e^{-i\beta z}$. To obtain the conductivity, it is necessary to first find the

induced current density in the linear response regime, which in this case has only the z component. The longitudinal conductivity can then be defined using Ohm's law $j_z = \sigma E_z$ ($\sigma = \sigma_{zz}$).

The charge and velocity of the graphene electron fluid can be written as

$$\rho = \rho_0 + \delta\rho e^{i(\omega t - \beta z)} \tag{4.8}$$

and

$$\mathbf{V} = \mathbf{V}_d + \delta\mathbf{V} e^{i(\omega t - \beta z)}. \tag{4.9}$$

Here, ρ_0 is the electron charge density at equilibrium, $\delta\rho e^{i(\omega t - \beta z)}$ is the induced charge density, V_d is the drift velocity applied by a DC voltage (assumed to be in the z direction), and $\delta\mathbf{V} e^{i(\omega t - \beta z)}$ is the induced velocity. From this point on, the phasor form of time-space-varying variables is used to suppress the $e^{i(\omega t - \beta z)}$ term.

The linear response of the system to a small electromagnetic field perturbation is determined by considering only the first-order terms in equations 4.4 and 4.3. The induced current is

$$\mathbf{j} = \rho_0 \delta\mathbf{V} + \delta\rho\mathbf{V_d}. \tag{4.10}$$

For the pressure gradient in Eq. 4.3,

$$\nabla p = \frac{\partial p}{\partial \rho}\nabla\delta\rho \approx \frac{1}{2}E_F(\rho_0)(-i\beta\delta\rho\hat{z}) \tag{4.11}$$

where the approximation in the second equation consists of only the first-order term and assumes the Fermi energy to be effectively time and position independent. The relativistic correction term is found through

$$\frac{\mathbf{V}}{v_f^2}\frac{\partial p}{\partial t} = \frac{\mathbf{V_d}}{v_f^2}\frac{1}{2}E_F(\rho_0)(i\omega\delta\rho). \tag{4.12}$$

For small drift velocities at low frequency, this term can be neglected, and the non-relativistic Navier-Stokes hydrodynamics equation is recovered. The enthalpy density $\mathcal{H} = \mathcal{E} + p$ equals

$$\mathcal{H} = \frac{3}{2}\int_0^\infty g(E)\left(\frac{E}{e^{(E-E_F)/k_BT}+1} + \frac{E}{e^{(E+E_F)/k_BT}+1}\right)dE \tag{4.13}$$

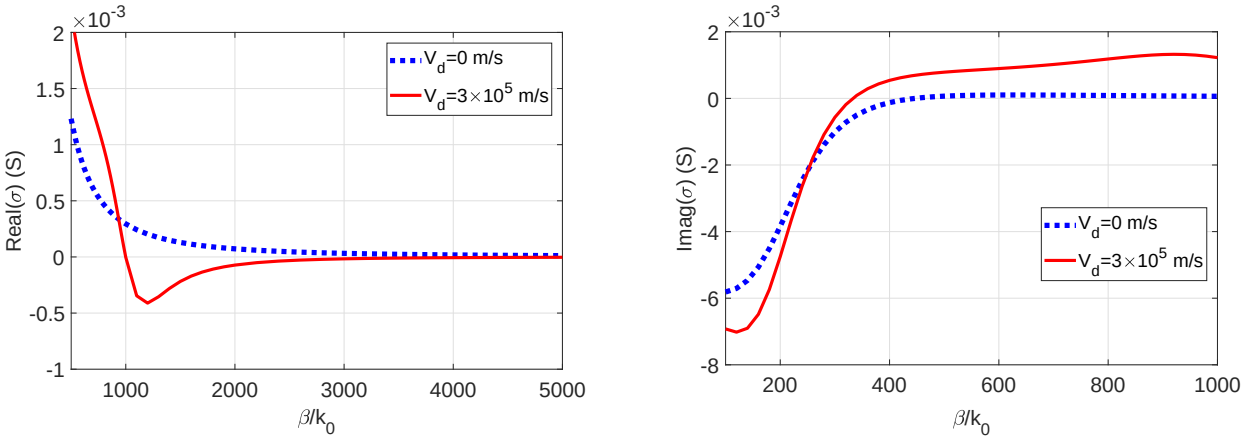

Figure 4.1: Real and imaginary parts of the conductivity versus β at $f = 1$ THz for $\mu_c = 0.3$ eV and two values $V_d = 0$ m/s(dotted line) and $V_d = 3 \times 10^5$ m/s (solid line).

in which $g(E) = g_s g_v/(2\pi(\hbar v_f)^2)$ is the energy density of states. Here, the spin and valley degeneracy are accounted for by $g_s = g_v = 2$. The Fermi energy in this equation is assumed to be constant in time and space. The prefactor $3/2$ comes from the $p = \mathcal{E}/2$ relation. At high values of chemical potential, the $\mathcal{H}$ value (Eq. 4.13) is close to its value at $T = 0$, ρE_F, which satisfies the Gibbs-Duhem relation. For example for $E_F = 0.3$ eV at $T = 300$ k, $\mathcal{H}/\rho E_F = 0.95$. By substituting equations 4.10, 4.11 and 4.12 into equations 4.4 and 4.3, it is found that

$$\sigma(\omega,\beta) = \frac{\frac{\beta^2\eta e^2}{m_{eff}^2\omega^2}A - j\frac{\rho_0 e^2}{m_{eff}\omega}\left(A^2 + \frac{\beta V_d}{4\omega} - \frac{\beta^2 E_f}{2m_{eff}\omega^2}\right)}{\left(A^2 + \frac{\beta V_d}{3\omega} - \frac{\beta^2 E_f}{2m_{eff}\omega^2}\right)^2 + \left(\frac{\eta\beta^2}{m_{eff}\omega\rho_0}A\right)^2} \tag{4.14}$$

in which $A = 1 - \beta V_d/\omega$ and $m_{eff} = E_F(\rho_0)/v_f^2$. The conductivity of graphene for $V_d = 0$ is

$$\sigma(\omega,\beta,V_d = 0) = \frac{\frac{\beta^2\eta e^2}{m_{eff}^2\omega^2} - j\frac{\rho_0 e^2}{m_{eff}\omega}\left(1 - \frac{\beta^2 E_f}{2m_{eff}\omega^2}\right)}{\left(1 - \frac{\beta^2 E_f}{2m_{eff}\omega^2}\right)^2 + \left(\frac{\eta\beta^2}{m_{eff}\omega\rho_0}\right)^2} \tag{4.15}$$

As expected the non-biased graphene ($V_d = 0$) is always lossy for all frequencies and phase velocities.

In Fig. 4.1, the real and imaginary parts of the conductivity versus β are plotted at $f = 1$ THz for $\mu_c = 0.3$ eV and two values: $V_d = 0$ (dotted line) and $V_d = 3 \times 10^5$ m/s

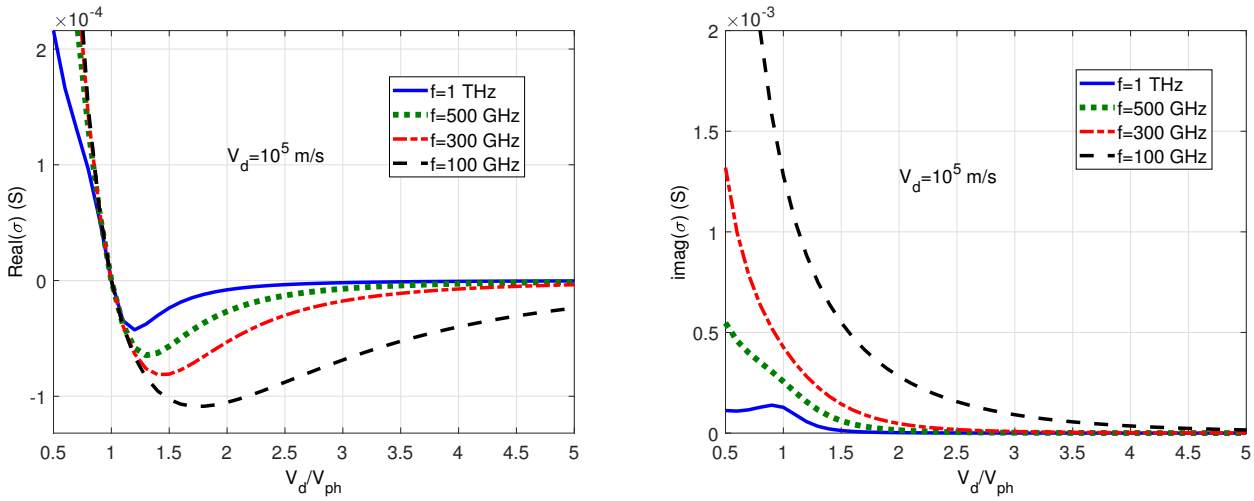

Figure 4.2: Real and imaginary parts of conductivity versus V_d/V_{ph} at frequencies of 0.1, 0.3, 0.5 and 1 THz for a drift velocity of $V_d = 10^5 m/s$.

(solid line). The result of this figure can be compared with the similar result of Fig. 3.4 obtained from quantum mechanical model. remarkable similarity excits between these two results. Here again, it can be seen that the real part of the conductivity is negative for $V_d = 3 \times 10^5$ m/s and for $\beta > 1000k_0$ which corresponds to $V_{ph} < V_d$. As expected, the non-biased graphene is always lossy for every value of frequency and wavenumber. Also, the imaginary part of the conductivity is negative only for small values of β ($\beta < 380k_0$ for $V_d = 0$ and $\beta < 440k_0$ for $V_d = 3 \times 10^5$ m/s).

The real and imaginary parts of the conductivity versus the normalized reciprocal value of the phase velocity at different values of frequency are plotted in Fig. 4.2(a) and (b). The phase velocity is normalized to a drift velocity of $V_d = 10^5 m/s$. The results show that in biased graphene ($V_d \neq 0$) for $\beta/\beta_e > 1$, or equivalently, for a drift velocity larger than the phase velocity, $V_d/V_{ph} > 1$, graphene changes from a lossy propagating medium with a positive real part of conductivity to a gain medium with a negative real part of conductivity. In this case, the power transfers from the DC power to the electromagnetic field.

The real and imaginary parts of the conductivity versus frequency for different values of drift velocity are plotted in Fig. 4.3 where $E_f = 0.3$ eV. The wavenumber for all curves is $\beta = 2\pi/d, d = 100nm$. This is consistent with the wavenumber of the first-order harmonic of a periodic structure with the period of $d = 100nm$. In the proposed graphene travelling wave amplifier, a periodic grating structure is used to generate a slow electromagnetic

wave. The propagation constant of the first-order harmonic of this structure is $\beta_1(\omega) = \beta_0(\omega) + 2\pi/d$, in which $\beta_0(\omega)$ is the frequency-dependent propagation constant of the fundamental wave. The d values of the periodic slow wave structure should be in the range of few hundreds of nanometres or less to meet the amplification requirement of a graphene travelling wave amplifier. In this range of d values, it is a sufficient approximation to consider $\beta_1 \simeq 2\pi/d$ to be frequency independent.

The results displayed in Fig. 4.3 shows that the amount of gain and the frequency range at which amplification is possible are increased significantly by increasing the value of the drift velocity.

In Fig. 4.3, the real and imaginary parts of the conductivity are plotted versus the frequency for different values of Fermi energy, with $\beta = 2\pi/(d = 100nm)$ and $V_d = 10^5 m/s$. Raising the Fermi energy level leads an increase in the absolute value of the negative conductivity and gain. However, as the Fermi energy increases, the frequency range at which the real part of the conductivity is negative (making amplification possible) does not change. An increase in the Fermi energy leads to an increase in the density of electrons, enhancing the transfer of energy from the electrons to the electromagnetic field. Since the exact value of viscosity, η, is not accurately known in the proposed analytical model, typical values have been used in the conductivity equations. The effect on conductivity of changing the viscosity from half to twice its typical value is depicted in Fig. 4.5. Changes in η alter the bandwidth and gain simultaneously.

4.1 Conclusion

In this chapter, a hydrodynamic model, derived from a relativistic fluid approach, was used to find the current induced by a harmonic perturbation of drifting charge carriers in graphene. The induced charge density and velocity were assumed to be significantly smaller than the total charge density and the drift velocity applied by the DC bias to obtain the conductivity in the linear region.

The obtained results are consistent with the results of the previous chapter. Both methods show that the negative conductivity and thus gain is obtained for drift velocities slightly greater than the phase velocity of the incident field. Although the two methods are quite different, one being more classical and the other more quantum mechanical, the behaviour of the two conductivity functions with respect to the frequency and wavenumber are remarkably similar.

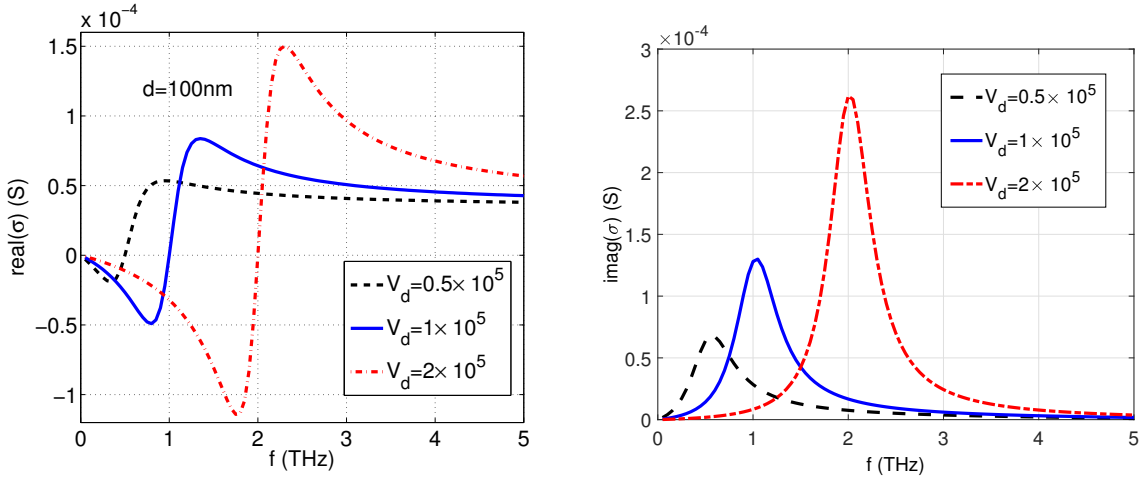

Figure 4.3: Real and imaginary parts of conductivity versus frequency for drift velocities of $V_d = 0.5, 1, 2 \times 10^5 m/s$ where $E_f = 0.3$ eV. The propagation constant is assumed to be frequency independent and equals $\beta = 2\pi/d, d = 100nm$ for all curves .

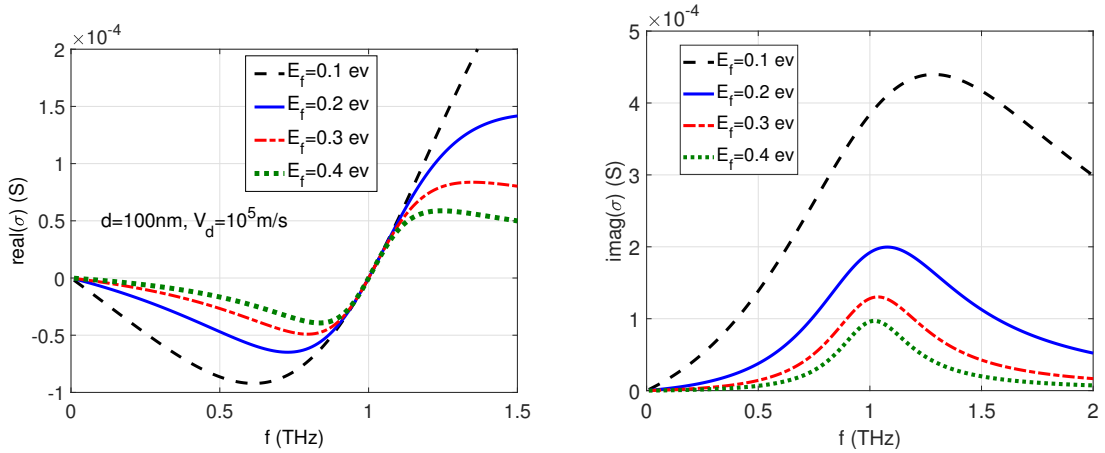

Figure 4.4: Real and imaginary parts of conductivity versus frequency for different values of Fermi energy where $V_d = 10^5 m/s$ and $\beta = 2\pi/d, d = 100nm$.

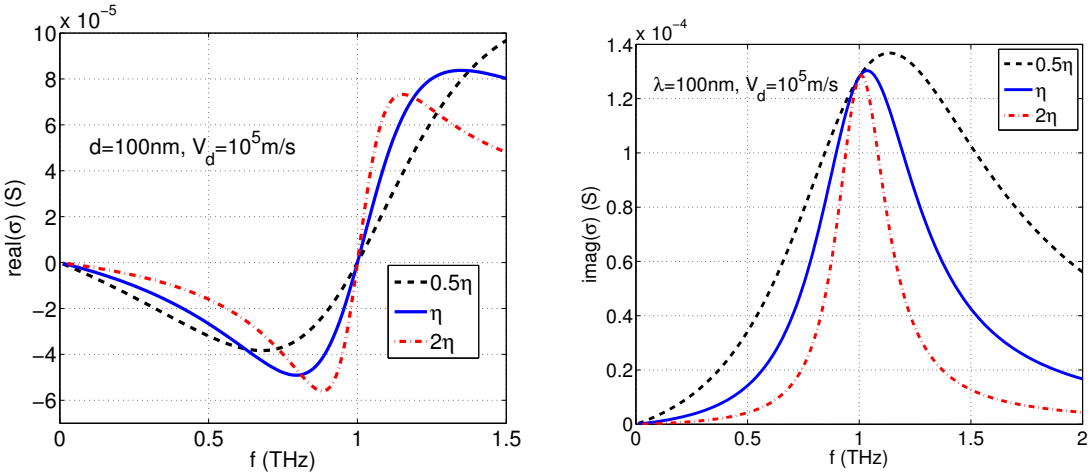

Figure 4.5: Real and imaginary parts of conductivity versus frequency for different values of viscosity where $V_d = 10^5$ m/s, $E_f = 0.3$ eV and $\beta = 2\pi/d, d = 100nm$.

Chapter 5

Analysis of travelling-wave amplifier using graphene

The quantum mechanical and hydrodynamic analysis of graphene that were presented in the previous chapters show that travelling-wave amplification is possible in graphene. The next step is to design a structure to demonstrate and apply this fascinating property of graphene. Under certain conditions, when the charged particles in graphene move at a higher velocity than an electromagnetic wave, energy transfers from the charged particles to the electromagnetic field. The maximum drift velocity in the graphene is in the order of 105m/s. The higher order space harmonics of a periodic waveguide can reach this level of phase velocity. The ability to fabricate dielectric waveguides with very short period grating make it possible to use low-velocity charged-particle currents like drifting carriers in graphene.

In this chapter, a slow-waveguide structure is proposed in which the graphene layer is placed right next to the periodic layer; hence, capitalizing on the maximum coupling between the electromagnetic field and the drifting space charge wave in graphene (Fig. 5.1). The waveguide is fabricated from high-resistivity silicon; such silicon having very low loss at the THz range of frequencies [98, 99].

An approximate analytic solution is presented for electromagnetic wave propagation in a periodic structure in the presence of graphene. The analytic approximate expressions show the effect of each parameter individually on the overall gain of the structure. Therefore, this approach provides insights for designing and optimizing the structure. Such transparency is not achievable when using numerical calculations.

Below, the electromagnetic wave propagation in both a slab and a rectangular waveg-

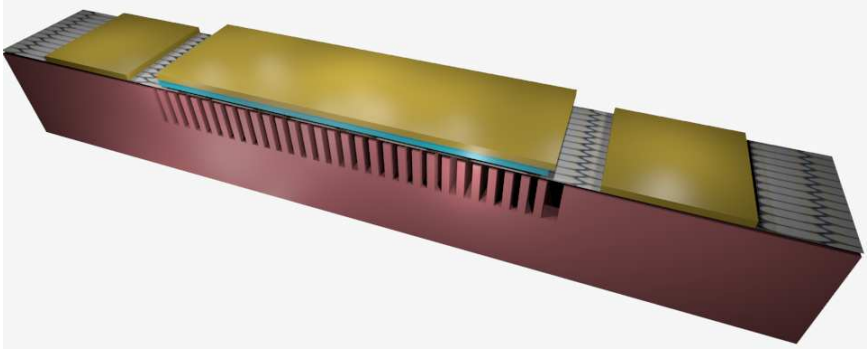

Figure 5.1: Proposed structure is a high-resistivity silicon waveguide with a grating etched on its top surface covered by a graphene sheet onto which metal contacts are attached

uide with a grating on the top surface is analyzed in terms of a Floquet mode solution. This method has been described by Gover and Yariv in [73, 100]. First-order approximate recursive analytical expressions for the space harmonics are obtained. The calculation in [73] was presented only for slab waveguides and the grating structure was modelled by a semi-infinite inhomogeneous layer. Therefore, the finite corrugation depth was not considered in the calculations. Here, the aforementioned method is generalized to a three-layer structures to model the effect of the grating depth accurately. A more generalized method is then used to analyze rectangular waveguides; more practically applicable with respect to slab waveguides. Slab waveguide analysis provides good approximations when the width of a structure is significantly larger than its thickness.

5.1 Analysis of general coupling in a periodic structure

In this section, a general analysis of wave interaction in a periodic structure using Floquet Bloch formalism is presented. Then, in the following two sections, this analysis is applied to two specific cases of coupling interaction in periodic slab and rectangular structures. Coupled mode theory for TWAs was first presented by Pierce and Louisell [101,102]. Later, Yariv and others developed coupled-mode formalism for wave interactions in dielectric waveguides [103–106].

There are two different approaches to studying coupling in periodic dielectric waveguides. In the first approach, the eigenmodes of the structure are the eigenmodes of the

uniform waveguide in the absence of periodic perturbation, and the periodic perturbation is the coupling perturbation that couples the eigenmodes of the uniform waveguide. For example, two modes with propagation constants β_A and β_B can be coupled to each other if the period of the periodic perturbation, d, satisfies: $2\pi/d = \beta_A - \beta_B$ [103, 104].

In the second approach-the approach used in this thesis-the eigenmodes of the structure are the Floquet-Bloch eigenmodes between which coupling takes place. These eigenmodes are coupled to each other by introducing another perturbation. This approach is described in detail in [73]. The travelling wave interaction in a periodic dielectric waveguide is analyzed using this approach, in which the external current acts as a perturbation. In a TWA, this current can be written as:

$$\mathbf{J} = \mathbf{J_e}(x, y)e^{-j\beta z}. \tag{5.1}$$

Assume a Floquet mode E_A with the Floquet expansion of

$$\mathbf{E_A} = \Sigma_m \mathbf{E_{A_m}}(x, y)e^{-j\beta_m^A z} \quad \beta_m^A = \beta_0^A + m\frac{2\pi}{d} \tag{5.2}$$

if for its first-order space harmonic $\beta_1^A \simeq \beta$, then after applying the external current (eq. 5.1) this mode will be predominantly excited and its amplitude will grow slowly. Therefore, the excited electric field can be written as:

$$\mathbf{E} = G(z)\mathbf{E_A} \tag{5.3}$$

where $G(z)$ is a slowly varying function obtained from:

$$G(z) = -j\frac{e^{-j\Delta\beta_1 z}}{4P_{A0}\Delta\beta_1}\int_{-\infty}^{\infty}\int_{-\infty}^{\infty} dxdy\mathbf{E}_{\mathbf{A_1}}^*(x, y)\cdot\mathbf{J_e}(x, y) \tag{5.4}$$

where $\Delta\beta_1 = \beta - \beta_1^A \approx 0$ and P_{A0} is the total average z-directed power carried by the fundamental harmonic. The detailed derivation of $G(z)$ is given in Appendix B.

By substituting $G(z)$ in eq. B.5 for the particular synchronous space harmonic field, $E_1(x, z)$, we find

$$\mathbf{E_1} = \frac{-j}{4P_{A0}\Delta\beta_1}\mathbf{E_{A_1}}(x, y)e^{-j\beta z}\int_{-\infty}^{\infty}\int_{-\infty}^{\infty} dxdy\mathbf{E_{A_1}}^*(x, y)\cdot\mathbf{J_e}(x, y) \tag{5.5}$$

For graphene, a zero thickness sheet, the current is a Dirac delta function of x. There-

fore, the integral with respect to x equals:

$$\int_{-\infty}^{\infty} dx \mathbf{E_{A_1}}^*(x,y) \cdot \mathbf{J_e}(x,y) = \mathbf{E_{A_1}}^*(x_g,y) \cdot \mathbf{J_s}(y) \tag{5.6}$$

where x_g is the location of the graphene sheet and $\mathbf{J_s}(y)$ is the current at the surface of the graphene. For a slab waveguide (assumed to be invariant in the y direction), eq. 5.5 is simplified to

$$E_1(x_g) = j\frac{|\mathbf{E_{A_1}}(x_g)|^2}{4P_{A0_w}(\beta_1^A - \beta)}\mathbf{J_s} \tag{5.7}$$

where $\mathbf{E_{A_1}}(x_g)$ is the field of the first-order space harmonic (in the absence of interaction) at the point where the interaction with the charged carrier sheet (placed at $x = x_g$) takes place. P_{A0_w} is the average z directed power per unit width carried by the fundamental harmonic.

If one assumes $\beta_1^A \simeq \beta$, it is possible to show that this equation is consistent with the Pierce equation

$$E_1 = j\frac{\beta^2\beta_1 K_1}{\beta_1^2 - \beta^2} I \tag{5.8}$$

where K_1 is the interaction impedance given by

$$K_1 = \frac{|E_{A_1}|^2}{2\beta_1^2 P_A} \tag{5.9}$$

The interaction impedance determines the strength of coupling between the electric field in the periodic and the space charge wave. This parameter is proportional to $\frac{P_{A1}(x_g)}{P_A}$ where $P_{A1}(x_g)$ is the power of the space harmonic synchronous with the drifting charge density wave at the interaction point, and P_A is the total z-directed power of the Floquet mode E_A.

As discussed above, to obtain the interaction impedance, the field at the point where the graphene is located should first be determined in the absence of interaction. Therefore, in the next sections, modal analysis is used to find the electromagnetic field in the periodic slow-wave structures alone, with no graphene sheet.

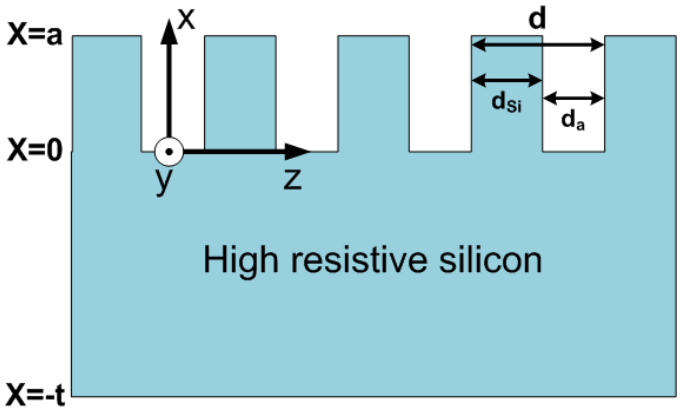

Figure 5.2: Periodic waveguide with rectangular corrugation

5.2 Analysis of Floquet modes in a slab dielectric waveguide with a grating on top

The structure under investigation is a silicon slab waveguide with thin surface corrugation (see Fig. 5.2).

The structure is assumed to be infinite in the y direction. Although the proposed structure supports both TE and TM modes, only the TM modes, $\mathbf{e_m} = e_{x,m}\hat{x} + e_{z,m}\hat{z}$ with a longitudinal electric field component are considered due to the particular modal excitation mechanism and the fact that the z-directed plasma wave can be modulated only by the z-component of the field.

For a periodic layer with the dielectric constant $\epsilon(z)$ function of z, the wave equation for the magnetic field of the TM mode, $\mathbf{H} = H_y\hat{y}$, is [73]

$$\frac{\partial^2 H_y}{\partial x^2} + \frac{\partial^2 H_y}{\partial z^2} - \frac{d\ln\epsilon}{dz}\cdot\frac{\partial H_y}{\partial z} + \omega^2\mu\epsilon(z)H_y = 0 \tag{5.10}$$

The relative dielectric constant of a thin periodically perturbed layer, $\epsilon_g = \epsilon_0\epsilon_{rg}$, can be approximated by the first two terms of its Fourier series,

$$\epsilon_{rg}(z) = \epsilon_{rg0} + \epsilon_{rg1}\cos(\frac{2\pi}{d}z) \tag{5.11}$$

Therefore, we have

$$-\frac{d\ln\epsilon_{rg}}{dz} \simeq g_1 \sin(\frac{2\pi}{d}z) \tag{5.12}$$

For the corrugated surface of Fig. 5.2 with the filling factor $f_d = d_{Si}/d$, $(d_{Si} + d_a = d)$, we have

$$\epsilon_{rg0} = f_d\epsilon_{Si} + (1 - f_d)\epsilon_{air}, \tag{5.13a}$$

$$\epsilon_{rg1} = \frac{2}{\pi}(\epsilon_{Si} - \epsilon_{air})\sin(f_d\pi), \tag{5.13b}$$

$$g_1 = \frac{4}{d}\sin(f_d\pi)\ln\left(\frac{\epsilon_{Si}}{\epsilon_{air}}\right). \tag{5.13c}$$

Substituting the Floquet expansion of H_y,

$$H_y = \sum_m a_m(x)e^{-j\beta_m z} \tag{5.14}$$

along with the first-order Fourier expansion of the periodic terms (eq. 5.11 and 5.12) into eq. 5.10 yields [73]

$$e^{-j\beta_0 z}\sum_m e^{-jm\frac{2\pi}{d}z}\left[a_m''(x) + \left(k^2\epsilon_{rg0} - \beta_m^2\right)a_m(x) + \frac{1}{2}\left(k^2\epsilon_{rg1} + \beta_{m-1}g_1\right)a_{m-1}(x) + \right.$$
$$\left.\frac{1}{2}\left(k^2\epsilon_{rg1} - \beta_{m+1}g_1\right)a_{m+1}(x)\right] = 0 \tag{5.15}$$

From the uniqueness theorem of the Fourier expansion we get [73]

$$a_m''(x) + \left(k^2\epsilon_{rg0} - \beta_m^2\right)a_m(x) + \frac{1}{2}\left(k^2\epsilon_{rg1} + \beta_{m-1}g_1\right)a_{m-1}(x) +$$
$$\frac{1}{2}\left(k^2\epsilon_{rg1} - \beta_{m+1}g_1\right)a_{m+1}(x) = 0 \tag{5.16}$$

where $a_m''(x) = \partial^2 a_m/\partial x^2$. In this equation each space harmonic is coupled to the next higher and lower harmonics. The field solutions should satisfy the wave equations in each

layer of the waveguide

$$a_m''(x) - \alpha_m^2 a_m(x) = 0 \qquad x < -t \quad , \quad x > a \tag{5.17}$$

$$a_m''(x) - \delta_m^2 a_m(x) = -\frac{1}{2}\left(k^2\epsilon_{rg1} + \beta_{m-1}g_1\right)a_{m-1}(x) - \frac{1}{2}\left(k^2\epsilon_{rg1} - \beta_{m+1}g_1\right)a_{m+1}(x) \qquad 0 < x < a \tag{5.18}$$

$$a_m''(x) + h_m^2 a_m(x) = 0 \qquad 0 > x > -t \tag{5.19}$$

in which

$$\alpha_m^2 = \beta_m^2 - k^2\epsilon_{air} \tag{5.20}$$
$$\delta_m^2 = \beta_m^2 - k^2\epsilon_{rg0} \tag{5.21}$$
$$h_m^2 = k^2\epsilon_{Si} - \beta_m^2 \tag{5.22}$$

In addition to meeting equations 5.17-5.19, the field solutions should meet the boundary conditions [i.e., the continuity of H_y and E_z at the interfaces x=-t, 0, and a (see Fig. 5.2)]. The continuity condition of H_y leads to continuity of the space harmonics $a_m(x)$

$$a_m(a^-) = a_m(a^+) \tag{5.23}$$
$$a_m(0^-) = a_m(0^+) \tag{5.24}$$
$$a_m(-t^-) = a_m(-t^+) \tag{5.25}$$

The continuity of $E_z = (-j/\omega\epsilon)\partial H_y/\partial x$ gives us

$$a_m'(a^-) = \frac{\epsilon_{rg0}}{\epsilon_{air}}a_m'(a^+) + \frac{\epsilon_{rg1}}{2\epsilon_{air}}[a_{m-1}'(a^+) + a_{m+1}'(a^+)] \tag{5.26}$$
$$a_m'(0^+) = \frac{\epsilon_{rg0}}{\epsilon_{Si}}a_m'(0^-) + \frac{\epsilon_{rg1}}{2\epsilon_{Si}}[a_{m-1}'(0^-) + a_{m+1}'(0^-)] \tag{5.27}$$
$$a_m'(-t^+) = \frac{\epsilon_{Si}}{\epsilon_{air}}a_m'(-t^-) \tag{5.28}$$

The + (−) index of a, 0 and -t is used for the field immediately above (below) the interfaces. The exact solution of the set of equations presented here is rather complicated. Therefore, the first-order approximation is applied, in which higher-order spatial harmonics are neglected relative to lower-order harmonics. For example, to obtain the solution for

the first-order harmonic (m=1), the second term (a_2) on the right-hand side of equations 5.18, 5.26 and 5.27 is neglected with respect to a_0. Furthermore, it is assumed that the zero-order harmonic is much larger than the other harmonics and is approximately equal to the unperturbed waveguide solution.

The magnetic field distribution of the first TM mode of the unperturbed waveguide (Fig. 5.2 $a = 0$) $H_y = a(x)e^{j\beta z}$ can be written as

$$a(x) = A_0 e^{-\alpha_0 x} \qquad x > 0 \tag{5.29a}$$

$$a(x) = B_0 \cos h_0(x + t/2) \qquad -t < x < 0 \tag{5.29b}$$

$$a(x) = A_0 e^{\alpha_0(x+t)} \qquad x < -t \tag{5.29c}$$

For thin gratings, it can be assumed that most of the power is carried by the fundamental harmonic and $P_A \simeq P_{A0}$. The total z directed power per unit width carried by the first TM mode of the slab waveguide is obtained from the following equation

$$P_{A0_w} = \frac{P_{A0}}{w} = \frac{A_0^2 \beta}{4\omega\epsilon_0}\left(\frac{t}{2n_g^2\cos^2(h_0 t/2)} + \frac{\tan(h_0 t/2)}{n_g^2 h_0} + \frac{1}{\lambda_0 \epsilon_{air}}\right) \tag{5.30}$$

5.2.1 First-order space harmonic

For large values of $2\pi/d$, the case in our application, the parameter h_1 in eq. 5.22 becomes imaginary

$$\kappa_1 = \left(\beta_1^2 - k^2\epsilon_{Si}\right)^{1/2} \tag{5.31}$$

Therefore, for $\kappa_1 t >> 1$, we can assume that the field distribution that satisfies the wave equations of 5.17-5.19 can be written as

$$a(x) = \begin{cases} A_1 e^{-\alpha_1(x-a)} & x > a \\ D_1\cosh(\delta_1 x) + E_1\sinh(\delta_1 x) - \dfrac{k^2\epsilon_{rg1} + g_1\beta_0}{2(\alpha_0^2 - \delta_1^2)}A_0 e^{-\alpha_0 x} & 0 < x < a \\ B_1 e^{\kappa_1 x} & x < 0 \end{cases} \tag{5.32}$$

in which the a_0 term in eq. 5.18 is approximated by eq. 5.29a. By applying boundary conditions (equations 5.23, 5.24, 5.26 and 5.27) at $x = 0$ and $x = a$ interfaces (see Fig.

5.2) we find the following expressions for coefficient A_1

$$
\begin{aligned}
A_1 &= \frac{M_1 M_4 - M_2 M_3}{M_1 - M_3} A_0 \\
M_1 &= \cosh(\delta_1 a) + \frac{\epsilon_{rg0}}{\epsilon_{Si}} \frac{\kappa_1}{\delta_1} \sinh(\delta_1 a) \\
M_2 &= \frac{k^2 \epsilon_{rg1} + g_1 \beta_0}{2(\alpha_0^2 - \delta_1^2)} \left(\cosh(\delta_1 a) - \frac{\gamma_0}{\delta_1} \sinh(\delta_1 a) - e^{-\gamma_0 a} \right) - \frac{n_{lp}^2}{2\epsilon_{air}} \frac{\gamma_0}{\delta_1} \sinh(\delta_1 a) \\
M_3 &= -\frac{\epsilon_{air} \delta_1}{\epsilon_{rg0} \gamma_1} \sinh(\delta_1 a) - \frac{\epsilon_{air} \kappa_1}{\epsilon_{Si} \gamma_1} \cosh(\delta_1 a) \\
M_4 &= -\frac{\epsilon_{air} \delta_1}{\epsilon_{rg0} \gamma_1} \frac{k^2 \epsilon_{rg1} + g_1 \beta_0}{2(\alpha_0^2 - \delta_1^2)} \sinh(\delta_1 a) + \frac{\epsilon_{rg1} \gamma_0}{2\epsilon_{rg0} \gamma_1} \cosh(\delta_1 a) + \\
&\quad \frac{\epsilon_{air} \gamma_0}{\epsilon_{rg0} \gamma_1} \frac{k^2 \epsilon_{rg1} + g_1 \beta_0}{2(\alpha_0^2 - \delta_1^2)} \left(\cosh(\delta_1 a) - e^{\gamma_0 a} \right)
\end{aligned}
\tag{5.33}
$$

5.2.2 Gain and dispersion equations

The travelling wave interaction can be described as a coupled wave problem. The z component of the slow-wave field modulates the drifting carriers in graphene and generates a carrier plasma wave. The plasma wave in turn induces the electromagnetic wave. Calculating each of these processes separately and combining them self consistently results in the dispersion equation. In the previous chapters, we obtained the conductivity of graphene. It defines defines the relation between the induced current, $\mathbf{J}(z) = J_{z1}(\beta, \omega) e^{j(\omega t - \beta z)}$, and the external field $E_{z1}(z) = E_{z1} e^{j(\omega t - \beta z)}$

$$
J_{z1}(\beta, \omega) = \sigma(\beta, \omega) E_{z1} \tag{5.34}
$$

and in section 5.1 the field of the excited space harmonic synchronized with the excited current variation was obtained (eq. 5.7). By substituting eq. 5.34 into eq.5.7, we obtain

$$
j \frac{|\mathbf{E_{A_1}}(x_g)|^2}{4 P_{A0_w} (\beta_1 - \beta)} \sigma(\beta, \omega) = 1, \tag{5.35}
$$

in which $\beta_1 = \beta_0 + 2\pi/d$ is the propagation constant of the first-order space harmonic in

the absence of charge carriers. If we assume $\beta = \beta_1 + \Delta\beta$, we get

$$\Delta\beta = -j\frac{|\mathbf{E_{A_1}}(x_g)|^2}{4P_{A0_w}}\sigma(\beta,\omega) \tag{5.36}$$

The imaginary part of the propagation constant β gives the intensity gain $g = 2Im\beta$. In the absence of the coupling and any loss, β_1 is a real number. Therefore, it can be written that

$$Im\beta = Im\Delta\beta = -\frac{|\mathbf{E_{A_1}}(x_g)|^2}{4P_{A0_w}}Real(\sigma) = -\frac{1}{2}K_1\beta_1^2 Real(\sigma) \tag{5.37}$$

In this equation, $E_{A_1}(x_g = a)$ equals A_1^2 given in eq. 5.33 and P_{A0_w} is given in eq. 5.30.The term $K1 = \frac{|\mathbf{E_{A_1}}(x_g)|^2}{2\beta_1^2 P_{A0_w}}$ in eq. 5.37 is the interaction impedance of a top-grated slab waveguide. As discussed in section 5.1, this term indicates the coupling strength between the space charge wave and the electromagnetic wave. For maximum gain, the optimized values of waveguide parameters t, a and f_d should be found. This gives the maximum value of this coupling term. Figure 5.3 shows the value of $K_1\beta_1^2$ as a function of t for different values of a, d and f_d at $f = 1THz$.The Fourier series expansion coefficients of the periodic electromagnetic field depend on the value of f_d. The amplitude of the second order harmonic is maximized by choosing the right value of f_d.

From the results of Fig. 5.3, it can be deduced that maximum coupling occurs at $t \simeq 0.15\lambda$ for $f_d = 0.3$ and $a > d$. Figure5.3(a) shows that the coupling factor is higher for deeper gratings. However, the coupling factor does not change for $a > d$, since the super slow wave decays rapidly away from the interface of the grating (see Fig. 5.4). Thus, for large values of a, the grating can be modelled as a two-layer structure. The fabrication of deep gratings, especially gratings with $a > 3d$, is challenging. However, this result [Fig. 5.3(a)] shows that such a deep grating is not required to get the maximum coupling factor.

The 2D grating structure is simulated using COMSOL Multiphysics modeling software. The $K_1\beta_1^2$ values obtained from the simulation are plotted versus t/λ for $a = 200$ nm, $d = 200$ nm, $f_d = 0.3$ and $f = 1$ THz in Fig. 5.3 (circle markers). These results are consistent with the approximated theoretical results (solid blue line). In Figure 5.4, the longitudinal component of the electric field, E_z is plotted versus z at the interface of the grating and at a distance of a above and $a/2$ below the interface given $d = 200$ nm, $a = 200$ nm, $f_d = 0.3$, $t = 46\mu$m and $f = 1$ THz. The field at the interface of the grating mainly consists of the first- and second-order space harmonics. However, the second-order space harmonic is a surface wave that decays rapidly away from the interface. As shown in Figure

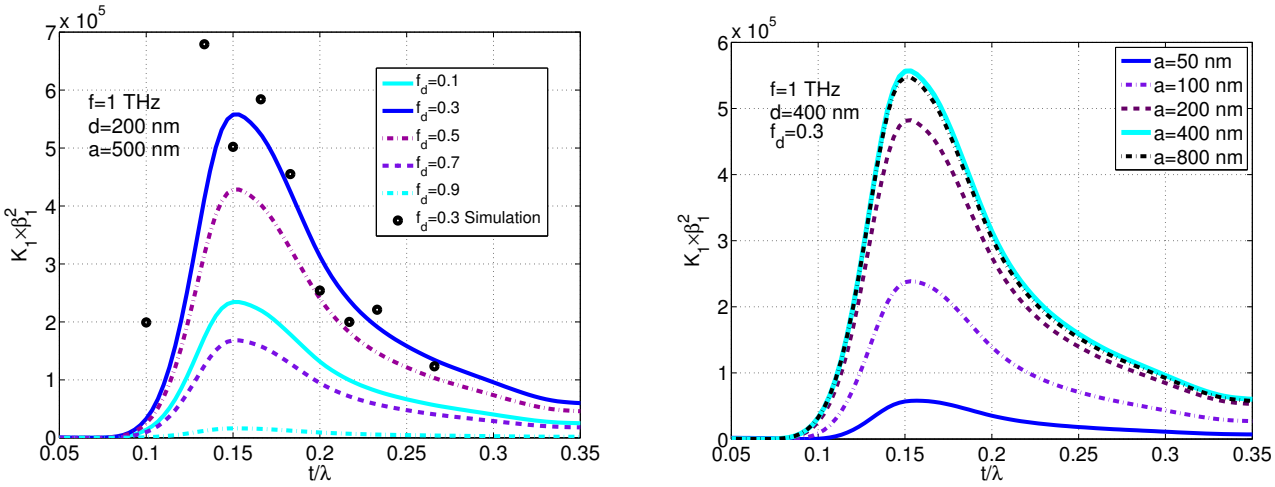

Figure 5.3: $K_1\beta_1^2$ as a function of t/λ for different values of a, d and f_d at $f = 1THz$. (Blue dots in (a) are obtained from COMSOL simulation results, for $a = 200nm$, $d = 200nm$ and $f_d = 0.3$).

5.4, the second order harmonic almost vanishes at $x = a$ and $x = -a/2$.

By substituting eq. 4.14 into eq. 5.37, and assuming $\beta \simeq \beta_1$, we find the intensity gain for different values of the chemical potential of graphene and drift velocities. The results at two different frequencies, $f = 300$ GHz and 1 THz, are presented in Figures 5.5 and 5.6. In these plots, the dimensions of the grating structure are $t/\lambda = 0.15$, $f_d = 0.3$ and a=d. With these dimensions, the maximum interaction impedance is obtained at each point and changes slightly with d (less than %0.4 of its maximum). Therefore, the change in intensity gain comes mainly from the change in the gain of the active medium, graphene, represented by its conductivity in eq. 5.37.

Figure 5.5 shows that increasing the density of electrons (and consequently the chemical potential), increases the intensity gain and thus the power delivered through the space charge wave to the electromagnetic field. The maximum of each curve is obtained at the point where the corresponding $\frac{V_{ph}}{V_d}$ results in the minimum value of the negative conductivity of graphene (see Fig. 4.2). For example, for $E_f = 0.3$ eV and $V_d = 3 \times 10^5$ m/s at $f = 1$ THz, the maximum gain is achieved at $d = 254$ nm. For very small values of the period, d, the phase velocity can be approximated by $V_{ph} \simeq fd$. Therefore, at $d = 254$ nm, $V_d/V_{ph} \simeq 1.2$ gives the maximum amplitude of the negative real part of the graphene conductivity (Fig. 4.2)

Figure 5.6 shows that for larger values of V_d, the maximum gain is increased and

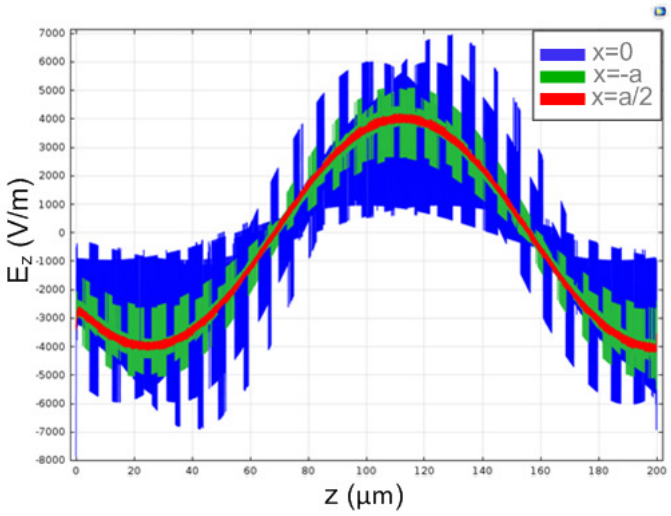

Figure 5.4: The longitudinal component of the electric field, E_z, versus z at the interface of the grating and at the distance of a above and $a/2$ below the interface at the frequency of $f = 1$ THz given $d = 200$ nm, $a = 200$ nm, $f_d = 0.3$, $t = 46\mu$m.

obtained at larger values of d and phase velocity. These results can be justified by the variation of the graphene conductivity with respect to V_d, shown in Fig. 4.3.

The maximum graphene drift velocity reported in the literature varies from $2 \times 10^5 m/s$ to $5.4 \times 10^5 m/s$ [107] [108] [109]. For example, for $V_d = 3 \times 10^5 m/s$, the maximum gain is obtained at $d = 254nm$. The fabrication of a grating with a period of $100nm$ or greater is feasible with currently available electron-beam lithography techniques.

Figure 5.7 shows the intensity gain versus frequency given optimized waveguide dimensions. In this figure, the Fermi energy and drift velocity of graphene are $V_d = 3 \times 10^5 m/s$ and $E_f = 0.3$ eV. The maximum intensity gain is $g = 10.53dB/cm$. The $3dB$ bandwidth for $1cm$ is around $190GHz$, showing that the proposed TWA is wideband.

5.3 Analysis of graphene traveling wave amplifier on a rectangular dielectric waveguide

In the previous section, we assumed that the grating and the silicon slab are infinite in the xy plane. Such 2D assumptions are not applicable for practical device design. A more-realistic structure to consider is a rectangular waveguide with a grating etched on its top

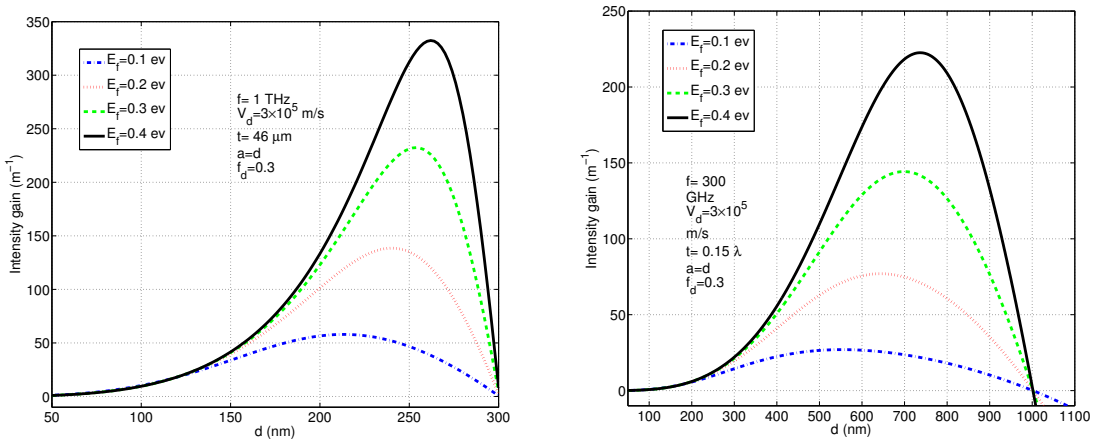

Figure 5.5: Intensity gain as a function of d (a) for different values of chemical potential given $t = 0.15\lambda$, $a = d$, $f_d = 0.3$ and $V_d = 3 \times 10^5$ m/s and (b)for different values of drift velocity given $t = 0.15\lambda$, $a = d$, $f_d = 0.3$ and $E_f = 0.3$ eV $f = 1$ THz (right) and $f = 300$ GHz (left)

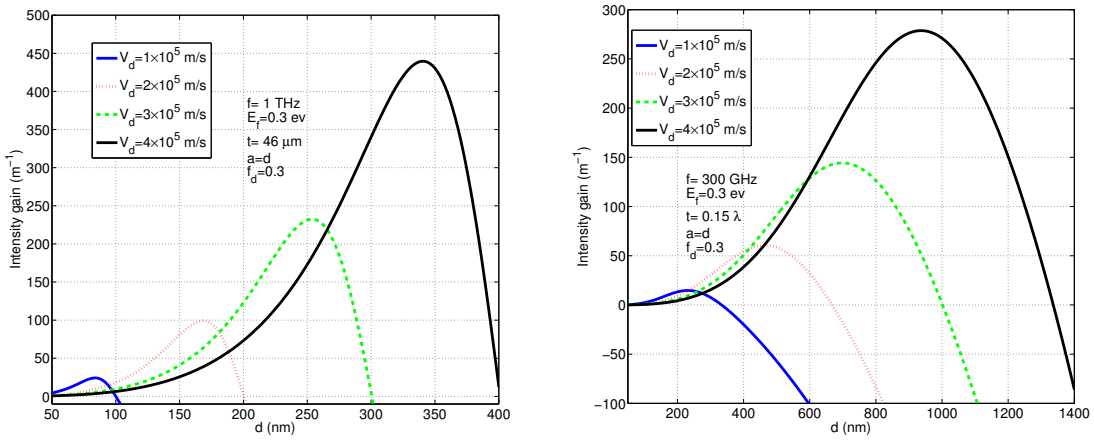

Figure 5.6: Intensity gain as a function of d for different values of drift velocity given $t = 0.15\lambda$, $a = d$, $f_d = 0.3$ and $E_f = 0.3$ eV at two different frequencies $f = 1$ THz (right) and $f = 300$ GHz (left)

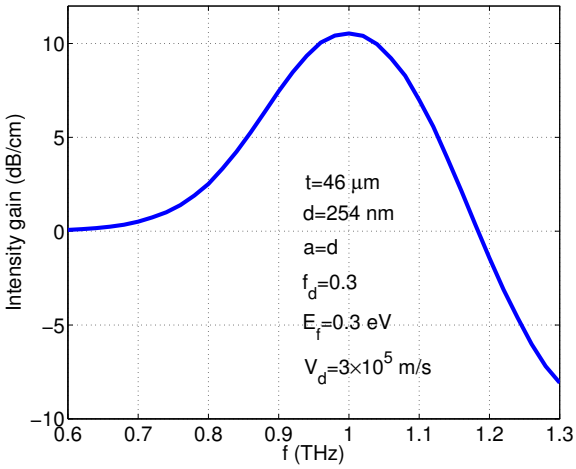

Figure 5.7: Intensity gain as a function of frequency

surface covered by a graphene sheet onto which metal contacts are later attached (see Fig. 5.1).

There is no analytical solution for the dispersion equation and field profiles of rectangular dielectric waveguides. Therefore, numerical methods such as the film mode matching method [110], circular harmonics computer analysis [111], variational mode expansion method [112], finite element method (FEM) [113], or finite-difference method [114], can be applied to obtain an accurate value for these quantities. However, these numerical methods do not give closed form analytical expressions to describe the effect of each parameter on the whole performance of the system. An analytical model is more useful for gaining insights into the physics of a device, and for conducting fast explorative simulations.

Another way to analyze rectangular dielectric waveguides is to employ approximate methods such as the effective index and Marcatili methods [115, 116]. Marcatili's approximate analytical approach has been used in many studies on optical waveguide theory [117–120]. However, his method is derived for waveguides with a low-refractive-index contrast; in a silicon waveguide, the index contrast is high.

In [121] it is shown that Marcatili's dispersion equations are more general and still give a good approximation of the propagation constant for both high and low refractive index contrast cases. However, at large index contrast causes a severe mismatch of the electromagnetic fields inside and outside the core of the waveguide.

The behavior of the TWA depends critically on having exact knowledge of the propa-

gating modes on the top surface of the waveguide where the interaction with electrons in graphene happens. To get a good approximation of the interaction impedance, an improved form of the modal field based on Marcatili's approach is used. This modal electromagnetic field has a lower mismatch for the same dispersion equations.

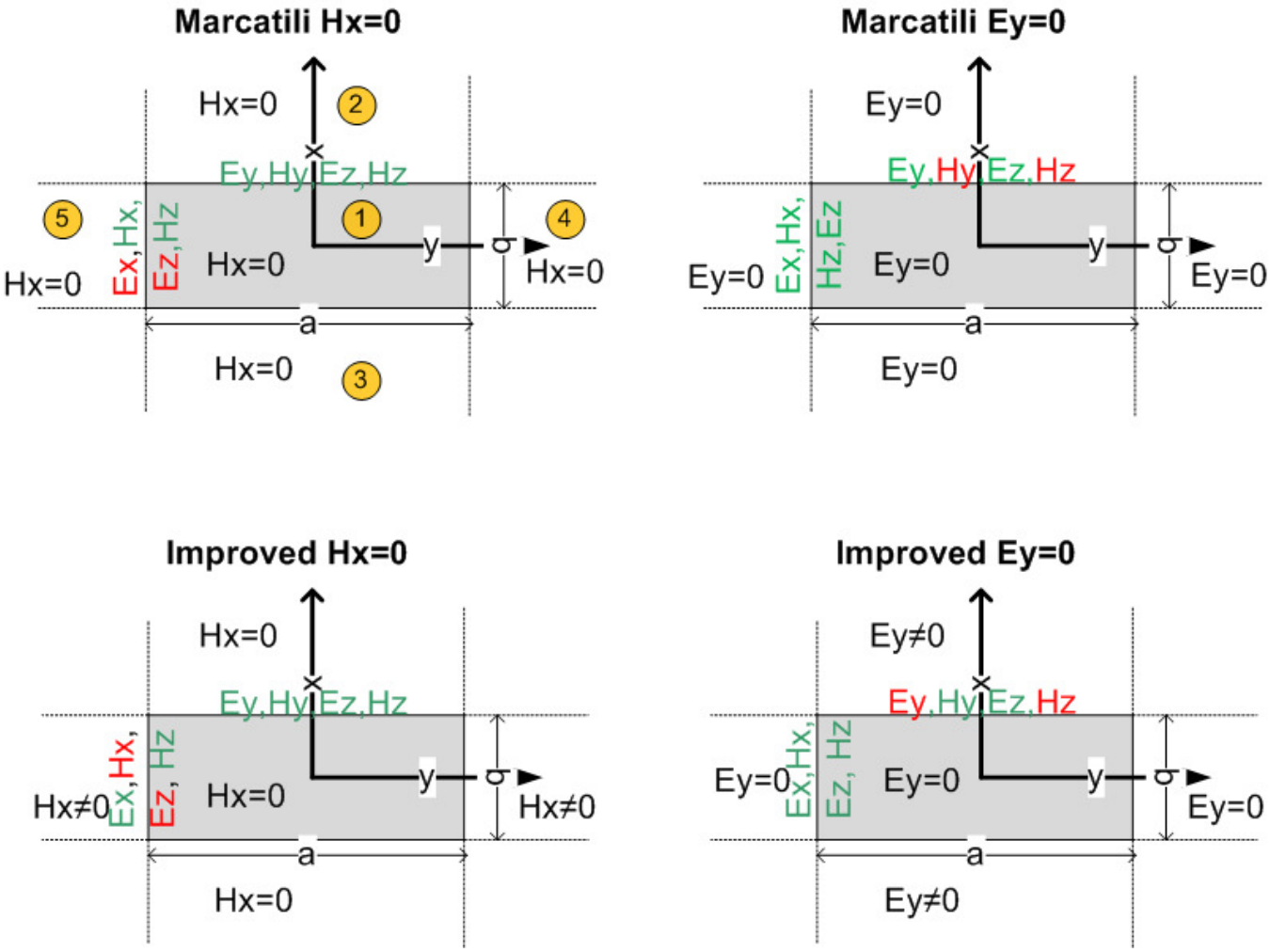

Figure 5.8: Depiction of fulfilled and unfulfilled boundary conditions for Marcatili, and improved Marcatili methods. At each interface, fields that satisfy boundary conditions are shown in green, all others are in red. Regions 1-5 are defined in top left picture.

Detailed descriptions of the Marcatili method and the improved method are given in appendices C and D, respectively. The field distributions obtained from both methods

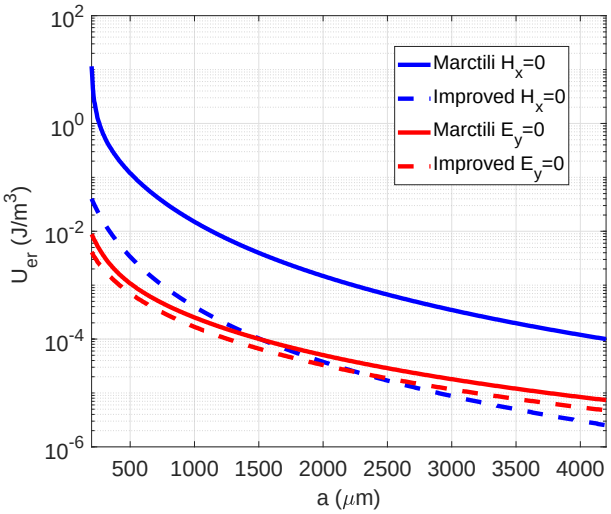

Figure 5.9: Normalized mismatch energy density of Ex_{11} mode at core interfaces, U_{er} (eq. 5.38), for $b = 600\mu m$ at $f = 150GHz$. Comparison of four methods calculating field distribution of Ex_{11} mode.

are not exact solutions of Maxwell's equations. The solutions obey Maxwell's equations in all regions individually. However, all boundary conditions at the interfaces between the waveguide core and its cladding cannot be satisfied at the same time. The difference between these methods is in choosing which boundary conditions to satisfy.

Marcatilis methods (original and improved) are summarized in Fig. 5.8. At each interface, the fields that satisfy the boundary conditions are shown in green, all others are shown in red.

The modes in a rectangular waveguide are divided into two families: Ex_{nm} modes, where most of the electric field is polarized in the x-direction; and Ey_{nm} modes, where most of the electric field is in the y-direction. The subscripts n and m represent, respectively, the number of field extrema along the x and y directions. Our analysis considers only the Ex_{11} mode, a TM-like mode at the top surface of the waveguide where the graphene is located. The coupling between the space charge density wave in the graphene and the TE-like mode (Ey_{nm}) is not significant, since the z-directed plasma wave is modulated only by the z component of the electric field.

Both the improved Hx=0 method and improved Ey=0 method give better estimation of the fields than their corresponding Marcatili method. To demonstrate this, the discon-

tinuities of tangential field components at the interfaces of the waveguide are quantified by defining the parameter U_{er} as [121]:

$$U_{er} = \frac{1}{2l} \oint \epsilon_{avg} |\hat{n} \times (\mathbf{E}^+ - \mathbf{E}^-)|^2 dl + \frac{1}{2l} \oint \mu_0 |\hat{n} \times (\mathbf{H}^+ - \mathbf{H}^-)|^2 dl \tag{5.38}$$

This parameter can be interpreted as a mismatched energy density at the interfaces. The line integral is taken along the circumference of the waveguide's cross section and $l = 2(a+b)$. $\mathbf{E}^+$ ($\mathbf{H}^+$) and $\mathbf{E}^-$ ($\mathbf{H}^-$) are the electric (magnetic) fields just outside and inside the waveguide's core region. $\hat{n}$ is the unit vector orthogonal to the waveguide's surface. Therefore, $\hat{n} \times (\mathbf{E}^+ - \mathbf{E}^-)(\hat{n} \times (\mathbf{H}^+ - \mathbf{H}^-))$ represents the discontinuity of the tangential electric (magnetic) field's vector at the core-cladding interfaces. $\epsilon_{avg} = (\epsilon^+ - \epsilon^-)/2$, where ϵ^+ and ϵ^- are the dielectric constants outside and inside of the waveguide.

The calculated U_{er} curves for the Ex_{11} mode obtained from the methods defined in Fig. 5.8, are plotted together in Fig. 5.9. In this figure, the field amplitudes at each point are normalized such that the total z-directed power propagating in waveguide regions 1-5 (see Fig. 5.8) equals unity.

In Fig. 5.9, the waveguides height is assumed to be constant ($b = 600\mu m$), and the width of the waveguide varies between $a = b/3 = 200\mu m$ and $a = 7b = 4200\mu m$. For the waveguide with a width smaller than $2275\mu m$ ($a \approx 3.8b$) the improved $E_y = 0$ method gives the lowest mismatch error. However, for a TM-like mode in a waveguide wider than $2275\mu m$, the improved $H_x = 0$ gives a lower mismatch than the $E_y = 0$ method. This behavior is expected. A waveguide with a very large value of $b \gg a$ is similar to a slab waveguide with $1-2$ and $1-3$ interfaces. Therefore, the improved $H_x = 0$ method gives better results; in this method all tangential field components are continuous at these interfaces. Similarly, a waveguide with a very large value of $a \gg b$ is similar to a slab waveguide with $1-4$ and $1-5$ interfaces. Therefore, the improved $E_y = 0$ method will give better results.

In the next section, a rectangular waveguide with a grating on top will be analyzed. For the waveguide geometries considered in this thesis, the improved $E_y = 0$ method results in the lowest mismatch and thus provides a better estimation of the electromagnetic field distribution. Therefore, the results of this method will be used in the next section where the field distribution of the fundamental harmonic of the periodic structure is approximated with the field of an unperturbed waveguide to obtain an explicit equation for the interaction impedance.

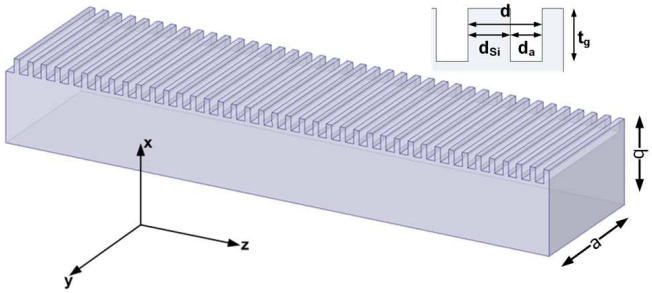

Figure 5.10: High-resistivity silicon waveguide with surface corrugation.

5.3.1 Analysis of Floquet modes in a rectangular dielectric waveguide with a grating on top

This thesis presents an approximate analytical solution for electromagnetic wave propagation in a dielectric rectangular waveguide grating. In the previous section, a similar analysis was done for TE and TM mode propagation in a thin film dielectric waveguide with a grating on the top surface. The current section covers a more-rigorous analysis of hybrid modes in a rectangular dielectric waveguide that is more applicable for monolithic integrated circuits.

The analytic expressions for the space harmonics of the electromagnetic field, and the interaction impedance, are obtained by means of an approximate Floquet mode analysis. In a TWA, the interaction impedance is a measure of the coupling between the electric field and the electron beam in the interaction region for a given electromagnetic power. It is an important parameter in determining the gain and efficiency of the amplifier. The approximate theoretical procedure is well-suited to generating design data for dielectric grating structures. For instance, using this technique in this thesis, the influences of phys- ical dimensions on the interaction impedance are explored. The dimensions of the rectangular waveguide and the grating are determined to obtain the optimum interaction impedance.

The structure under investigation is depicted in Fig. 5.11 The structure is composed of a rectangular high-resistivity silicon waveguide with surface corrugation. Recently, it was demonstrated in [98, 99] that such a waveguide is very low loss at sub-millimeter-wave and THz frequencies. A high precision fabrication process for this structure is also presented.

The electromagnetic waves propagating along a straight waveguide are classified into TE, TM or hybrid modes according to the presence or absence of the longitudinal field components E_z and H_z. The dielectric rectangular waveguide can only support hybrid modes

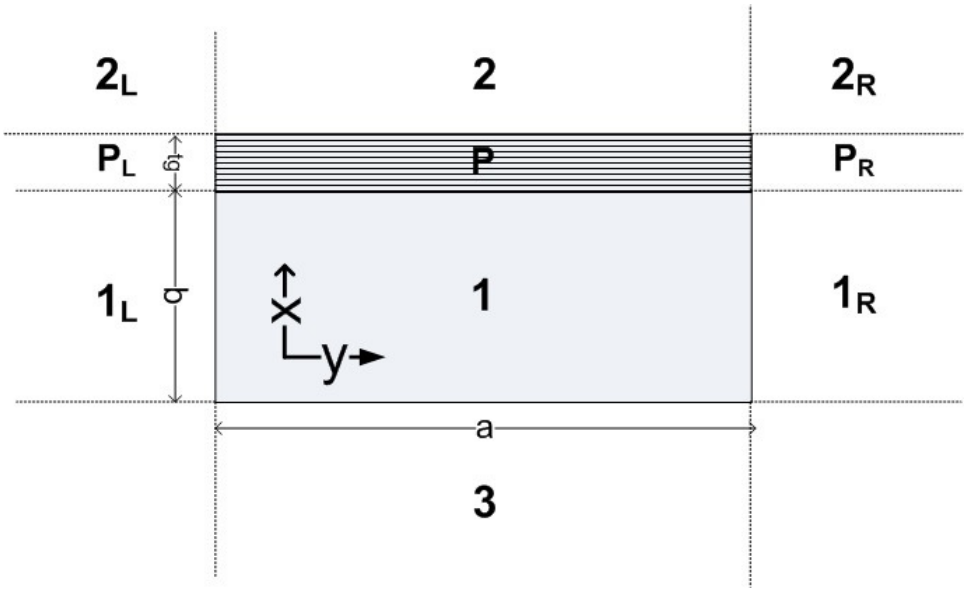

Figure 5.11: Cross section of waveguide with grating layer on top (denoted by "P").

with both E_z and H_z present. Consider a monochromatic wave with angular frequency ω, propagating in the z direction with a propagation constant β_z. In a homogeneous region j, with a relative dielectric constant of $\epsilon_r = \epsilon_{rj} = cons$, all components satisfy the reduced wave equation (here given only for E_z)

$$\nabla_t^2 E_z + K_j^2 E_z = 0 \tag{5.39}$$

where $K_j^2 = k_0^2 \epsilon_{rj} - \beta_z^2$, and ∇_t is the transverse Laplacian.

The grating structure is modelled by a thin inhomogeneous layer of thickness t_g, characterized by the dielectric constant $\epsilon_g(z)$, which varies periodically along the propagation direction z. The wave equations for E_z and H_z in this layer are

$$\nabla^2 E_z + \frac{\partial}{\partial z}\left[\frac{\partial ln(\epsilon_g(z))}{\partial z} E_z\right] + \omega^2 \mu_0 \epsilon_g(z) E_z = 0 \tag{5.40a}$$

$$\nabla^2 H_z + \omega^2 \mu_0 \epsilon_g(z) H_z = 0 \tag{5.40b}$$

Using Maxwell's equations, all electromagnetic field components can be obtained from the longitudinal field components. In the grating region with the $\epsilon_g(z) = \epsilon_0 \epsilon_{rg}(z)$ function of

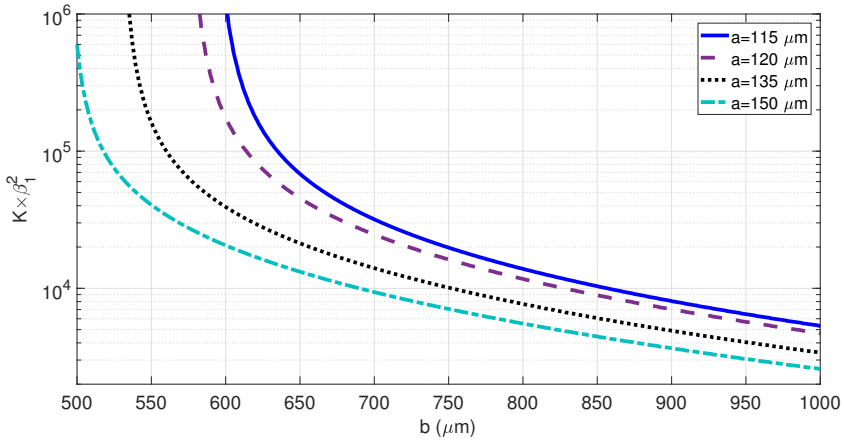

Figure 5.12: Coupling factor as a function of b for different values of a with $l_p = 300nm$, $t_g = 300nm$ and $m_d = 0.3$ at $f = 150GHz$.

z, we have

$$k_0^2\epsilon_{rg}(z)E_x + \frac{\partial^2 E_x}{\partial z^2} = \frac{\partial^2 E_z}{\partial z \partial x} - j\omega\mu\frac{\partial H_z}{\partial y} \tag{5.41a}$$

$$k_0^2\epsilon_{rg}(z)E_y + \frac{\partial^2 E_y}{\partial z^2} = \frac{\partial^2 E_z}{\partial z \partial y} + j\omega\mu\frac{\partial H_z}{\partial y} \tag{5.41b}$$

$$k_0^2\epsilon_{rg}(z)H_x - \frac{\partial \ln\epsilon_g(z)}{\partial z}\frac{\partial H_x}{\partial z} + \frac{\partial^2 H_x}{\partial z^2} = j\omega\epsilon_g\frac{\partial E_z}{\partial y} + \frac{\partial^2 H_z}{\partial z \partial x} - \frac{\partial \ln\epsilon_g(z)}{\partial z}\frac{\partial H_z}{\partial x} \tag{5.41c}$$

$$k_0^2\epsilon_{rg}(z)H_y - \frac{\partial \ln\epsilon_g(z)}{\partial z}\frac{\partial H_y}{\partial z} + \frac{\partial^2 H_y}{\partial z^2} = j\omega\epsilon_g\frac{\partial E_z}{\partial y} + \frac{\partial^2 H_z}{\partial z \partial x} - \frac{\partial \ln\epsilon_g(z)}{\partial z}\frac{\partial H_z}{\partial x} \tag{5.41d}$$

In a homogeneous region, the above equations (5.40,5.41) are simplified by substituting $\partial \ln\epsilon_g(z)/\partial z$ equal to zero.

In a rectangular dielectric waveguide with a periodic dielectric layer, the field compo-

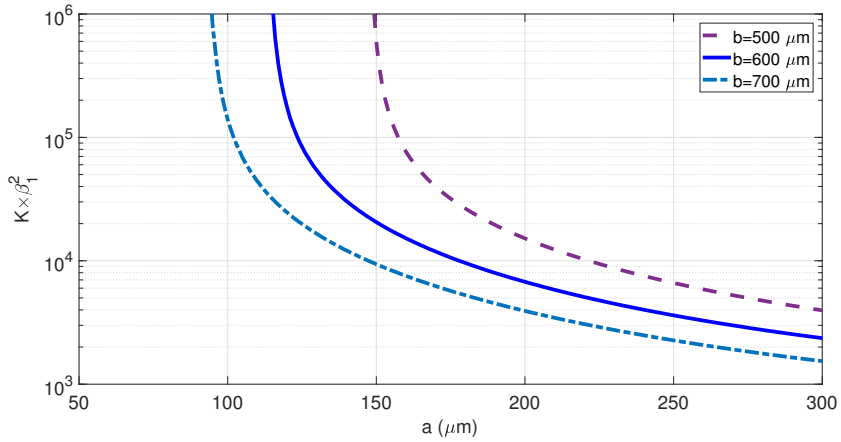

Figure 5.13: Coupling factor as a function of a for different values of b with $l_p = 300nm$, $t_g = 300nm$ and $m_d = 0.3$ at $f = 150GHz$.

nents are in the Floquet form:

$$H_z = \sum_{-\infty}^{\infty} h_{zm}(x,y)e^{-j\beta_{zm}z} \tag{5.42a}$$

$$E_z = \sum_{-\infty}^{\infty} e_{zm}(x,y)e^{-j\beta_{zm}z} \tag{5.42b}$$

where $\beta_{zm} = \beta_{z0} + \frac{2m\pi}{d}$. Similar equations are applied for the x and y field components.

The relative dielectric constant of the grating layer with periodic dielectric constant, $\epsilon_g = \epsilon_0\epsilon_{rg}$, can be expressed by its Fourier series expansion

$$\epsilon_{rg} = \epsilon_{rg0} + \sum_{1}^{\infty} \epsilon_{rgm}\cos(\frac{2\pi m}{d}z) \tag{5.43}$$

Substituting the Floquet expansion of the field components (5.42), along with the first-order Fourier expansion of $\epsilon_{rg} = \epsilon_{rg0} + \epsilon_{rg1}\cos(\frac{2\pi}{d}z)$ and $\frac{\partial \ln(\epsilon_{rg})}{\partial z} = g_1\sin(\frac{2\pi}{d}z)$ into equation

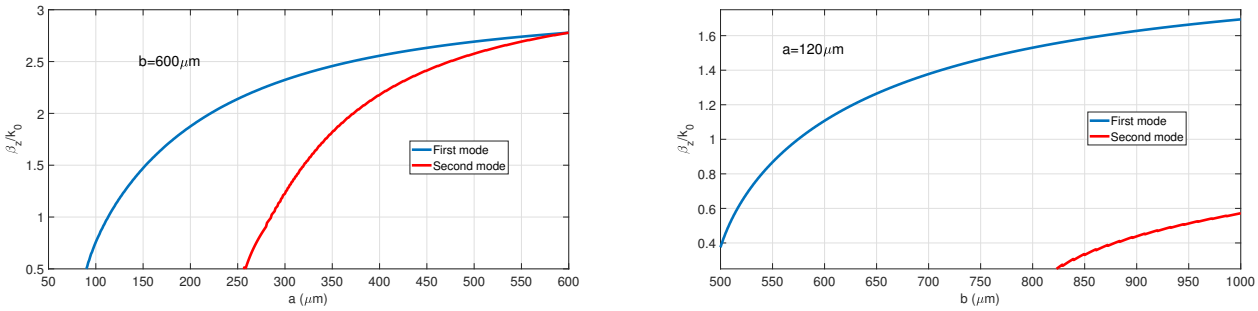

Figure 5.14: (a) Normalized dispersion diagram of uniform rectangular silicon waveguide versus a with $b = 600\mu$m. (b) Normalized dispersion diagram versus b with $a = 120\mu$m.

(5.40) and (5.41) yields

$$\sum_m \left(\nabla_t^2 - \beta_{zm}^2 + k_0^2\epsilon_{rg0}\right) h_{zm}(x,y)e^{-j\beta_{zm}z} + k_0^2\epsilon_{rg1}/2\left[\sum_m h_{zm}e^{-j\beta_{z(m-1)}z} + \sum_m h_{zm}e^{-j\beta_{z(m+1)}z}\right] = 0 \tag{5.44}$$

$$\begin{aligned}&\sum_m \left(\nabla_t^2 - \beta_{zm}^2 + k_0^2\epsilon_{rg0}\right) e_{zm}e^{-j\beta_{zm}z} + \\ &\sum_m \left(k_0^2\epsilon_{rg1}/2 + g_1\pi/d - \beta_{zm}g_1/2\right) e_{zm}e^{-j\beta_{z(m-1)}z} + \\ &\sum_m \left(k_0^2\epsilon_{rg1}/2 + g_1\pi/d + \beta_{zm}g_1/2\right) e_{zm}e^{-j\beta_{z(m+1)}z} = 0\end{aligned} \tag{5.45}$$

$$\begin{aligned}&\sum_m \left(k_0^2\epsilon_{rg0} - \beta_{zm}^2\right) e_{ym}e^{-j\beta_{zm}z} + \sum_m \frac{k_0^2\epsilon_{rg1}}{2}e_{ym}e^{-j\beta_{z(m-1)}z} + \sum_m \frac{k_0^2\epsilon_{rg1}}{2}e_{y(m)}e^{-j\beta_{z(m+1)}z} \\ &= -\sum_m j\beta_{zm}\frac{\partial e_{zm}}{\partial y}e^{-j\beta_{zm}z} + \sum_m j\omega\mu_0\frac{\partial h_{zm}}{\partial x}e^{-j\beta_{zm}z}\end{aligned} \tag{5.46}$$

$$
\begin{aligned}
&\sum_m \left(k_0^2\epsilon_{rg0} - \beta_{zm}^2\right) h_{ym} e^{-j\beta_{zm}z} + \\
&\sum_m \left(\frac{k_0^2\epsilon_{rg1}}{2} + \frac{g_1\beta_{zm}}{2}\right) h_{ym} e^{-j\beta_{z(m-1)}z} + \sum_m \left(\frac{k_0^2\epsilon_{rg1}}{2} - \frac{g_1\beta_{zm}}{2}\right) h_{ym} e^{-j\beta_{z(m+1)}z} \\
&= -\sum_m j\beta_{zm}\frac{\partial h_{zm}}{\partial y} e^{-j\beta_{zm}z} - \frac{g_1}{2j}\left[\sum_m \frac{\partial h_{zm}}{\partial y} e^{-j\beta_{z(m-1)}z} - \sum_m \frac{\partial h_{zm}}{\partial y} e^{-j\beta_{z(m+1)}z}\right] \\
&- \sum_m j\omega\epsilon_0\epsilon_{rg0}\frac{\partial e_{zm}}{\partial x} e^{-j\beta_{zm}z} - j\omega\epsilon_0\frac{\epsilon_{rg1}}{2}\left[\sum_m \frac{\partial e_{zm}}{\partial x} e^{-j\beta_{z(m-1)}z} + \sum_m \frac{\partial e_{zm}}{\partial x} e^{-j\beta_{z(m+1)}z}\right]
\end{aligned}
\tag{5.47}
$$

Due to the uniqueness of the Fourier series expansion, we have:

$$
\nabla_t^2 h_{zm} - G_{pm}^2 h_{zm} = -k_0^2\frac{\epsilon_{rg1}}{2}\left(h_{z(m-1)} + h_{z(m+1)}\right) \tag{5.48}
$$

$$
\begin{aligned}
\nabla_t^2 e_{zm} - G_{pm}^2 e_{zm} = &-\left[\frac{k_0^2\epsilon_{rg1}}{2} + \frac{g_1\beta_{z(m-1)}}{2} + \frac{g_1\pi}{d}\right] e_{z(m-1)} \\
&-\left[\frac{k_0^2\epsilon_{rg1}}{2} - \frac{g_1\beta_{z(m-1)}}{2} + \frac{g_1\pi}{d}\right] e_{z(m+1)}
\end{aligned}
\tag{5.49}
$$

$$
e_{ym} = \frac{k_0^2\epsilon_{rg1}}{2G_{pm}^2}\left(e_{y(m-1)} + e_{y(m+1)}\right) + \frac{j\beta_{zm}}{G_{pm}^2}\frac{\partial e_{zm}}{\partial y} - \frac{j\omega\mu_0}{G_{pm}^2}\frac{\partial h_{zm}}{\partial x} \tag{5.50}
$$

$$
\begin{aligned}
h_{ym} = &\frac{k_0^2\epsilon_{rg1}}{2G_{pm}^2}\left(h_{y(m-1)} + h_{y(m+1)}\right) \\
&\frac{g_1}{2G_{pm}^2}\left(\beta_{z(m+1)}h_{y(m+1)} - \beta_{z(m-1)}h_{y(m-1)}\right) \\
&-\frac{j\beta_{zm}}{G_{pm}^2}\frac{\partial h_{zm}}{\partial y} - \frac{jg_1}{2G_{pm}^2}\left(\frac{\partial h_{z(m-1)}}{\partial y} - \frac{\partial h_{z(m+1)}}{\partial y}\right) \\
&-\frac{j\omega\epsilon_0\epsilon_{rg0}}{G_{pm}^2}\frac{\partial e_{zm}}{\partial x} - \frac{j\omega\epsilon_0\epsilon_{rg1}}{2G_{pm}^2}\left(\frac{\partial e_{z(m-1)}}{\partial x} + \frac{\partial e_{z(m+1)}}{\partial x}\right)
\end{aligned}
\tag{5.51}
$$

where $G_{pm}^2 = \beta_{zm}^2 - \omega^2\mu_0\epsilon_0\epsilon_{rg0}$. This set of equations couples each space harmonic to the next lower and higher harmonics. If higher order Fourier terms of ϵ_{rg} (5.43) are considered, more harmonic terms will appear. The higher-order space harmonics have amplitudes much smaller than those of the lower-order space harmonics. Therefore, the first-order approximation is applied to simplify the above equations. In this approximation, to obtain the solution for the first-order space harmonic (m=1), the second-order space harmonic (m=2) is neglected with respect to the zeroth-order space harmonic.

$$\nabla_t^2 h_{z1} - G_{p1}^2 h_{z1} = -k_0^2 \frac{\epsilon_{rg1}}{2} h_{z0} \tag{5.52}$$

$$\nabla_t^2 e_{z1} - G_{p1}^2 e_{z1} = -\left[\frac{k_0^2\epsilon_{rg1}}{2} + \frac{g_1\beta_{z0}}{2} + \frac{g_1\pi}{d}\right] e_{z0} \tag{5.53}$$

$$e_{y1} = \frac{j\beta_{z1}}{G_{p1}^2}\frac{\partial e_{z1}}{\partial y} - \frac{j\omega\mu_0}{G_{p1}^2}\frac{\partial h_{z1}}{\partial x} + \frac{k_0^2\epsilon_{rg1}}{2G_{p1}^2} e_{y0} \tag{5.54}$$

$$\begin{aligned} h_{y1} = &-\frac{j\beta_{z1}}{G_{p1}^2}\frac{\partial h_{z1}}{\partial y} - \frac{j\omega\epsilon_0\epsilon_{rg0}}{G_{p1}^2}\frac{\partial e_{z1}}{\partial x} \\ &- \frac{jg_1}{2G_{p1}^2}\frac{\partial h_{z0}}{\partial y} - \frac{j\omega\epsilon_0\epsilon_{rg1}}{2G_{p1}^2}\frac{\partial e_{z0}}{\partial x} + \frac{k_0^2\epsilon_{rg1} - g_1\beta_{z0}}{2G_{p1}^2} h_{y0} \end{aligned} \tag{5.55}$$

For a waveguide with a thin grating, the zeroth-order space harmonic can be approximated by the modal solution of the rectangular waveguide with no grating. As was mentioned in the introduction, there is no analytic solution for the field distribution of a rectangular dielectric waveguide. Therefore, the field distributions obtained from the improved Marcatili $E_y = 0$ method (described in appendix D), are used as a good approximation for the field distribution of the zeroth-order space harmonic.

$$e_{z0} = A_2 e^{-\gamma_x(x-b/2)}\cos(k_y y) \tag{5.56a}$$

$$h_{z0} = B_2 e^{-\gamma_x(x-b/2)}\sin(k_y y) \tag{5.56b}$$

$$e_{y0} = \left(A_2\frac{j\beta_{z0}k_y}{k_{t_2}^2} - B_2\frac{j\omega\mu\gamma_x}{k_{t_2}^2}\right) e^{-\gamma_x(x-b/2)}\sin(k_y y) \tag{5.56c}$$

$$h_{y0} = \left(A_2\frac{j\omega\epsilon_0\epsilon_{r2}\gamma_x}{k_{t_2}^2} - B_2\frac{j\beta k_y}{k_{t_2}^2}\right) e^{-\gamma_x(x-b/2)}\cos(k_y y) \tag{5.56d}$$

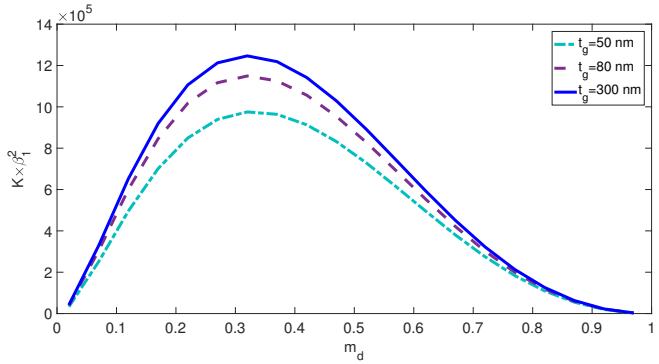

(a)

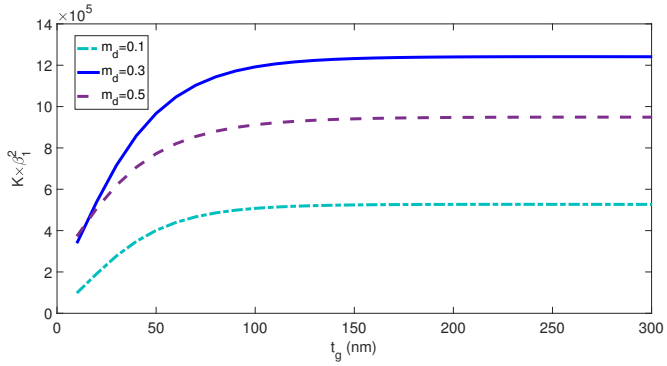

(b)

Figure 5.15: (a) Coupling factor versus m_d for different values of t_g; and (b) interaction impedance versus t_g for different values of m_d with $a = 115\mu m$, $b = 600\mu m$ at $f = 150GHz$

where A_2 and B_2 coefficients are defined by eq.D.1.

5.3.2 Derivation of the field distribution of the first-order space harmonic

Because the first order space harmonic field is confined mainly to the grating layer, its field distribution can be defined only for the grating layer and surrounding areas, assuming the field distribution to be negligible in other areas. Figure 5.11 shows a cross section of the rectangular waveguide with a thin grating layer on top denoted by the letter "P". The field

of the first-order harmonic inside regions 1, 2, and P, is a standing wave in y direction, and it decays in proportion to its distance from the interfaces of the P layer in the x direction. For a thick rectangular waveguide, it can be assumed that the field decays completely in silicon layer 1; thus, no field of the first order harmonic reaches layer 3 under the silicon layer.

Since most of the first order space harmonic's power is concentrated in layer P (as in Marcatili's approach), the field at the corner areas $1_{L,R}$ and $2_{L,R}$ can be neglected. Furthermore, in regions P_R and p_L, the field decays in y direction from the interfaces of the grating layer. Thus, for a thin layer of grating when its thickness, t_g, is much smaller than its width, a, the field in regions p_L and p_R can also be neglected. The analysis of a 2D slab structure presented in the previous section, showed that although the interaction impedance is higher for thicker grating layers, it does not change for gratings thicker than $t_g = d$, where d is the pitch of the grating (Fig. 5.3). Therefore, the assumption $t_g << a$ can be applied for the structure in question in which t is in the order of a few hundred nanometers and a is in the order of tens of micrometers.

By considering all of the above-mentioned assumptions, the $H_{z1} = h_{z1}e^{-j\beta_{z1}z}$ and $E_{z1} = e_{z1}e^{-j\beta_{z1}z}$ field components of the first-order space harmonic can be represented as:

$$e_{z1} = \begin{cases} a_2 e^{-\gamma_{x2}(x-b/2-t_g)}\cos(k_y y) & x > b/2 + t_g \\ \left[a_p \sinh(\gamma_{xp}(x-b/2)) + a'_p \cosh(\gamma_{xp}(x-b/2)) \right. & \\ \qquad \left. -A_2 \dfrac{f' e^{-\gamma_x(x-b/2)}}{\gamma_x^2 - k_y^2 - G_{p1}^2}\right]\cos(k_y y) & b/2 < x < b/2 + t_g \\ a_1 e^{\gamma_{x1}(x-b/2)}\cos(k_y y) & x < b/2 \end{cases} \tag{5.57}$$

$$h_{z1} = \begin{cases} b_2 e^{-\gamma_{x2}(x-b/2-t_g)}\sin(k_y y) & x > b/2 + t_g \\ \left[b_p \cosh(\gamma_{xp}(x-b/2)) + b'_p \sinh(\gamma_{xp}(x-b/2)) - B_2 \dfrac{f e^{-\gamma_x(x-b/2)}}{\gamma_x^2 - k_y^2 - G_{p1}^2}\right] & \\ \quad \sin(k_y y) & b/2 < x < b/2 + t_g \\ b_1 e^{\gamma_{x1}(x-b/2)}\sin(k_y y) & x < b/2 \end{cases} \tag{5.58}$$

where $f = \frac{k_0^2 \epsilon_{r2}}{2}$ and $f' = \frac{k_0^2 \epsilon_{r2}}{2} + \frac{g_1 \beta_{z0}}{2} + \frac{g_1 \pi}{d}$. From the wave equations in 3 regions we have:

$$\gamma_{x1}^2 = \beta_{z1}^2 + k_y^2 - k_0^2 \epsilon_{air} \tag{5.59a}$$
$$\gamma_{x2}^2 = \beta_{z1}^2 + k_y^2 - k_0^2 \epsilon_{Si} \tag{5.59b}$$
$$\gamma_{xp}^2 = \beta_{z1}^2 + k_y^2 - k_0^2 \epsilon_{rg0}. \tag{5.59c}$$

Since both the zeroth- and first-order harmonics are hybrids, both E_z and H_z components should be defined to obtain all other field components (Eq. 5.41). The e_{z1} and h_{z1} fields defined by equations 5.57 and 5.58, satisfy wave equations C.2 in homogeneous layers 1 and 2, and satisfy the equations 5.53 and 5.52 for the periodic layer "p". These are inhomogeneous electromagnetic wave equations with $ez0$ and $hz0$ given in eq. 5.56.

Similarly, the e_{y1} and h_{y1} components are obtained from equations 5.54 and 5.3.1

$$e_{y1} = \begin{cases} \left[-a_2 \dfrac{j\beta_{z1} k_y}{G_{t2}^2} + b_2 \dfrac{j\omega\mu_0 \gamma_{x2}}{G_{t2}^2} \right] e^{-\gamma_{x2}(x - b/2 - t_g)} \sin(k_y y) & x > b/2 + t_g \\ e_{y1}^g & b/2 < x < b/2 + t_g \\ \left[-a_1 \dfrac{j\beta_{z1} k_y}{G_{t1}^2} - b_1 \dfrac{j\omega\mu_0 \gamma_{x1}}{G_{t1}^2} \right] e^{\gamma_{x1}(x - b/2)} \sin(k_y y) & x < b/2 \end{cases} \tag{5.60}$$

$$\begin{aligned} e_{y1}^g = & -\frac{j\beta_{z1} k_y}{G_{p1}^2} \left[a_p \sinh(\gamma_{xp}(x - b/2)) + a_p' \cosh(\gamma_{xp}(x - b/2)) - \frac{f' A_2}{\gamma_x^2 - k_y^2 - G_{p1}^2} e^{-\gamma_x (x - b/2)} \right] \sin(k_y y) \\ & - \frac{j\omega\mu_o}{G_{p1}^2} \left[\gamma_{xp} \left(b_p \cosh(\gamma_{xp}(x - b/2)) + b_p' \sinh(\gamma_{xp}(x - b/2)) \right) + \frac{f B_2}{\gamma_x^2 - k_y^2 - G_{p1}^2} \gamma_x e^{-\gamma_x (x - b/2)} \right] \sin(k_y y) \\ & + \frac{k_0^2 \epsilon_{rg1}}{2 G_{p1}^2} \left(A_2 \frac{j\beta_{z0} k_y}{k_{t2}^2} - B_2 \frac{j\omega\mu_0 \gamma_x}{k_{t2}^2} \right) e^{-\gamma_x (x - b/2)} \sin(k_y y) \end{aligned} \tag{5.61}$$

$$h_{y1} = \begin{cases} \left(-a_2 \dfrac{j\omega\epsilon_0\epsilon_{r2}\gamma_{x2}}{G_{t2}^2} + b_2 \dfrac{j\beta_{z1}k_y}{G_{t2}^2}\right) e^{-\gamma_{x2}(x-b/2-t_g)} \cos(k_y y) & x > b/2 + t_g \\ h_{y1}^g & b/2 < x < b/2 + t_g \\ \left(a_1 \dfrac{j\omega\epsilon_0\epsilon_{r1}\gamma_{x1}}{G_{t1}^2} + b_1 \dfrac{j\beta_{z1}k_y}{G_{t1}^2}\right) e^{\gamma_{x1}(x-b/2)} \cos(k_y y) & x < b/2 \end{cases} \tag{5.62}$$

$$\begin{aligned} h_{y1}^g =& \frac{j\omega\epsilon_0\epsilon_{rg0}}{G_{p1}^2} \left[\gamma_{xp}[a_p \cosh(\gamma_{xp}(x-b/2)) + a_p' \sinh(\gamma_{xp}(x-b/2))] + \gamma_x \frac{f' A_2}{\gamma_x^2 - k_y^2 - G_{p1}^2} e^{-\gamma_x(x-b/2)}\right] \cos(k_y y) \\ &+ \frac{j\beta_{z1}k_y}{G_{p1}^2} \left[b_p \cosh(\gamma_{xp}(x-b/2)) + b_p' \sinh(\gamma_{xp}(x-b/2)) - \frac{f B_2}{\gamma_x^2 - k_y^2 - G_{p1}^2} e^{-\gamma_x(x-b/2)}\right] \cos(k_y y) \\ &+ \frac{k_0^2\epsilon_{rg1} - g_1\beta_{z0}}{2G_{p1}^2} \left(A_2 \frac{j\omega\epsilon_0\epsilon_{r2}\gamma_x}{k_{t2}^2} - B_2 \frac{j\beta_{z0}k_y}{k_{t2}^2}\right) e^{-\gamma_x(x-b/2)} \cos(k_y y) \\ &+ \left(-A_2 \frac{j\omega\epsilon_0\epsilon_{rg1}\gamma_x}{2G_{p1}^2} + B_2 \frac{j g_1 k_y}{2G_{p1}^2}\right) e^{-\gamma_x(x-b/2)} \cos(k_y y) \end{aligned} \tag{5.63}$$

where $G_{t1}^2 = B_{z1}^2 - k_0^2\epsilon_{Si}$ and $G_{t2}^2 = B_{z1}^2 - k_0^2\epsilon_{air}$. The eight unknown coefficients ($a_{1,2,p}$, $b_{1,2,p}$, a_p', and b_p' coefficients in equations5.57 and 5.58) are obtained from the boundary conditions. Since the field is considered non-negligible only in regions 1, 2, and p, the boundary conditions are the continuity of E_z, H_z, E_y and H_y components at the top and bottom grating layer interfaces, resulting in 8 equations. By solving these 8 equations with 8 unknowns, the field distribution coefficients are obtained.

The next step is to use the field distribution of the first-order space harmonic mode defined in this section to obtain the interaction impedance of the proposed TWA described in the beginning of this chapter (Fig. 5.1)

5.3.3 Gain and dispersion equations

Similar to the discussion focused on slab waveguides (section 5.2.2), the field of the space harmonic excited by the surface current of $\mathbf{J} = \mathbf{J_e} e^{-j\beta z}$ can be obtained for the top-grated rectangular waveguide from eq. 5.5, substituting $\mathbf{E_{A_1}} = A_s \cos(k_y y)\hat{z}$ and $\mathbf{J_e} = J_s \cos(k_y y)\hat{z}$

$$\mathbf{E_1}(x_g, y) = \frac{-j|A_s|^2\,(a + \sin(k_y a)/k_y)}{8P_{A0}(\beta_1 - \beta)} J_s \cos(k_y y) \tag{5.64}$$

where $A_s = a_p \sinh(\gamma_{xp} t_g) + a'_p \cosh(\gamma_{xp} t_g) - A_2 \frac{f' e^{-\gamma_x t_g}}{\gamma_x^2 - k_y^2 - G_{p1}^2}$ (eq. 5.53). P_{A_0} is calculated by integrating the z component of the Poynting vector $\mathbf{P} = \frac{1}{2}\mathbf{E} \times \mathbf{H}^*$ over the areas of all $1-5$ regions using the field expressions given by equations C.3 and C.4.

The current induced by this electric field at the surface of the graphene is obtained from Ohm's law (eq. 5.34). The dispersion equation is obtained by imposing a self-consistency condition between equations 5.64 and 5.34:

$$\frac{-j|A_s|^2\,(a + \sin(k_y a)/k_y)}{8P_{A0}(\beta_{z1} - \beta_z)} \sigma(\beta_z, \omega) = 1 \tag{5.65}$$

This equation is similar to equation 5.35 given for the slab waveguide, except that in the former, the term $|E_{A1}(x = x_g, y = 0)|^2\,(1/2 + cos(k_y a))$ replaces the term $|E_{A1}(x = x_g)|$ in order to consider the variation of the electric field along the y axis. Also, the P_{A0} in this equation is the total power carried by the first harmonic of the electric field. Similar to eq. 5.37 the gain equals $g = 2Im\beta = K_1\beta_1^2 Real(\sigma)$. For the rectangular structure, the interaction impedance K_1 is defined as:

$$K_1 = \frac{|A_s|^2\,(a + \sin(k_y a)/k_y)}{4P_{A0}\beta_{z1}^2} \tag{5.66}$$

The amount of $K_1\beta_1^2$ determines the strength of the coupling between the electromagnetic wave propagating in the rectangular waveguide and the space charge wave confined to the graphene layer. The value of $K_1\beta_1^2$ depends on both the waveguide dimensions, a and b, and the grating dimensions, l_p, t_g and f_d. These parameters should be optimized to maximize the coupling factor.

Figure 5.12 and 5.13 show the value of $K_1\beta_1^2$ as a function of b and a for different a and b values respectively, at the frequency of $150GHz$ with $l_p = 300nm$, $t_g = 300nm$ and $m_d = 0.3$. These figures show that the maximum coupling is obtained when the propagation constant of the waveguide is close to the cutoff point. Figure 5.14(a) and (b) show the dispersion plot of the uniform (without grating) rectangular waveguide versus a (with $b = 600\mu m$) and b (with $a = 120\mu m$), respectively. These plots are obtained by solving equations C.7d and C.8d, given $\beta_0^2 = k_0^2 - k_x^2 - k_y^2$. Near the cutoff point, the field of the rectangular waveguide is less confined to the core and therefore has more overlap with the plasma wave at the graphene's surface. The result is a larger coupling factor.

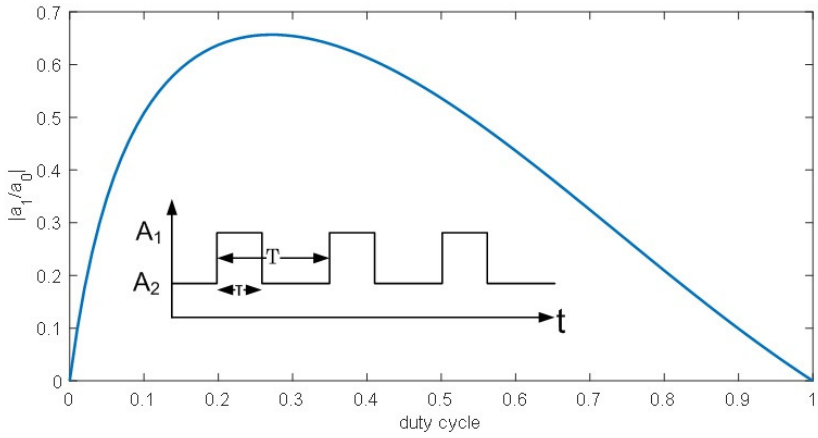

Figure 5.16: Normalized amplitude of second Fourier series coefficient $\left|\frac{a_1}{a_0}\right|$ for rectangular wavefrom, depicted in the inset, with $A_1 = 1$ and $A_2 = 1/\epsilon_{Si}$.

Figure 5.15(a) and (b) shows the variation of $K_1\beta_1^2$ with respect to the filling factor and depth of the grating, respectively, with $l_p = 300nm$, $a = 115\mu m$ and $b = 600\mu m$ at $f = 150GHz$. The first-order space harmonic field at the surface of the grating is roughly similar to a periodic rectangular waveform. The Fourier series representation of a rectangular waveform with the maximum of A_1, minimum of A_2, period of T, and duty cycle of $D = \frac{\tau}{T}$ (see inset of Fig. 5.16) is:

$$S_{\Pi}(t) = \sum_{n=-\inf}^{+\infty} a_n e^{-j\frac{2\pi n}{T}t} \tag{5.67}$$

$$a_0 = A_2 + D(A_1 - A_2), \quad a_n = \frac{(A_1 - A_2)}{j2\pi n}\left(e^{j2\pi Dn} - 1\right) \tag{5.68}$$

The ratio of $\left|\frac{a_1}{a_0}\right|$ versus D for $A_1 = 1$ and $A_2 = 1/\epsilon_{Si}$ is plotted in Fig. 5.16. This plot is very similar to the plot depicted in Fig. 5.15(a).

The plots of Fig. 5.12, 5.12 and 5.15 are used to design the rectangular waveguide and the grating for the slow-wave structure of the TWA. The goal is to gain maximum interaction impedance. The rectangular image waveguide is used instead of a rectangular rod waveguide. The image waveguide has the same thickness as the wafer being used. From among standard wafer thicknesses, 300μm was chosen; a thickness suitable for the frequency band of $\sim 100GHz$ to $300GHz$. The image waveguide structure is supported by

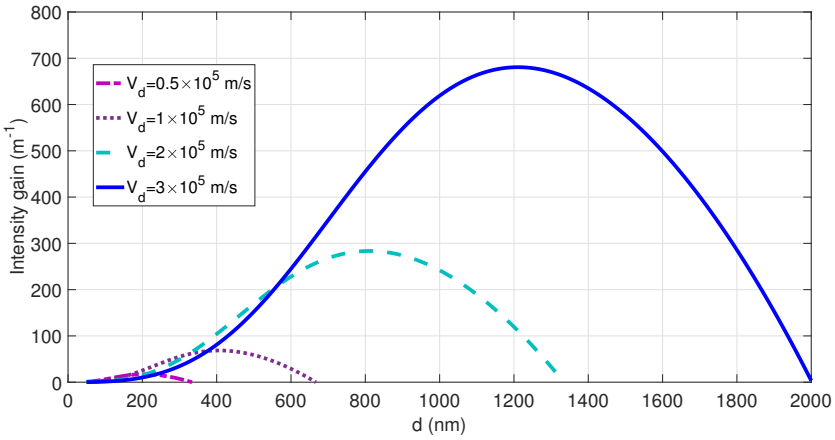

Figure 5.17: Gain versus period of grating for different values of drift velocity given $b = 600\mu m$, $a = 120\mu m$, $m_d = 0.3$, $t_g = d$, and $E_f = 0.3$ eV.

a metallic ground. Therefore, for TM modes, it is roughly equivalent to a rod waveguide twice as thick as the image waveguide. Thus, the b dimension in Fig. 5.12 and 5.13, is fixed to 600μm, and the waveguide width, a, is the only design parameter used when optimizing the interaction impedance. The values of $b = 600\mu$m, $a = 120\mu$m, $m_d = 0.3$, and $tg \geqslant d$ are chosen to obtain the maximum impedance.

By substituting (4.14) and (5.66) into $g = K_1\beta_1^2 Real(\sigma))$, the power gain is found for different values of drift velocity. The intensity gain in Fig. 5.17 is plotted for drift velocities from $V_d = 0.5 \times 10^5$ m/s to $V_d = 3 \times 10^5$ m/s. The maximum graphene drift velocity reported in the literature varies from 2×10^5 m/s to 5.4×10^5 m/s [107] [108] [109]. For very small values of period, d, the phase velocity can be approximated by $V_{ph} \simeq fd$. The values of d at which the maximum gain is obtained increase with the drift velocity (Fig. 5.17). For example, for $V_d = 3 \times 10^5$ m/s, the maximum gain is obtained at $d = 680$ nm.

Figure 5.18 shows the power gain versus the frequency for the optimized waveguide dimensions. In this figure, the Fermi energy and drift velocity of the graphene are respectively $V_d = 3 \times 10^5$m/s and $E_f = 0.3$ eV. The maximum power gain is $g = 14.45$ dB/cm.

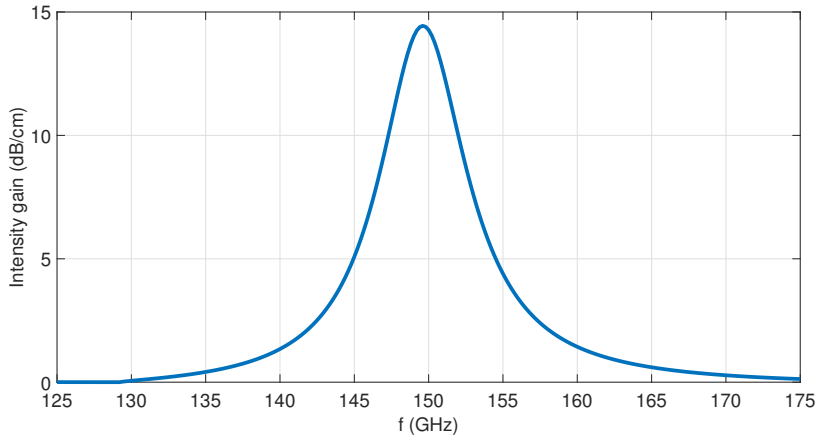

Figure 5.18: Gain verus frequency for $b = 600\mu m$, $a = 120\mu m$, $m_d = 0.3$, $d = t_g = 680nm$, $V_d = 3 \times 10^5$ m/s and $E_f = 0.3$ eV.

5.3.4 Verifying the proposed method using numerical simulation

To verify the proposed approximation method, rectangular waveguides with grating on top were simulated by a finite-element-based software from ANSYS electronics. The grating periods for the proposed TWA at $f = 150$ GHz should be in the range of a few 100 nms. Simulating these gratings requires a very fine mesh; for example, the grating period of 200 nm is 10000 times smaller than the free space wavelength. Therefore, due to the lack of system memory, gratings with a much larger period of 20μm were simulated. Some of the assumptions (e.g., confinement of the first order space harmonic field to the surface of the grating), are less accurate for a larger period of gratings. However, there are still enough similarities between the results of the two methods to show that the proposed approximation method has enough accuracy to be used to design a structure and achieve nearly optimum gain. However, it may not be accurate enough to give the exact value of specific parameters such as the interaction impedance and gain.

The simulated structure is depicted in Fig. 5.19 To obtain highly accurate results, a very fine mesh is defined inside the grating layer, and to save memory space, coarser mesh is defined inside the rectangular waveguide. The generated mesh is shown in the inset of Fig. 5.19. To extract the interaction impedance from the simulation results, the simulated fields were transferred to a MATLAB file. Then, the discrete Fourier transform of the field was computed using the fast Fourier transform algorithm in MATLAB.

The magnitude of the electric field inside the waveguide and around it is plotted in Fig.

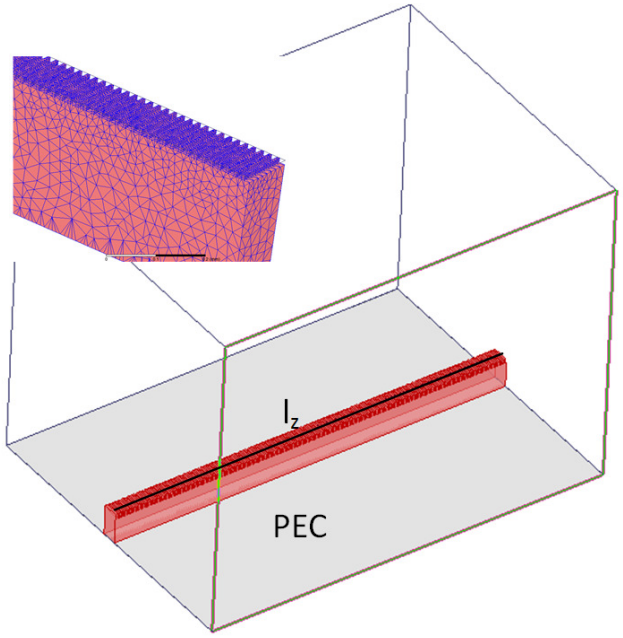

Figure 5.19: Simulated silicon image waveguide. Inset shows generated mesh.

5.20. Figure 5.21 shows the Ez component of the electric field in the middle of the surface of the grating along the z-direction (line l_z in Fig. 5.19). It consists of rapid fluctuations with a slowly varying sinusoidal envelope. The slow varying sinusoidal envelope is the fundamental harmonic, while the rapid fluctuations are caused by first and higher order harmonics. To obtain the exact amplitude of each harmonic, the Fourier transform of the field distribution along the z direction is calculated (see Fig. 5.22). The k_y parameter in (5.66) is obtained by fitting a cosine, $cos(k_y y)$ function to the field distribution of the field along the y direction inside the rectangular waveguide (see Fig. 5.23). The propagated power P is the same as the source power defined by the input port.

In Fig. 5.24, the coupling factor versus b obtained from the approximate analysis is plotted together with that obtained from the simulations. The guided modes in an infinite dielectric slab waveguide have propagation constants greater than k_0. The propagation constant depends on the slab thickness. The thickness at which the propagation constant becomes $\beta_z = k_0$ is called the cutoff thickness. Waveguides with thicknesses larger than this cutoff thickness have at least one guided mode. For smaller profiles, all modes are radiating modes andwhich are not confined by the dielectric core. For a rectangular waveguide with a finite width, the cutoff thickness is smaller than the cutoff thickness of anthe infinite slab

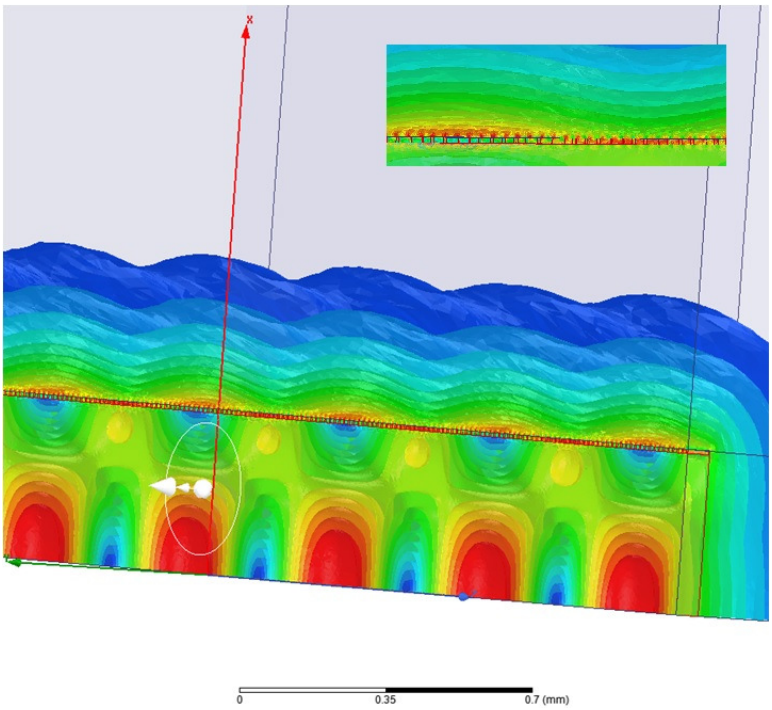

Figure 5.20: Magnitude of electric field vector simulated by ANSYS electronics software.

waveguide. However, there is no exact analytical solution to find the cutoff thickness in a rectangular waveguide. In Fig. 5.24, theoretical results are plotted only for b values at which $\beta_z > k_0$; simulation results are plotted also for smaller values of b at which guided modes were observed in simulation.

In Fig. 5.24, both the approximate analytical and numerical results show that the interaction impedances decrease, away from the cutoff point, when the width of the waveguide is increased. However, near the cutoff point, the interaction impedance calculated using the proposed approximate analytical method increases exponentially; the numerical result shows only a relatively small peak near this point.

The difference near the cutoff point comes from the large discrepancy between the exact field distribution of the electromagnetic field and the estimated field distribution obtained from the improved Marcatili method. This method is based on the assumption that the field is confined inside the waveguides core which is not valid near the cutoff point. As it is shown in Fig. 5.24, away from the cutoff point, there is good agreement between the approximate analytical and simulation results. Also, where an analytical solution exists for the slab waveguide, there is good agreement between the approximate analytical and

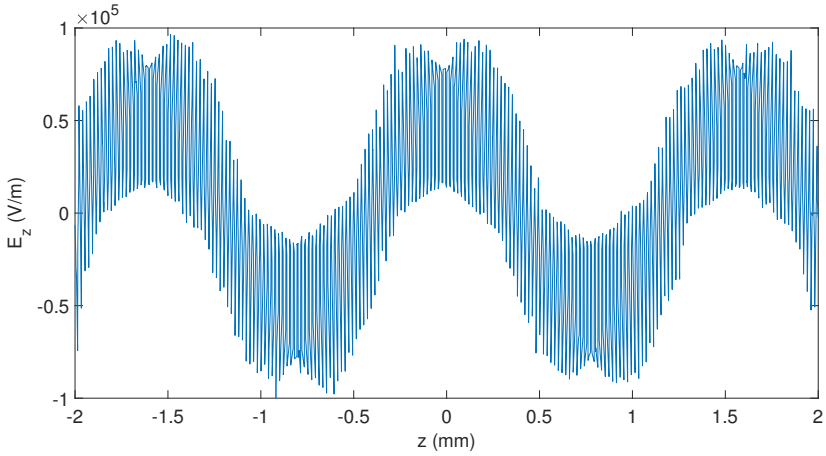

Figure 5.21: E_z component of electric field on surface of grating along line l_z (see Fig. 5.19), for $a = 125\mu m$, $b = 600\mu m$, $m_d = 0.3$, $t_g = 10\mu$m, and $l_p = 20\mu m$ at $f = 150GHz$.

simulation results (see Fig. 5.3).

Equation (5.66) can also be written as:

$$K_1 = \frac{|A_s|^2}{|A_2|^2} \frac{|A_2|^2 \left(1 + \sin(k_y a)/k_y\right)}{4P_{A0}\beta_1^2} \tag{5.69}$$

The expression on the left is a multiplication of two terms. The first term, $\frac{|A_s|^2}{|A_2|^2}$ (A_2 is defined in eq. D.2), represents the amplitude of the first-order space harmonic generated by the grating layer with respect to the fundamental harmonic. This term is determined mainly by the grating dimensions. The second term shows how much of the power is distributed along the surface of the grating. For thin gratings, it is mainly determined by the waveguide dimensions.

Figure 5.25 shows the term $\frac{|A_s|}{|A_2|}$ versus m_d for a grating with $t_g = 10\mu$m on top of a rectangular waveguide with $a = 125\mu m$ and $b = 600\mu m$. The normalized amplitude of the first-order space harmonic obtained from the approximate theoretical analysis is maximized at $m_d = 0.3$. However, for the values obtained from simulation, it is maximized at $m_d = 0.4$. As mentioned above, the normalized amplitude of the first-order space harmonic of the rectangular periodic field is maximized for a duty cycle of 0.3. For very small grating periods (small with respect to the wavelength of propagation), the field at the surface of the grating is very similar to the periodic rectangular wave. This approximation becomes less accurate for larger grating periods, justifying the difference between the approximate

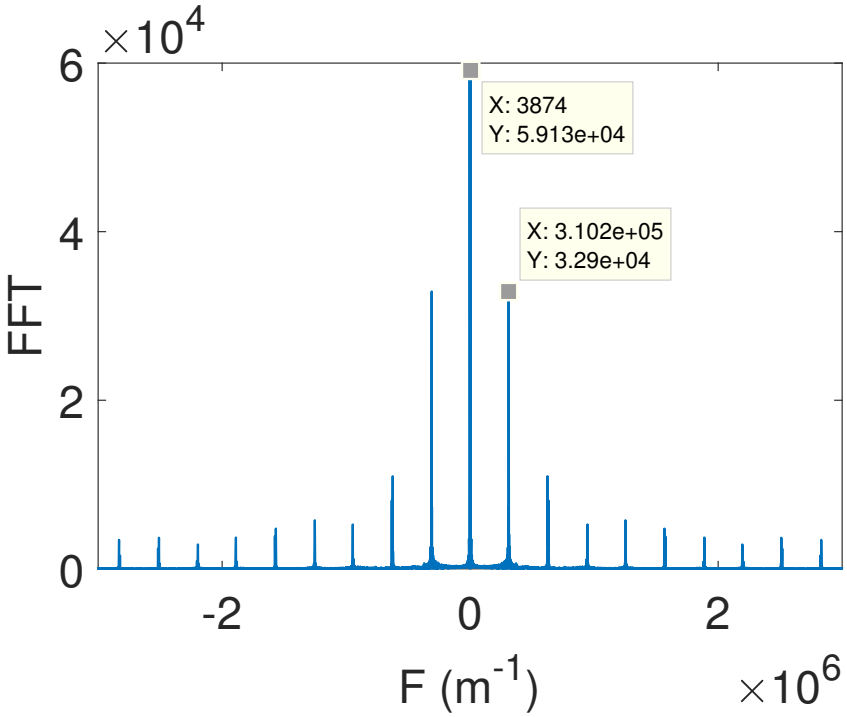

Figure 5.22: Fourier series transform of E_z component depicted in Fig. 5.21.

analytical and simulation results for a grating period of 20μm.

In chapters 3 and 4, (when calculating the conductivity of the graphene layer), and in this chapter (when calculating the dispersion equation from eq. 5.65), it is assumed that the electromagnetic field exciting the space charge density wave in the graphene has only the z-component on the surface of the graphene, parallel to the direction of the drifting current. The TM modes of an infinite slab waveguide have only the E_z component. However, hybrid modes in a dielectric rectangular waveguide have both E_y and E_z components at the surface of the graphene. In this case, for an exact analysis of the graphene, a conductivity tensor $\sigma = \begin{pmatrix} \sigma_{yy} & \sigma_{yz} \\ \sigma_{zy} & \sigma_{zz} \end{pmatrix}$ should be defined. The z- and y-components of the electric field are coupled through hydrodynamic equations, increasing the complexity of the analysis drastically.

Therefore, we have assumed that the E_y component of the first-order space harmonic is negligible with respect to its E_z component. To verify the accuracy of this assumption, the E_y field on the surface of the grating along the z direction for $a = 125\mu m$, $b = 600\mu m$, $m_d = 0.7$, $t_g = 10\mu$m, and $l_p = 20\mu m$ at $f = 150GHz$ is plotted in Fig. 5.26. Comparing the two plots of Fig. 5.21 and 5.26, it can be seen that E_y of the first-order space harmonic

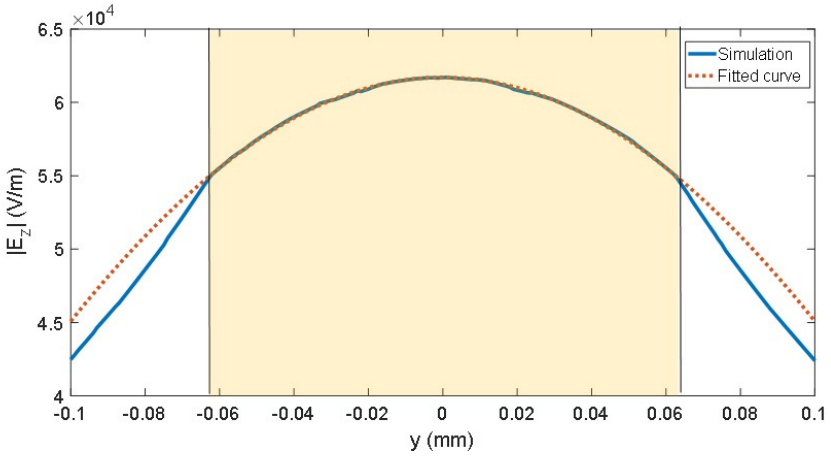

Figure 5.23: Field distribution of the field along y direction. Solid line is simulated field; dotted line is fitted curve; and colored area indicates inside of silicon waveguide.

is one order of magnitude smaller than its E_z component.

5.4 Conclusion

In this chapter, an analytic solution is presented to analyze electromagnetic wave propagation in a periodic structure in the presence of graphene. Analytic expressions are also given for the interaction impedance and gain of a proposed TWA. Within these expressions, each parameters individual effect on the overall performance of the structure is studied. Throughout the chapter, the approximations made for this method along with the conditions under which these approximations are valid are discussed.

The main contribution of this chapter has been to introduce an approximate theoretical method for analyzing Floquet modes in gratings on top of rectangular dielectric waveguides. This method gives explicit expressions for the interaction impedance of slow-wave grating structures, which are then used to design the waveguide and grating.

To verify the proposed approximation method, the results obtained with this method are compared with simulation results. To adjust the mesh size in accordance with the system memory, the period of the simulated gratings was set to be much larger than what is required for the proposed graphene TWA. Therefore, the simulation results are used only for verification of the theoretical results.

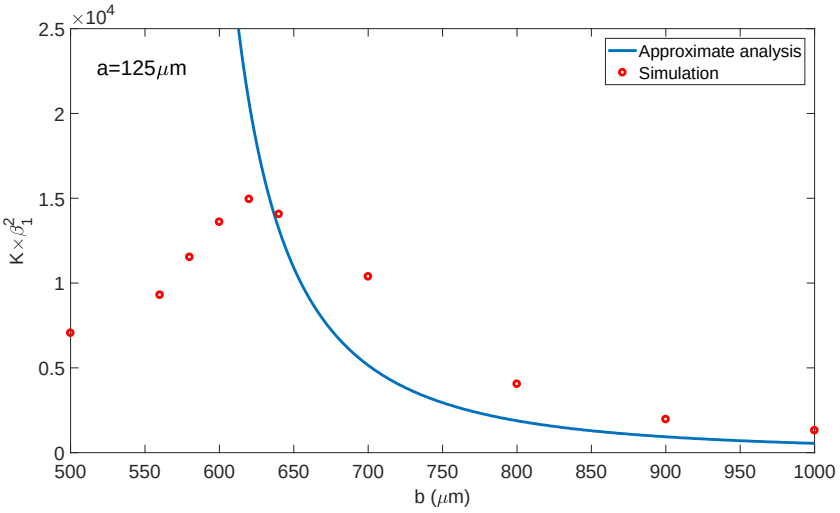

Figure 5.24: Coupling factor versus b with $a = 125\mu m$, $m_d = 0.3$, $t_g = 10\mu m$, and $l_p = 20\mu m$ at $f = 150GHz$. Results obtained using proposed approximate theoretical method (solid line); results obtained from simulation (dots).

Some of the assumptions made in the approximate theoretical method, such as the confinement of the first order space harmonic field to the surface of the grating, are less accurate for larger periods of gratings. However, there are still enough similarities between the results of the two methods to show that the approximate method is accurate enough for designing structures with nearly optimum gain. However, it may not be accurate enough to give the exact value of parameters such as the interaction impedance and gain.

The dimensions of the rectangular waveguide and the grating have now been determined. The next step, described in Chapter 6, is to fabricate the designed sample and verify the theoretical results with measurement results.

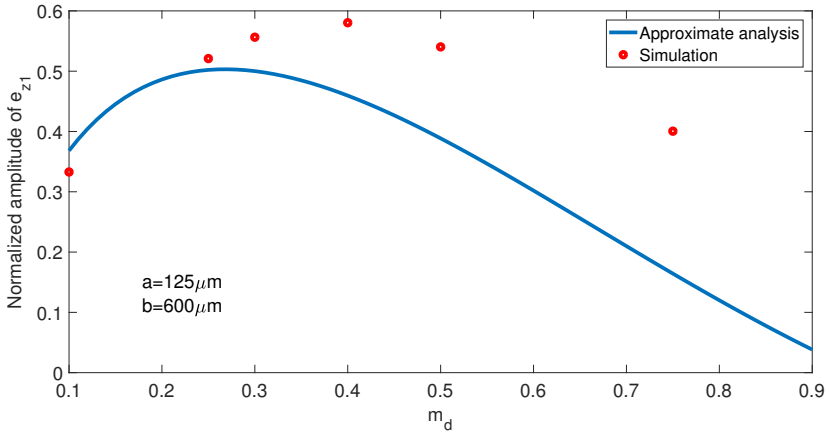

Figure 5.25: Normalized amplitude of first-order space harmonic as function of m_d. Results obtained using proposed approximate theoretical method (solid line); results obtained from simulation (dots).

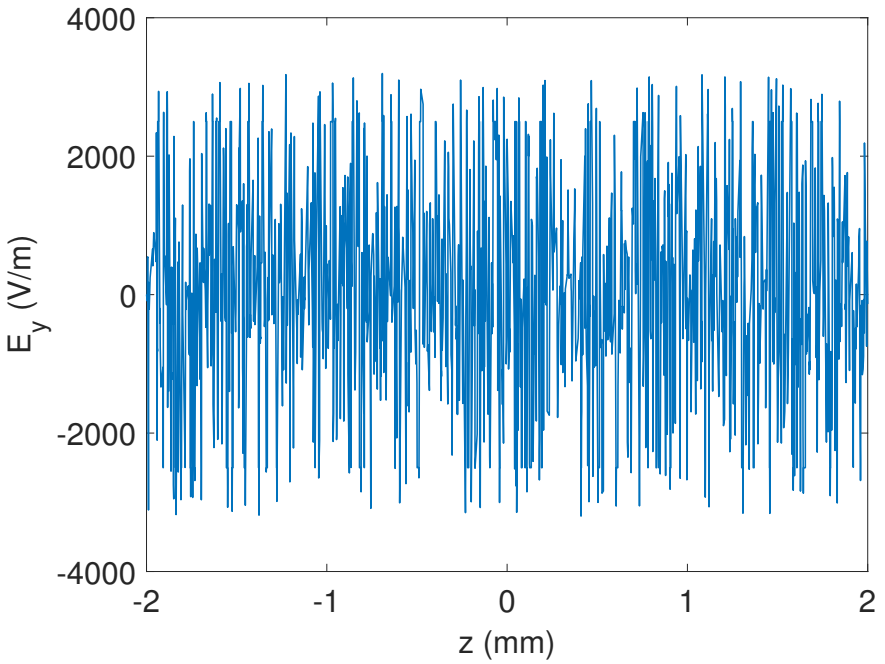

Figure 5.26: E_y component of electric field on surface of grating along line l_z (see Fig. 5.19), for $a = 125\mu m$, $b = 600\mu m$, $m_d = 0.3$, $t_g = 10\mu$m, and $l_p = 20\mu m$ at $f = 150GHz$.

Chapter 6

Fabrication and measurement

The proposed structure, depicted in Fig. 5.1, was created in three main stages (see Fig. 6.1):

- Fabrication of the grating. (6.1)
- Transfer of the graphene layer and fabrication of the DC bias contacts. (6.2)
- Fabrication of the silicon waveguide.(6.3)

This chapter details the steps taken in each stage of the fabrication process. The proposed travelling amplifier could have been designed and fabricated for use at 1 THz frequency (the frequency of interest in this thesis so far); however, to simplify and speed up the fabrication process, the prototype structure was fabricated for a frequency range of 110-170 GHz. The fabrication of such a device at 1 THz is more complicated, for two main reasons. The first reason is the long grating with smaller pitch. Because this grating is fabricated using the Electron Beam Lithography (EBL) method, a good electron beam focus is crucial and even a small change in height will knock the electron beam out of focus. This focus issue becomes more problematic for certain large area samples that require a homogeneous structure, and it is very difficult to overcome in small structures because higher resolution is required. The solution is to divide the large area into smaller parts, then align and pattern each separately, after refocusing the beam on the individual parts in series. Unfortunately, this is a time-consuming process.

For frequencies around 100 GHz to 400 GHz, a simple image silicon waveguide ([122]), a stand-alone waveguide that can be moved without having to be mounted on a handler,

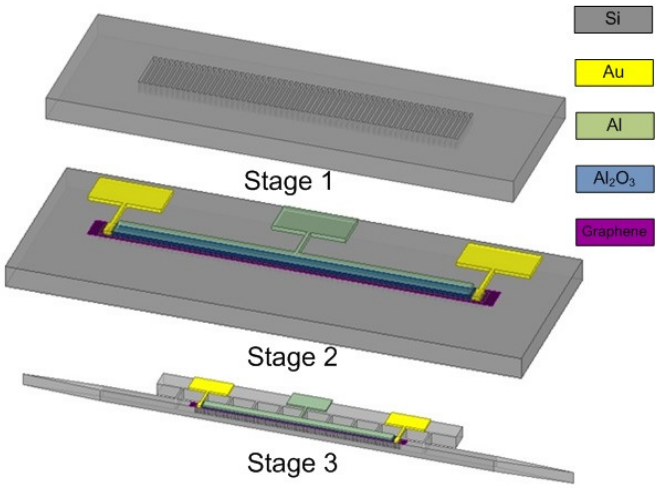

Figure 6.1: Three main stages of the fabrication process.

was used. However, at 1THz, this type of waveguide become very lossy; moreover, its very delicate structure means it should be mounted on a handling structure ([98,99,123]). This is the second reason why fabricating the structure at higher frequencies is more complicated. For these reasons a frequency of around 150 GHz was selected for fabricating the first prototype structure for proof of concept.

Various methods of etching and thin film deposition are known. In each step of the fabrication process, a suitable method whose outcome meets the required specifications was selected based on the advantages and disadvantages of each method. These are described in detail below.

There are two major types of etching: wet and dry. Wet etching uses liquid chemicals , usually mixtures of acids, bases, and/or solvents. The surface material is removed by chemical reactions. This form of etching is generally isotropic, and the material is etched uniformly in all directions. This can lead to undercutting, as the underlying film is etched from underneath the mask (Fig 6.2). Therefore, straight vertical walls cannot be fabricated and undercuts always exist. However, the chemical nature of the etch can lead to good etch selectivity, which is the main advantage of this method. Selectivity is the ratio of the underlying film etch rate to the mask etch rate. However, it is essentially isotropic. If anisotropic etching is desired, directionality must be induced into the etch process, and this can be achieved by dry etching.

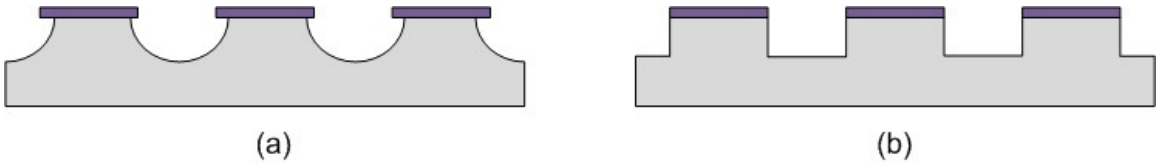

Figure 6.2: Schematic of (a) isotropic wet etching with undercut and (b) anisotropic dry etching with straight vertical walls.

Dry etching uses plasmas formed from gases as the etchant. Plasmas are usually composed of positively charged ions, electrons, and uncharged radicals. Applying an electric field causes the ions to be accelerated downward toward the wafer. Therefore, dry etching involves chemical reactions or physical removals or a combination of both [124].

There are three main types of dry etching [124]: sputter, chemical, and reactive ion etching (RIE). Sputter etching, in which a wafer is directionally bombarded by non-reactive ions, is a purely physical process. Such physical sputtering is highly anisotropic, due to the essentially vertical nature of the etching. However, the selectivity and etch rate are low. Usually, the mask etches at about the same rate as the substrate. Chemical etching is a purely chemical process that uses neutral free radicals reaction with substrate material. It is highly selective, but isotropic. RIE combines chemical etching and physical sputtering, to gain both sufficient selectivity and directionality. Since the process combines both physical and chemical interactions, it is faster than the other two methods.

In a simple RIE system, an RF voltage is applied to a pair of electrodes in the etch chamber. Electrons are accelerated by the generated RF electric field. The electrons collide with other atoms and molecules, thereby ionizing them, and releasing additional electrons which accelerate and collide with further atoms. The resulting chain reaction generates electrically conductive plasma.

The lower electrode is connected to a blocking capacitor, that is gradually biased to a negative potential, referred to as a self-bias and represented by V_{dc}. Electrons with small mass follow the oscillation of the RF electric field. On the other hand, ions with masses of approximately 100,000 times larger move relatively little in response to the RF electric field. However, due to the large negative V_{dc} at the wafer platter, the ions accelerate down toward the wafer surface. Since the V_{dc} value depends on the RF power, the RF plasma source determines both ion density and ion energy. The ions react chemically with the materials on the wafer, but can also knock atoms off the surface by transferring their kinetic energy [125].

As mentioned above, in simple RIE systems, both ion density and ion energy are determined by a single RF source value. With high plasma densities, better etch rates can be achieved, and with high ion energies, more anisotropic etch profiles can be achieved. High process flexibility is achieved by having separate control over the ion energy and ion density. For this purpose, other types of RIE systems exist, called inductively coupled plasma (ICP) RIE.

ICP-RIE systems use two independent RF sources. One RF generator applies power to the ICP coil. This coil, located in the plasma generation region, creates an RF magnetic and electric field that energizes electrons so as to ionize gas molecules and atoms. Therefore, the ICP RF source controls ion densities, while the RF bias power, applied to the wafer platter, extracts and accelerates ions and radicals from the plasma towards the wafer surface. This configuration results in the independent control of ion density and ion energy, leading to higher etch rates, greater process flexibility, and more control over the anisotropy of etching.

A modified version of RIE is deep reactive ion etching (DRIE), used to create very deep, high aspect ratio structures. By using DRIE, very thick features, up to 500 μm or more can be etched. There are two main technologies used for high-rate DRIE: cryogenic etching and the Bosch process. The Bosch process is the most-common production technique, and is used mainly for etching silicon substrates.

The Bosch process comprises a sequence of alternating steps (no more than a few seconds long): a passivation step and an etch step [126]. The typical DRIE system uses an ICP source to provide a high-density plasma, and an independent substrate power bias to provide directional ion bombardment during the etch step. In the passivation step, a protective layer of polymer is deposited by Plasma Enhanced Chemical Vapor Deposition (PECVD). Octafluorocyclobutane (C_4F_8) gas is typically used for this passivation step. The deposited Teflon-like polymer protects the already-carved features from further lateral etching.

The passivation step is followed by the etch step, during which, the vertical sidewalls of the silicon are relatively protected by the C_4F_8 induced polymer layer. However the horizontal surfaces, although also coated with polymer, are sputtered off by the directional ion bombardment, and thus exposed to the chemical etchant. The silicon is then etched nearly isotropically by a chemical reaction. The typical etchant gas for silicon is sulfur hexafluoride (SF_6). The iteration of these passivation/etch cycles creates a large number of very small isotropic etch bites called ripples. To etch through a $300\mu m$ silicon wafer, for example, 600700 etch/deposit steps are performed. The cycle time affects the etch rate. Long cycles yield a higher etch rate but larger ripples. Short cycles yield smoother walls

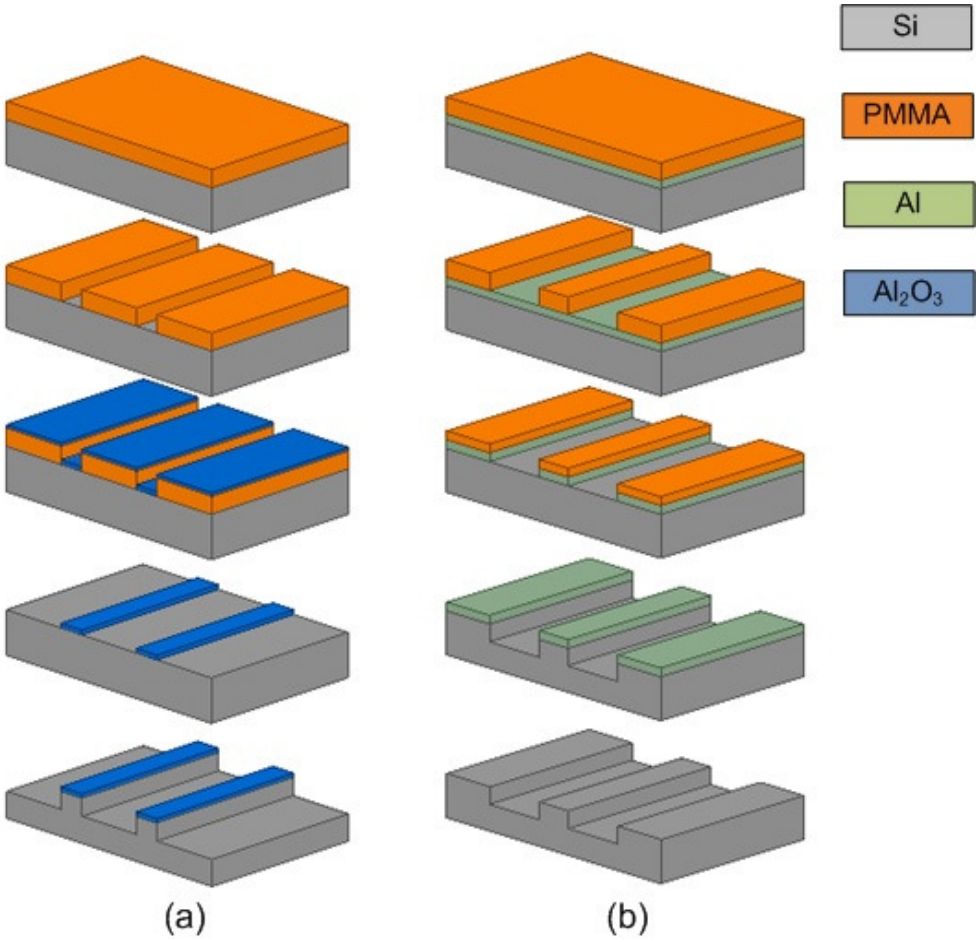

Figure 6.3: Process flow for two methods of grating fabrication.

and a lower etch rate. In this thesis, the Bosch process was used to fabricate rectangular silicon waveguides with a thickness of 300 μm and a shadow mask with a thickness of 200 μm.

In this thesis, the ICP-RIE technique was used to fabricate the grating structures with a very small pitch size (around 300 nm). As the silicon width was around 90 nm, a small amount of undercut will change the filling factor drastically. For example, a 20 nm undercut will change the filling factor from 0.3 (which gives the maximum interaction impedance), to 0.17 giving an interaction impedance 2.4 times smaller than its maximum value (see Fig. 5.15). Therefore, a very directional etching profile with no undercut is required. This can be achieved by optimizing the ICP RF source power, platen RF bias power, gas flow rates,

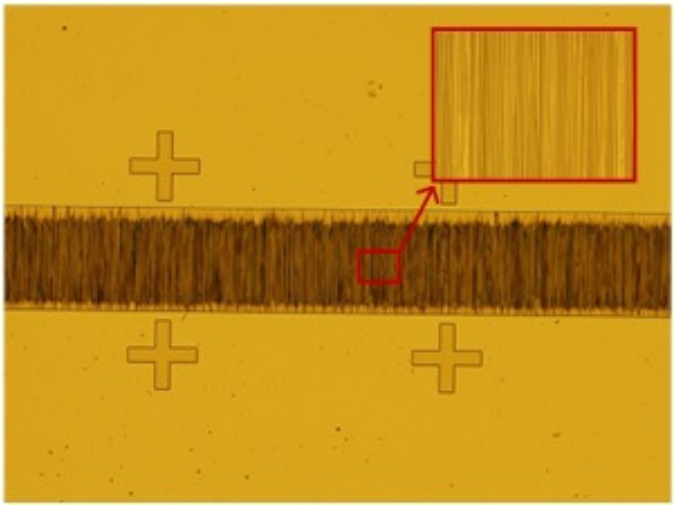

Figure 6.4: Microscope image of grating fabricated using Method 1 (Fig. 6.3(a)).

flow cycle time and temperature. In addition, to increase the anisotropy of the etching, as in the Bosch technique a mixture of etch gas (SF_6) and passivation gas (C_4F_8) is used, but are released at the same time, resulting in smoother sidewalls than is possible with the Bosch approach, but shallower etching.

Two thin film physical deposition methods were used in this project. For the lift-off process, where direct pattern coating is required, an electron beam evaporation system is used. However, for depositing a very thin layer of aluminum (20 nm), to be etched in to the silicon mask later, a sputtering system was used. Compared with the E-beam evaporation system, the sputtering system provides better thickness control and more pure aluminum (it is less oxidized, which makes the etching process easier).

6.1 Fabrication of the grating

In the first stage of fabrication, the grating structure is constructed and the graphene sheet transferred onto it. The fabricated grating structures have a width of 100-150 um, length of 1 cm, thickness of 300 - 600 nm, pitch size of 312 nm and a filing factor of 0.15-0.3.

Two different fabrication methods were tried in this research. The first involved fewer steps; however, it was difficult to obtain uniform structures with few defects. The second was more reliable and repeatable. It yielded better quality gratings with few defects

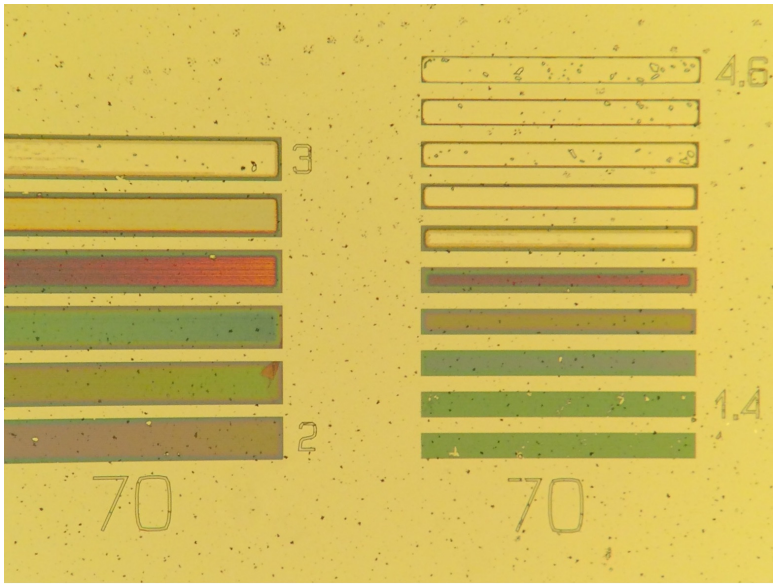

Figure 6.5: Microscope image of a test pattern after etching of silicon. Numbers at the bottom of each column represent the line width of the written test pattern in micrometers, and the numbers beside each bar are the dose factors. All gratings have the same period of 312 nm. However, as the filling factors differ the colors of the test gratings also differ.

and little inhomogeneity. However, this fabrication process had more steps than the first approach.

The fabrication steps of the first method (Method 1) are as follows:

Step 1: Cleaning the silicon piece. This is done using the Piranha process or using an ultrasonic bath of acetone and Iso Propanol Alcohol (IPA).

Step 2: Polymethyl methacrylate (PMMA) coating. The PMMA950- A3 was spin coated with a speed of 2000 rpm and an acceleration of 500rpm/s for 45 seconds. After this, it was baked on a hot plate at 180C for 17.5 minutes. The final thickness of the PMMA resist was around 160 nm.

Step 3: Patterning the grating and alignment marks via electron beam lithography. Because of the feature size and overall size of the patterned structure, a 20 KV acceleration voltage and a 30 μm beam current aperture were selected. Higher voltages and smaller aperture sizes result in higher resolution and grainy images for very small

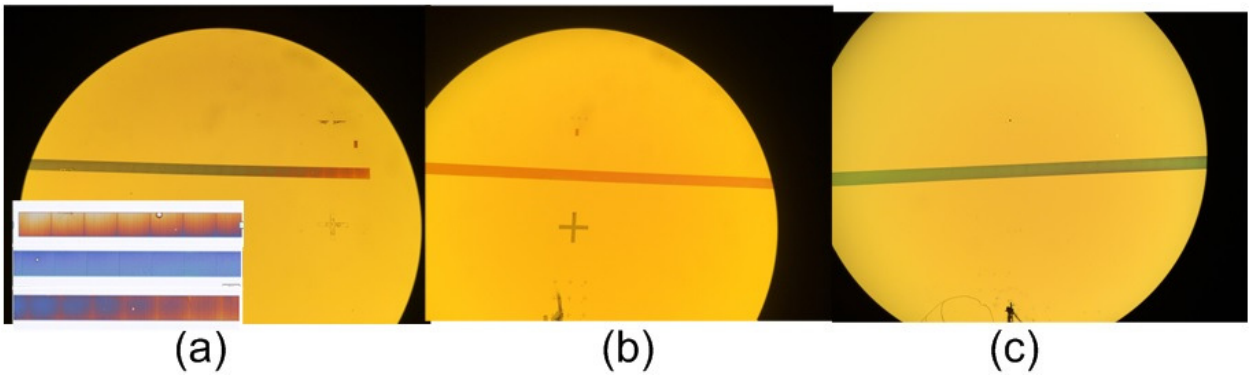

Figure 6.6: Microscope images of fabricated gratings with period of 312 nm with (a) non-uniform filing factor of 0.3 at the middle and 0.15 at the end points, (b) uniform filling factor of 0.5, and (c) uniform filling factor of 0.3. The total length of each grating is 1 cm, but only 5 mm of each is shown in each image. The inset in (a) shows the focused image at the middle and two end points.

apertures. On the other hand, lower voltages and larger aperture sizes result in less heating damage and charge up, and smoother images.

Step 4: PMMA developing. The PMMA was developed for 30 sec in a mixture of methyl-isobutylketone (MIBK) and IPA with a ratio of 1:3 followed by dipping in IPA for 30 sec.

Step 5: Deposition. Depositing 20-30 nm of Aluminum or Aluminum oxide Al_2O_3 using an E-beam evaporating system.

Step 6: Liftoff. For the liftoff, the sample was put in remover PG for 24 hours.

Step 7: Etching. The silicon was dry etched into the grating using aluminum or Al_2O_3 as a mask, using a mixed gas of SF_6 and C_4F_8 in an ICP-RIE system (Oxford Plasmalab 100 ICP380 Etcher).

Step 8: Mask removing. The aluminium mask was removed by putting it in aluminium etchant for 6-7 minutes. The Al_2O_3 mask was kept on the sample since it does not affect the electrical response of the grating significantly.

The process flow is shown in Fig. 6.3(a). The grating with a period of $1\mu m$, depth of $1\mu m$ and filling factor of around 0.3, fabricated with this method is shown in Fig. 6.4. The grating has many defects and is not uniform.

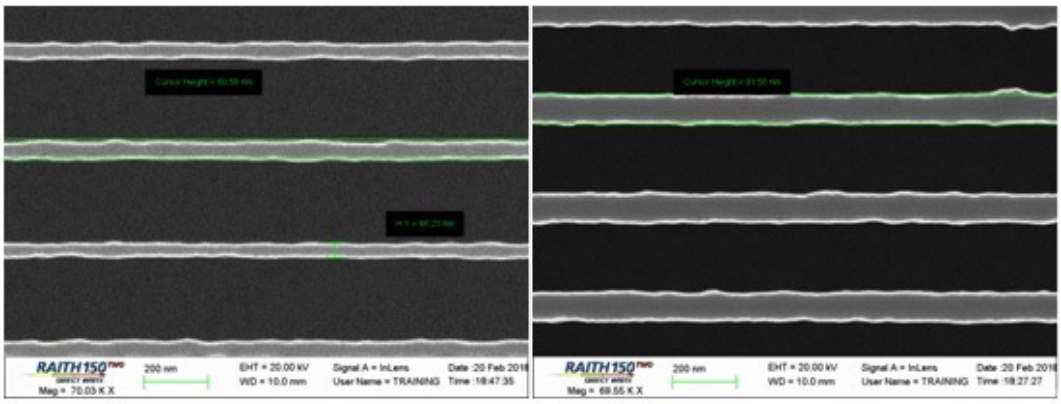

Figure 6.7: SEM image of the first fabricated grating at (a) the middle and at (b) the end point. The silicon teeth, d_{Si}, are 91.5 nm wide at the middle of the grating and $45 - 60$ nm at its end. A microscope image of this grating is shown in Fig. 6.6

The steps involved in the second approach (Method 2) used for grating fabrication are given below. There is a brief discussion of each step and some of the practical issues involved in each step are pointed out.

Step 1: Cleaning the silicon piece. Done using the Piranha process.

Step 2: Depositing 20-30 nm of Aluminum. Accomplished using a sputtering system.

Step 3: PMMA coating. The PMMA was spun to a thickness of approximately 160 nm and baked at 180C for 17.5 minutes on the hot plate.

Step 4: Grating pattern written with 20 KV acceleration voltage and 30 um beam current aperture. Choosing a higher voltage and smaller aperture size results in better resolution, at the cost of slower scanning speed. Since the area of the structure is large, a 20 KV and 30 um aperture were chosen and resulted in both acceptable resolution and patterning time.

The developed pattern is wider than the scanned pattern due to proximity-effect phenomena. Therefore, before patterning the main grating, a test pattern consisting of small gratings with different line widths and dose factors was written on the sample. Figure 6.5 shows a microscope image of a test pattern after the etching of silicon. All the gratings have the same period of 312 nm; however, the colors differ due to the different filling factors of the gratings. Writing a pattern with a higher dose results

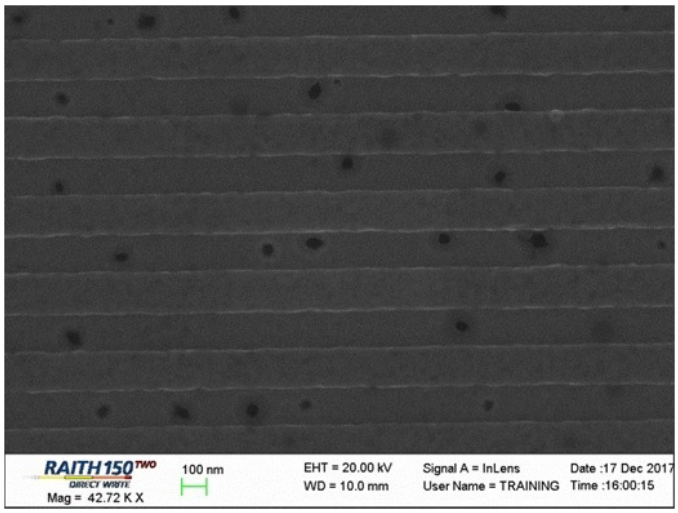

Figure 6.8: SEM image of a grating sample for which the fabrication went wrong because the PMMA residue was not fully removed after MIBK development.

in a grating with a smaller filling factor. For gratings with filling factors between 0.25 and 0.35, the color varies from blue to green. The color changes to orange when the filling factor decreases to around 0.15.

After Scanning electron microscope (SEM) imaging on a developed sample, the right width and dose was selected for the main structure. Since a small change in temperature and PMMA thickness will change the final result, it is better to do the dose test on part of the main sample, then pattern the whole grating on it later, rather than conducting of doing the dose test on a separate test piece.

Electron beam focusing, with aperture stigmation and write field alignments, was performed at a point near to the center of the grating. The grating is 1 cm long. Therefore, close to the two ends of the grating, the electron beam loses its focus. Figure 6.6(a) shows a microscope image of the center and two end points of the first fabricated grating. The silicon teeth at the center of the grating are 92 nm wide.However, the width gradually changes further away from the center, becoming $\sim$60 nm at each end (see Fig. 6.7). To solve this issue a larger silicon piece was selected. This, allowed for the use of a clip on either side to hold the sample, rather than having it held by only one clip at the center. The resulting gratings are depicted in Fig. 6.6(b) and (c). The color of the grating indicates its uniformity along the whole structure.

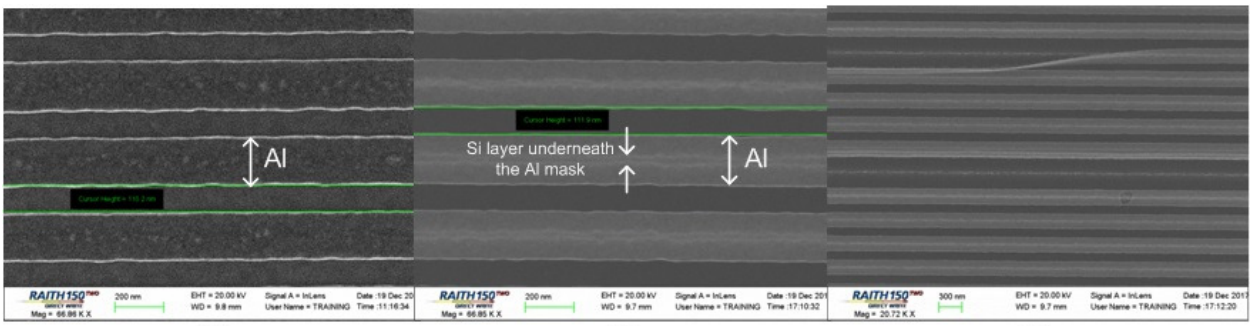

Figure 6.9: SEM images of aluminum mask (a) before silicon etching, (b) after silicon etching but before mask removal, and (c) a zoomed-out view of (b). The rough light lines are the edges of the etched silicon teeth underneath the thin aluminum layer.

Step 5: Developing the sample. Done in MIBK:IPA 1:3 for 30s followed by 30s rinsing in IPA.

Step 6: Etching 10 nm of PMMA. This was completed, using 5 second oxygen plasma etching, to remove possible unwanted PMMA residue remaining after developing. Figure 6.8 shows the effect of remaining PMMA residues after silicon dry etching on a final grating. After development, the PMMA layer acts as an etching mask for the next step.

Step 7: Through-etching of the aluminum layer. Using ICP-RIE with the gas mixture of Cl_2 and BCl_3. The etching process takes only 5 seconds. Therefore, a pre-process with the same temperature and gas flows, should be run first for a few minutes to stabilize the chamber temperature and the gas inside the chamber. This pre-process, reduces the typical variance of ICP-RIE processing. After the aluminum etching, the remaining PMMA mask was removed with acetone or PG remover, followed by 40 second of oxygen plasma ashing. The aluminum layer acts as a hard mask during the silicon dry etching process.

Step 8: Etching of silicon using ICP-RIE with a gas mixture of C_4F_8 (passivation gas) and SF_6 (etchant gas). To obtain high anisotropy and near zero undercutting, the platen RF bias power was set to 30W, whereas the ICP RF power was set at the lowest possible value that can generate stable plasma but keep the plasma density low. The temperature was also set at T=0. This low temperature slows down the chemical reactions that produce isotropic etching. The flow rates of the C_4F_8 and SF_6 gas were first set equally (15 sccm). However, the side walls were not completely straight, and

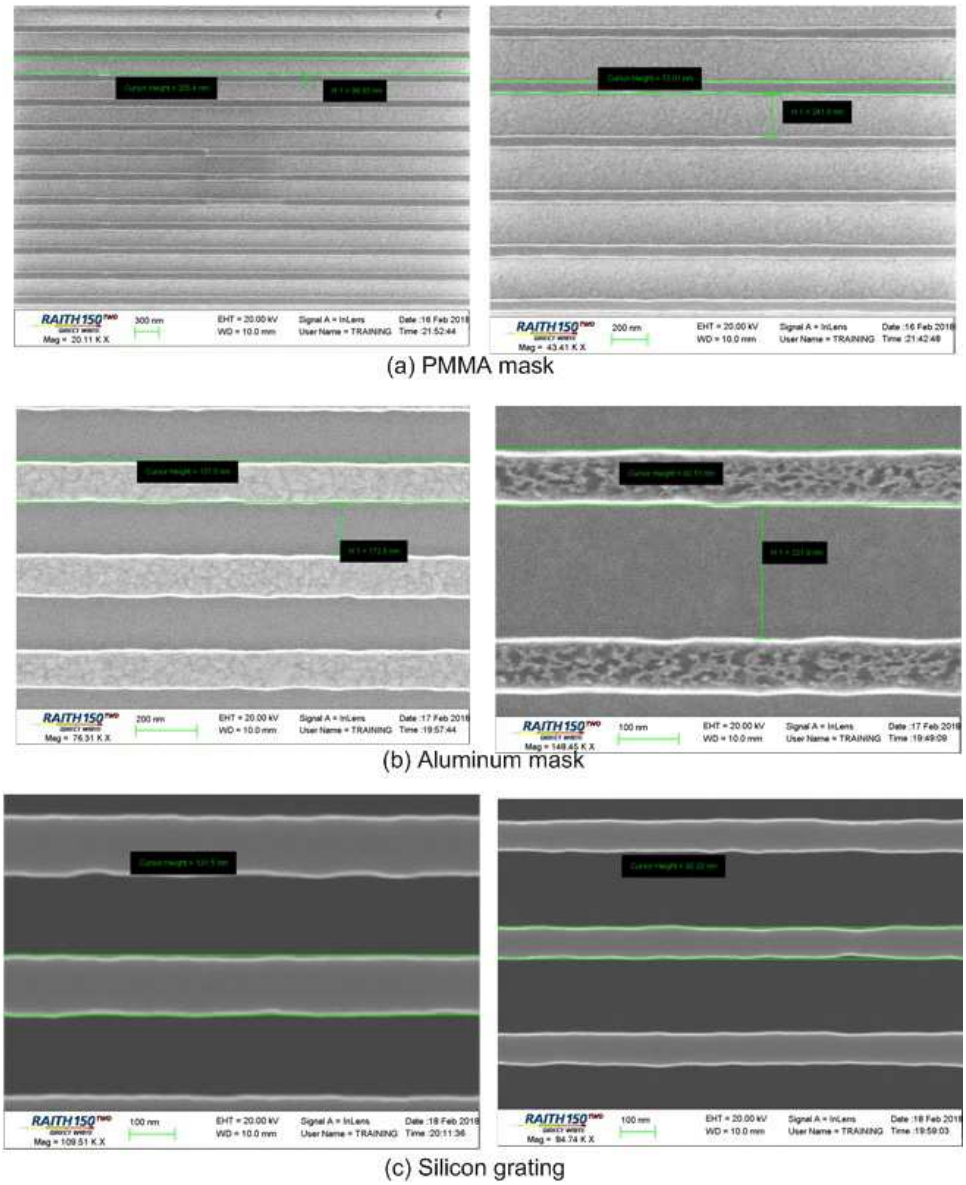

Figure 6.10: SEM images of two gratings with $d_{Si} \simeq 132nm$ (pictures on the right) and $d_{Si} \simeq 92nm$ (pictures on the left), at three stages of the fabrication process: (a) the PMMA mask (after step 5 of the fabrication process described in the text); (b) the aluminium mask (after step 7), (c) the final fabricated grating.

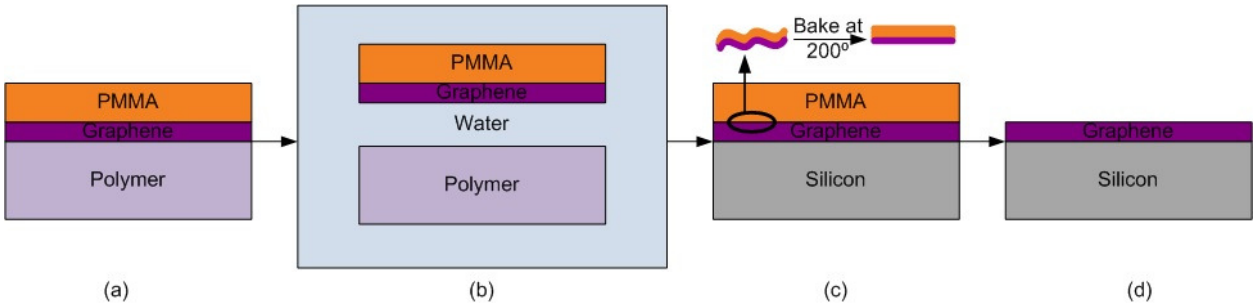

Figure 6.11: Schematic illustration of the graphene transfer procedure.

there was lateral etching and significant undercutting. Figures 6.9(a) and (b) show a grating before and after silicon etching, respectively. In Fig. 6.9(b) the aluminium mask has not been removed. The light lines represent the edges of the etched silicon teeth underneath the aluminium layer. Figure 6.9(c) shows part of the sample where a couple of aluminium strips are peeled away and the etched silicon layer becomes visible.

In the next run, to improve the anisotropy of the etching profile, the flow rate of the C_4F_8 gas was increased to 25 sccm while keeping the flow rate of the SF_6 at 15 sccm. This change achieved better anisotropy and almost zero undercut. The etching rate was around 0.4 nm/s. Figure 6.10 shows the PMMA mask, the aluminium mask, and the silicon grating after removing the aluminium layer for two gratings with different silicon teeth widths. Comparing the width of the aluminium strips in Fig. 6.10(a) with the width of the silicon tooth in Fig. 6.10(b) shows that an undercut of less than 3 nm was achieved.

Step 9: Removing the aluminium mask. The sample was immersed in the aluminum etchant solution for 6 to 7 minutes.

6.2 Transfer of the graphene layer and fabrication of the DC bias contacts

Mass fabrication of large-area uniform monolayer graphene is achieved by CVD. In this project, as a graphene layer with a length of 1 cm is needed, PMMA coated CVD graphene is used. Figure 6.11 schematically illustrates the graphene transfer procedure. The graphene

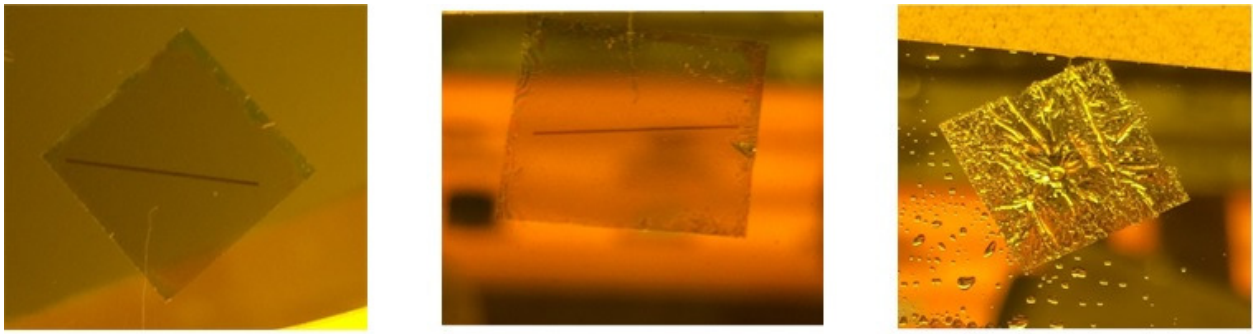

Figure 6.12: Photos of transferred graphene layers locate on top of gratings. In (a) and (b), graphene layers transferred successfully with no wrinkles or bubbles. Figure (c) shows an example of unsuccessful transfer of graphene with some air bubbles trapped underneath.

should be fully wetted, before being dipped very slowly into distilled water; if it is nott will roll up or even fold. Therefore, a few droplets of IPA are placed on a spongy fabric layer underneath the graphene piece to be absorbed.

The PMMA-coated graphene film was floated on the water surface. It should remain there for around 2 hours to ensure that water is in contact with the complete undersurface of the film and not separated from it by air bubbles trapped underneath the graphene (Fig. 6.11(b)). The PMMA layer makes the graphene layer visible. With the graphene floating on the waters surface, the sample was placed beneath it at an inclined angle, and then gently lifted to come into contact with the graphene sheet. Further gentle pulling brought the substrate from the water, with the graphene layer resisting smoothly on it. The graphene layer thus lies on the substrate, with some excess water that is washed away with a few droplets of IPA added on top of the substrate. The water is replaced with IPA since the latter evaporates and dries faster. At this point, any air bubbles remaining underneath the graphene sheet can be removed by adding more IPA and tilting the substrate to one side. While the graphene film was still wet, the substrate was inclined from side to side in all directions to help the graphene sheet move across the substrate and locate on top of the grating. This procedure should be done as gently as possible to reduce tearing and winkles on the graphene film. Then, the graphene was put aside and left to dry naturally for around 30 minutes. Figure 6.12(a) and (b) shows photos of two successfully transferred graphene layers with no wrinkles and bubbles. In contrast, Figure 6.12(c) shows an example of unsuccessful transferring of graphene with a few air bubbles trapped underneath.

After 30 minutes, the sample was baked on a hot plate for 20 minutes at 60°, then 20

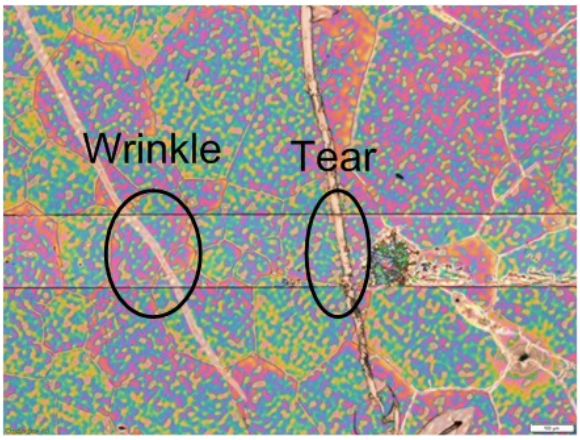

Figure 6.13: Defects in graphene after transfer on to the silicon substrate.

minutes at 100°-120°, followed by 30 minutes at 200°, allowing the PMMA to reflow as it was baked. This last part is essential to increase the adhesion between the graphene and the substrate. Graphene follows the surface roughness of the underlying copper during the growth process. Therefore, the PMMA coated graphene film is wavy and rough and so does not lie flat on the substrate surface. Baking the PMMA at 200 allows it to reflow and slightly stretches and flattens the graphene, as shown in the inset of Fig. 6.11(c) [127,128]. Once the sample has cooled, the PMMA is removed by acetone.

Before removing the PMMA layer the graphene was investigated to check for any cracks or tears specially on the grating (See Fig. 6.13). If any cracks or tears were located on the grating then the sample was cleaned and a new graphene sheet transferred onto it. Samples without cracks or tears were ready for the next step: fabricating the DC biasing structure.

The DC biasing structure consists of three layers: 1) drain and source contacts which are connected to the graphene layer through ohmic contacts, 2) an insulator layer covering the graphene layer, and 3) the top gate layer. The source, drain and gate are extended and connected to the large rectangular metallic pads where the connections to the DC biasing board are made.

Before fabricating the drain and source contacts the graphene was patterned using optical lithography with positive photo resist AZ p4620. The AZ p4620 was used as a mask for removing uncovered graphene area, using oxygen plasma ashing for 20 seconds at low temperature (descum process). This was followed by removing the photo resist mask using either heated acetone or acetone at room temperature for 24 hours, or sometimes,

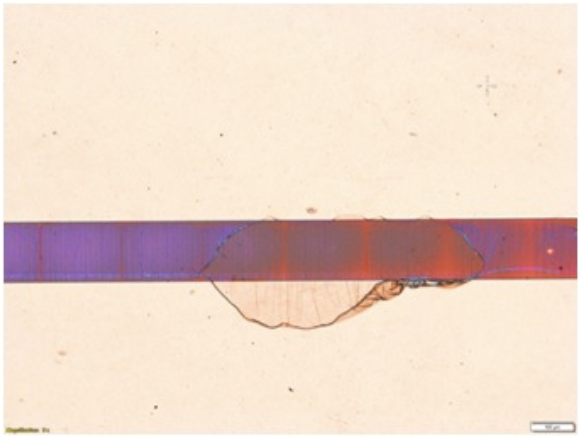

Figure 6.14: Graphene delamination after strong liquid pressure force applied with pipette.

both. The adhesion of photoresist to graphene is stronger than the adhesion of graphene to the substrate, especially after the plasma treatment. Thus, the graphene delaminates when the photo resist is removed using ultrasound or pipette to apply strong liquid pressure (see Fig. 6.14).

The residual photoresist will dope graphene, causing major problems for fabricating graphene devices [129]. The photoresist residue after photolithography is more than the residue after EBL, leading to weak device performance [130, 131]. An experiment in [132] showed that photoresist residue can be effectively removed by a ethyl-2-pyrrolidone based remover.

The fabrication of each layer of the DC-biasing structure consisted of the following steps:

Step 1: Spin coating of the negative photo resist ma-N 1410 with a speed of 3000 rpm and acceleration of 500 rpm/s for 60 seconds. The sample was then baked on a hot plate at 110° for 90 seconds. The resulting thickness of the photo resist was around 950 nm.

Step 2: Optical lithography using chrome photomask. The resist was exposed to UV light with an intensity of 350 mW/cm^2 at a wavelength of 365 nm for 35 seconds. The exposure time value was determined using dummy samples to achieve the correct dimensions and desired resist sidewall profile. The longer the samples were exposed to radiation, the thinner the lines were. For example, for a line width of 80 μm on the mask, an exposure time between 35 to 40 seconds resulted in a line width of 76

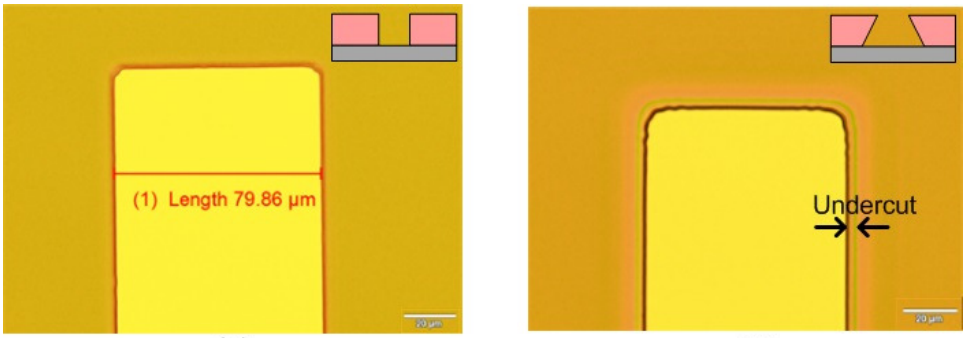

Figure 6.15: Optical microscope image of sample after ma-N 1410 resist developed in ma-D 533/S for (a) 50 seconds (no undercut) and (b) 2 minutes (with undercut). The light brown region is where exposed resist remains, while the yellow region is the silicon surface after removal of unexposed resist. The band surrounding the yellow region in Figure (b) indicates an undercut of about 3 μm.

to 80 μm after development. On the other hand, with a negative resist, less exposure means more developer attack, leading to more undercut. Therefore, considering all of these factors, an exposure time of 35 second was selected.

Step 3: Developing the sample in ma-D 533/S developer. In the first experiment, the sample was developed until the unexposed photo resist part dissolved completely, which took around 50 seconds. However, this time was not sufficient to achieve a good undercut profile (see Fig. 6.15(a)), a key element for a good lift-off result. Therefore, the developing time was increased to two minutes. The resulting undercut is shown in Fig. 6.15(b)

Step 4 :Deposition of thin film materials using an electron beam evaporation system. The deposited layers are as follows:

layer 1: 10 nm of chrome or titanium and 60 nm of gold;

layer 2: 75 nm of Al_2O_3;

layer 3: 10 nm of chrome and 80 nm of aluminum.

The titanium and chrome layers are used to increase the film's adhesion to the substrate.

Step 5: Lift-off. The goal of this crucial process is to wash away the photoresist in a solvent, together with the material deposited on its top. After the lift-off, only material in

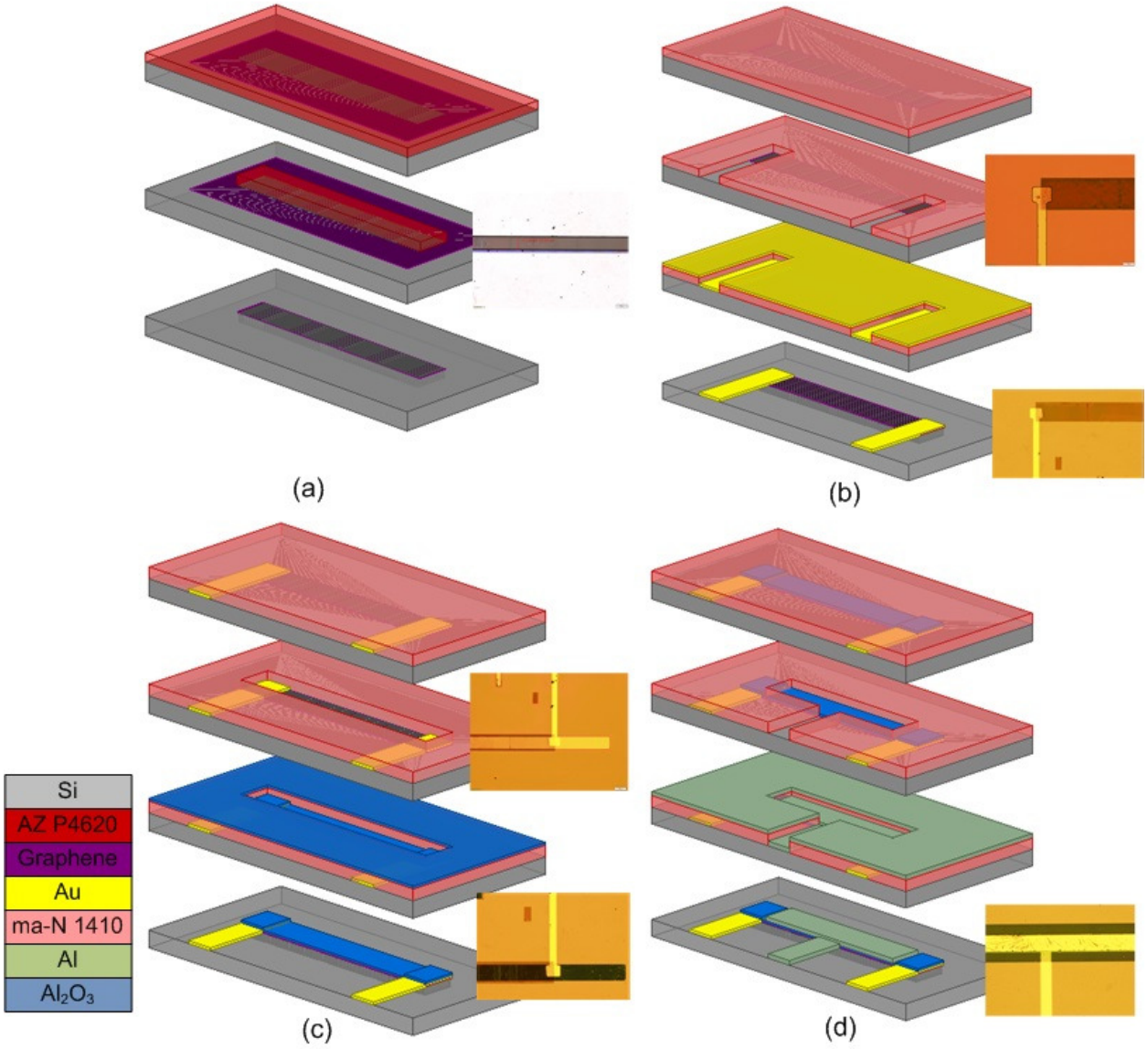

Figure 6.16: Fabrication flows for (a) patterning of graphene layer, (b) fabricating drain and source contacts on the graphene, (c) adding insulator layer and (d) fabricating top gate contact. For some steps, an optical microscope image of a fabricated sample has been added.

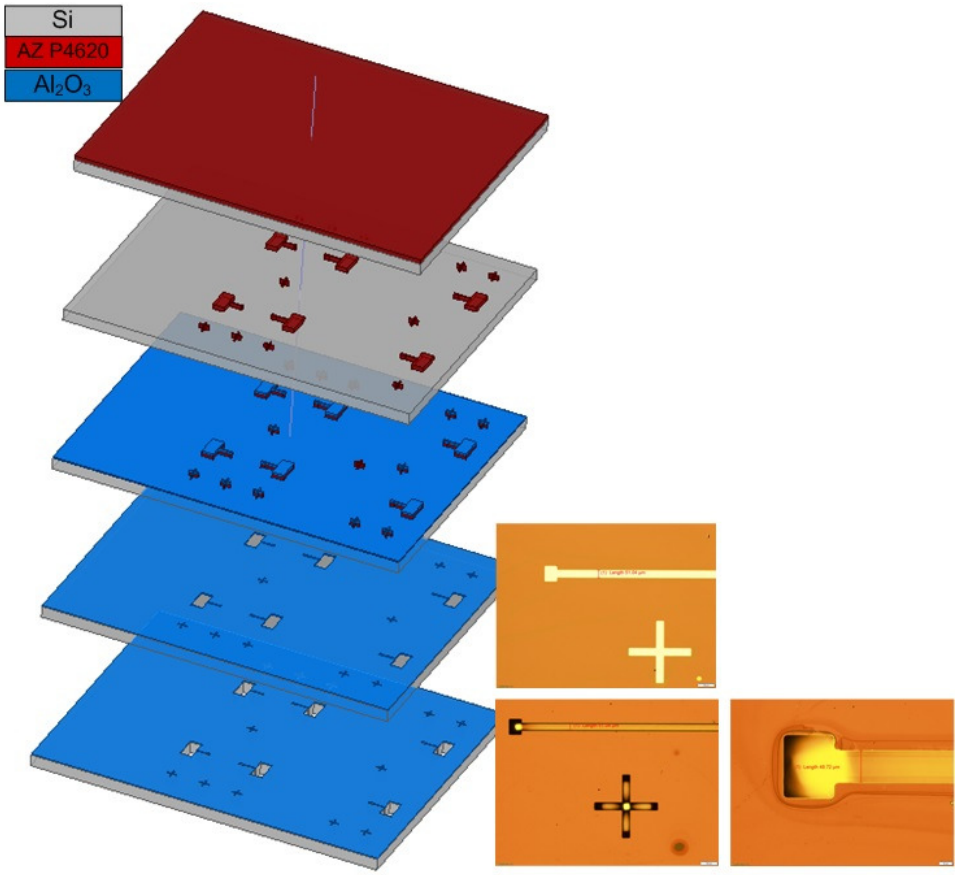

Figure 6.17: Fabrication flow for shadow mask. For some steps, an optical microscope image of a fabricated sample has been added.

direct contact with the substrate should remain. In some cases, unwanted small flakes of the metal layer adhere so well to the remaining parts that clean lift-off does not occur. In these cases, the application of small force with ultrasound or a pipette removes the unwanted flakes.

The main difficulty arises from the fact that the bonding of the graphene to the substrate is based on weak Van Der Waals forces. The low adhesion of graphene to the substrate prevents the facilitation of the lift-off process using ultrasound. The ultrasonic force will remove not only the photo resist and the material on top but also the material deposited on the graphene, potentially damaging the graphene as well. The best that can be done is to put the sample in the solvent after the deposition

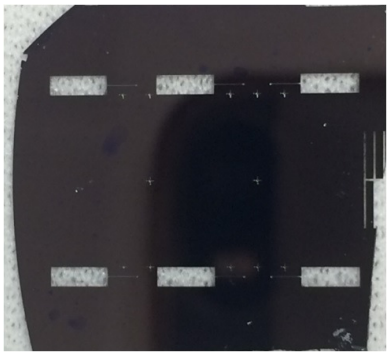

Figure 6.18: Fabricated shadowmask.

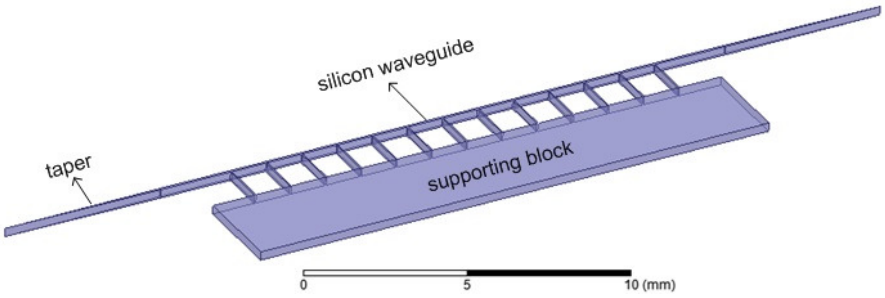

Figure 6.19: Silicon waveguide with a supporting block attached to it.

until the material layer on top of the photo resist is cracked and peels off from the substrate. Then, with the use of liquid pressure from a pipette, the lift-off process can be completed.

Acetone and remover PG can be used as solvents for the photo resist. However, the graphene layer interacts with remover PG and starts to detach and curl back on itself. Therefore, for the first layer, when the graphene layer had not yet been covered, the sample was put in the acetone for 24 hours, and for the second and third layers, the heated PG remover was used.

During the lift-off process, particles of metal may be redeposited on the surface, contaminating the sample at random locations. To prevent this, and to help the lift-off process, parts unnecessary to the deposition were covered and exposure of the contacts area and surround was minimized.

$a = 125\mu m$, $b = 620\mu m$, $t_g = 540nm$, $m_d = 0.28$ The process flow for the fabrication of the DC biasing structure is shown in Fig. 6.16. For some steps, an optical microscope

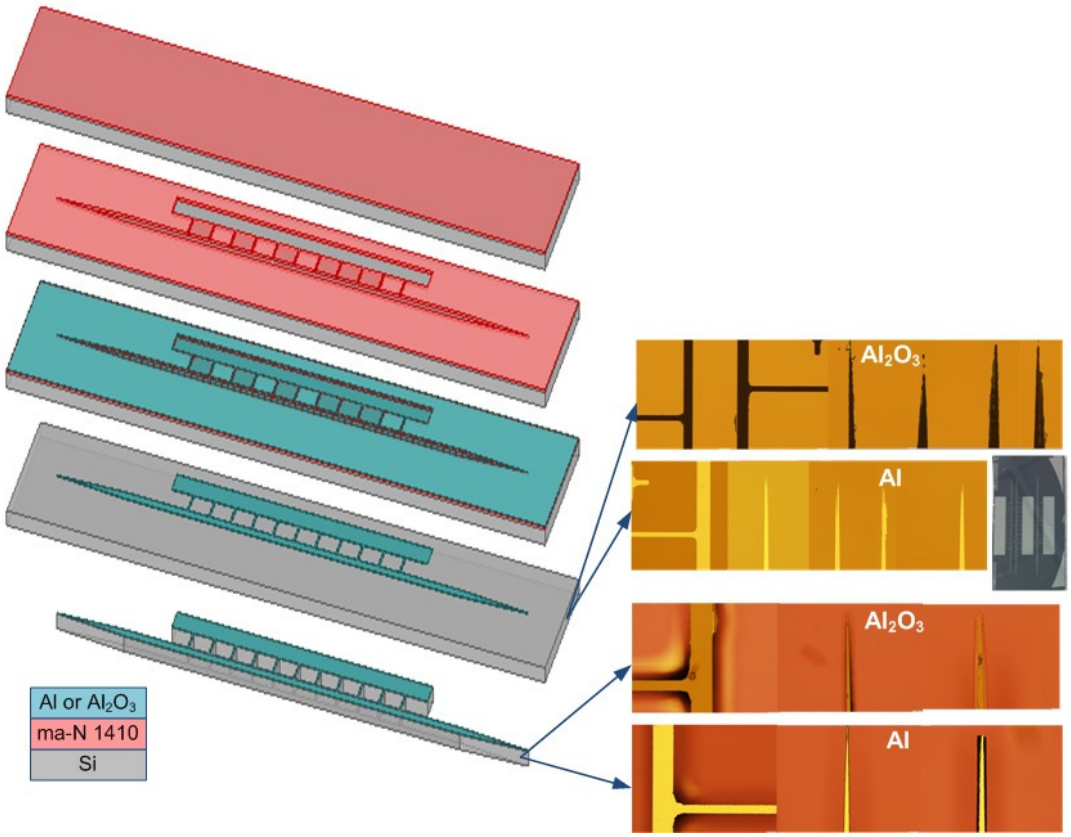

Figure 6.20: Process flow for fabricating silicon waveguide using Al_2O_3 and Al mask to etch waveguide. For some steps, optical microscope images and photos of fabricated samples have been added.

image of the related fabricated sample is also added. The inconsistency in processing graphene is a major obstacle. The photolithography method described above for patterning and subsequent contacting of the graphene poses problems; the etching and unreliable lift-off processes may affect the quality of the graphene by creating defects and introducing contaminants. Contaminants or solvent residues may be reduced by cleaning and/or annealing procedures. Polymer residues, however, are more difficult to remove and harsh cleaning methods may result in defects to the graphene layer or its delamination [133].

To find methods that did not have these disadvantages, other methods were investigated, including Atomic Layer Deposition (ALD) techniques and shadow masks.

ALD is a thin-film deposition approach based on a vapor phase technique capable of

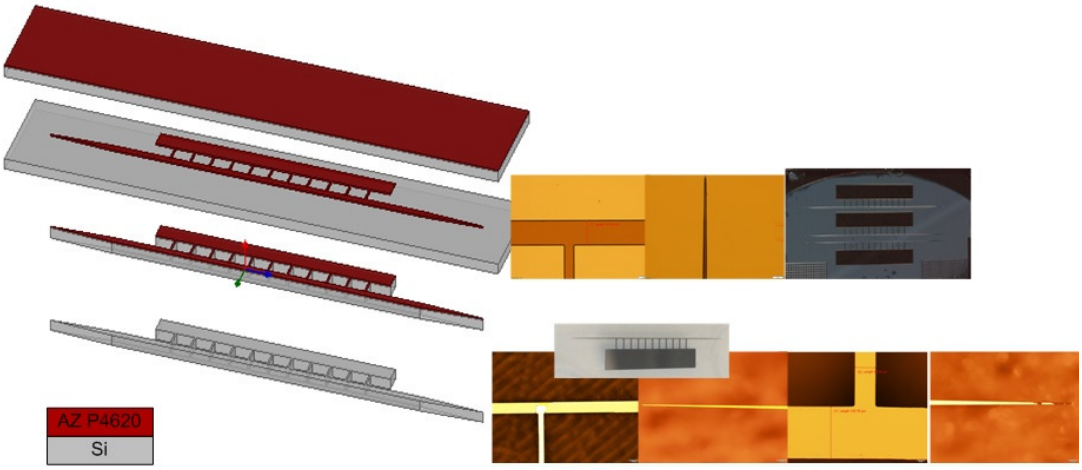

Figure 6.21: Process flow for fabricating silicon waveguide using AZ P4620 mask to etch waveguide. For some steps, optical microscope images and photos of fabricated samples have been added.

depositing thin films one atomic layer at a time. ALD is based on sequential, self-limiting reactions and so offers exceptional conformality. With these advantages, along with its capability to produce tunable film composition, ALD has emerged as a powerful tool for many applications in microelectronics.

There are two main approches for patterning ALD-grown films have been used in the literature: (i) patterning based on lithography and lift-off or etching; and (ii) area-selective ALD by area-deactivation or area- activation. There has been much interest in patterning by area-selective approaches since they can eliminate compatibility issues associated with the use of solvents, etchants, or resist films when working with sensitive materials. The ALD patterned films are superior to sputtered or evaporated films in continuity, smoothness, conformality, and minimum- feature size. The low deposition temperature prevents damage to the photoresist, such as from significant outgassing or hardbaking of resist layers underneath.

ALD of thin films on graphene is, however, a much more complex task due to the lack of out-of-plane bonds and surface hydrophobicity of the graphene [134]. There are no reactive adsorption sites on the perfect graphene surface. However, boundary regions, wrinkles and defects, typical in CVD graphene, are nucleation centers for ALD films.

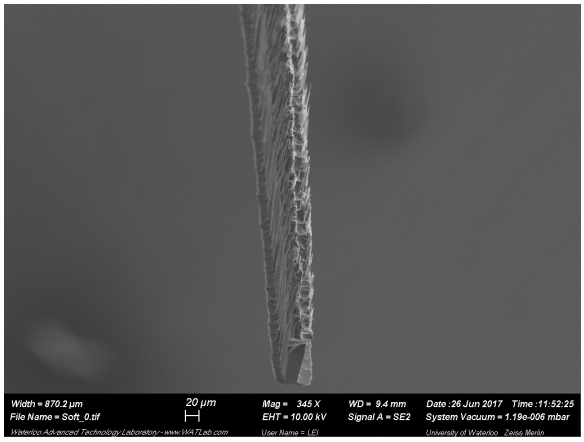

Figure 6.22: SEM image of the tip of the waveguide. Photoresist layer did not adhere properly to the substrate, causing lateral etching through the gap under the resist.

Thus, the uniform deposition of ALD film on graphene without any surface preparation techniques is impossible. Different techniques to initialize ALD growth on graphene have been investigated in the literature. These techniques include the use of different types of seed layers [135–137], ozone and plasma treatments to create functional groups [138, 139], and enhance nucleation by tuning the underlying substrate [140]. Research is ongoing to develop a method that does not damage the graphene, and/or degrade the electrical properties of graphene such as its carrier mobilities.

Paradoxically, the difficulties of growing ALD on graphene can be exploited in the fabrication of graphene and graphite-based structures through self-aligned ALD. In this technique, the material is selectively deposited on the materials where it is desired, eliminating the nano-scale alignment difficulties and multistep lithography processes.

Another method for fabricating contacts on graphene is to replace the patterned photoresist layer with a shadow mask. A shadow mask is a thin sheet with pattern features etched completely through it. After being positioned in intimate contact with the substrate, it is placed into the electron beam evaporation system. The thin film material is deposited through the mask directly on the substrate. This simplified process eliminates several steps associated with the photolithography and lift-off processes without contaminants or residues affecting the quality of the graphene. However, shadow masks are not good for high-resolution applications. Furthermore, shadow mask alignment is more difficult than the alignment in photolithography, and it is not as accurate. In this thesis, 200 μm silicon was employed to fabricate a shadow mask, using the fabrication procedure illustrated in Fig 6.17. and described below:

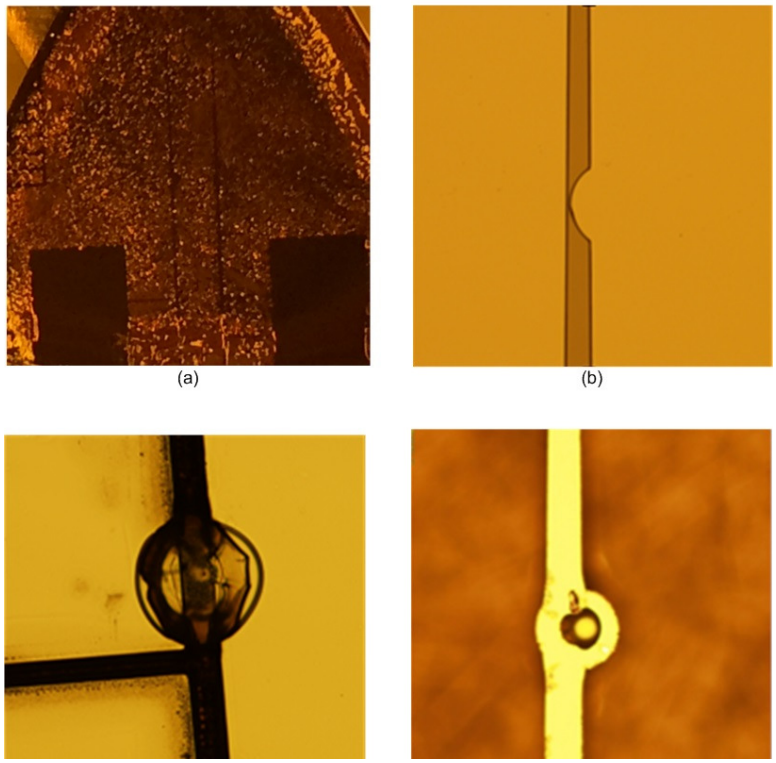

Figure 6.23: (a) Remaining solvent in the resist out-gassed after exposure and filled exposed area with micro-cavities. (b) Effect of a bubble on a sample after photo resist development. (c) Bubble created during dry etching. (d) Effect of a bubble created during dry etching on a sample after etching.

Step 1: Positive photo resist AZ P4620 was spun to a thickness of approximately 10 um and baked at 115°C for 90 seconds.

Step 2: Optical lithography was carried out using the same chrome photomask as the one used in the previous method to pattern contacts on the negative photoresist.

Step 3: The photoresist was developed in AZ developer 1:4 for around 2 minutes 20 seconds, followed by 1 minute rinsing in water.

Step 4: 100 nm Al_2O_3 was deposited using the electron beam evaporator system.

Step 5: The sample was soaked in the PG remover to accomplish the lift-off process.

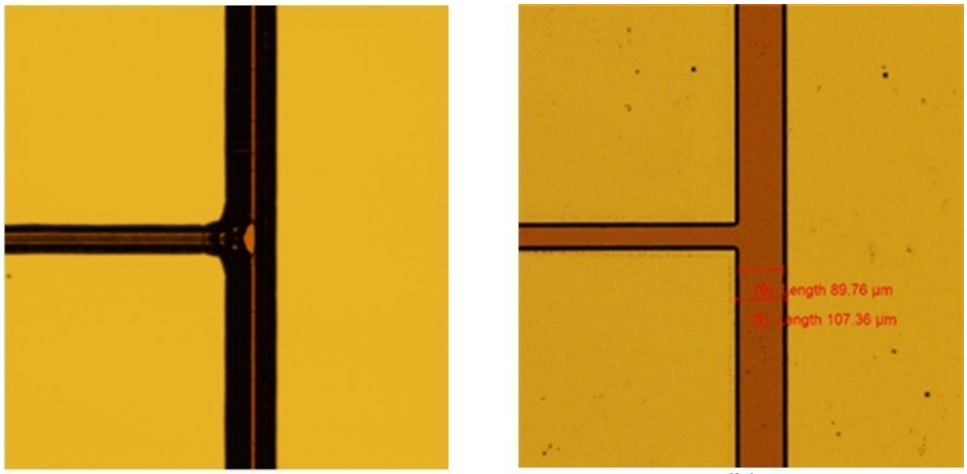

Figure 6.24: Microscope image of two AZ-P4620 patterns with different exposure times: (a) 75 seconds, and (b) 58.4 seconds. The black bond around the pattern indicates the angled sidewalls.

Step 6: Through etching of 200 um silicon was performed using the Al_2O_3 layer as a mask, in the Oxford Plasmalab 100 ICP380 system, using the Bosch process. Al_2O_3 is a chemically inert material and gives appropriate selectivity.

The fabricated shadow mask is shown in Fig. 6.18. Rough alignment under the optical microscope led to a misalignment of around 100 μm. The alignment precision can be improved to 5-10 μm by using a shadow-mask aligner equipped with a three-axis micropositioner and 1 rotation axis and 2 tilt axes. At the time of measurement, this system was not available.

6.3 Fabrication of the silicon waveguide

The last stage is to etch the silicon substrate into the silicon waveguide and its attached supporting block (see Fig. 6.19). The etch thickness is around 300 um. Therefore, the challenges of this stage are in controlling the lateral etching so as to fabricate straight wall waveguides, and in using an etch mask that can resist the long etching process. For the latter, either a mask with very high selectivity or a very thin mask with typical selectivity can be used. Therefore, two different types of mask materials were tested for the etching

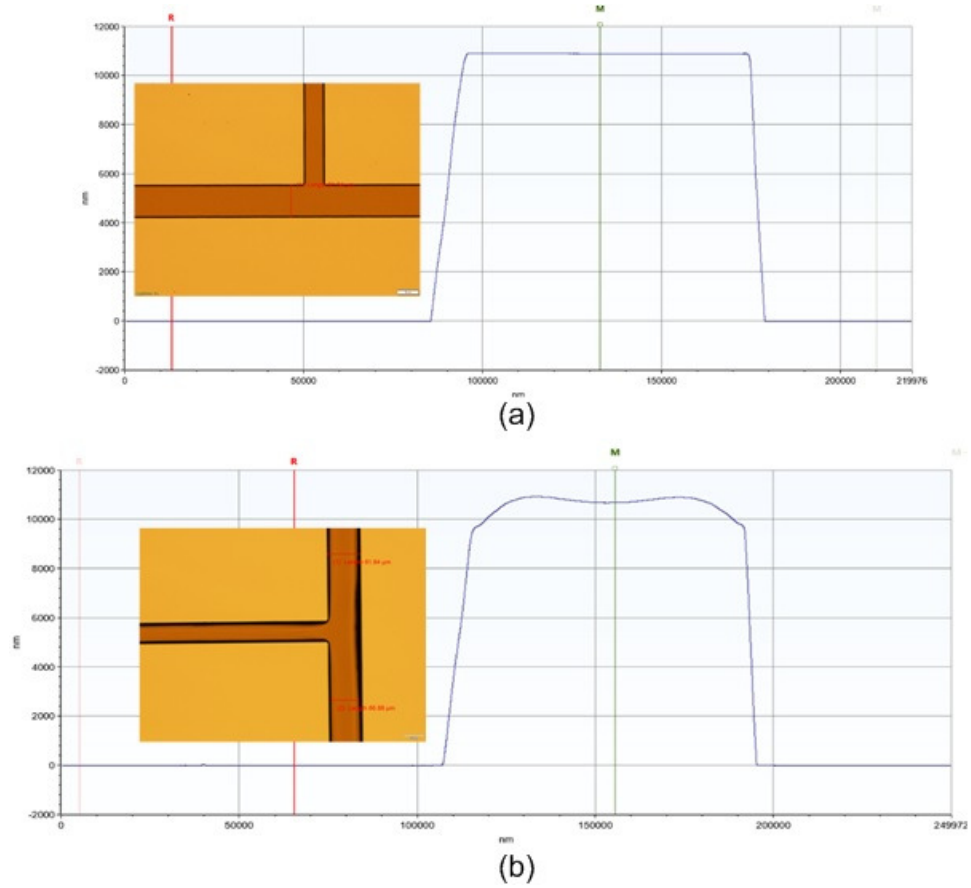

Figure 6.25: Profile pattern of 11 μm AZ P4620 photoresist (a) before and (b) after post bake at 110°C for 5 minutes. Insets are corresponding microscope images.

process: soft masks made of thick layers of the positive photo resist AZ P4620, and hard masks made of Al_2O_3 and Al.

The selectivity of the hard masks is very high [141]. Any reactions Al_2O_3 and Al have with the etchant gas SF_6 are too small to perceive; attempts to measure any changes in the thickness of hard masks before and after etching with filmetrics and profilometer were unsuccessful. However, based on the experiments done, it is possible to say the selectivity is greater than 1000 and 5000 for aluminum and aluminum oxide, respectively.

Using a hard mask required additional deposition and lift-off steps, as depicted in Fig. 6.20. The hard mask was fabricated by coating the sample with 950 nm of negative photo resist ma-N 1410 followed by patterning the photo resist via optical lithography. Then,

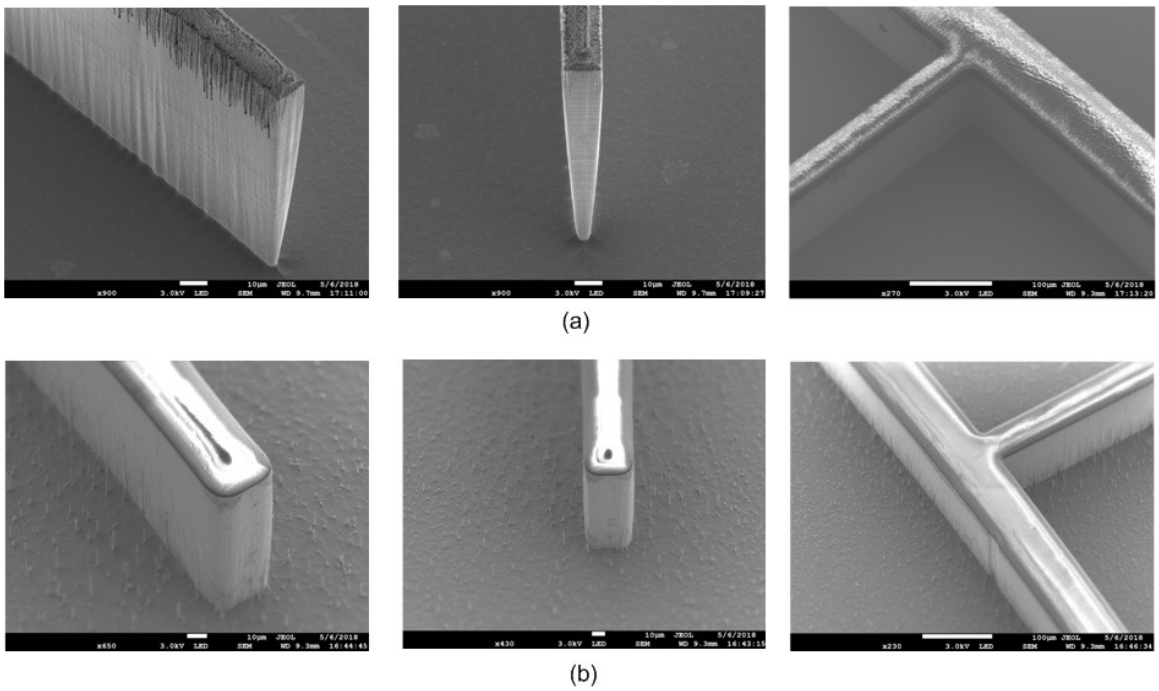

Figure 6.26: SEM image of silicon waveguide etched by (a) standard Busch process with a patterned AZ-P4620 mask, and (b) Busch process with longer passivation time step, with the same AZ-P4620 mask, postbaked at 110° for 5 minutes.

100 nm Al_2O_3 or Al were deposited by electron beam evaporation. The lift-off process was accomplished in PG remover heated to 80°C (see Fig. 6.20). A very clean lift-off is required, as any small flakes of material remaining after the lift-off lead to rippling along the edge of the etched waveguide.

The patterned photo resist layer can also be used as an etch mask. For this purpose, the thick photo resist AZ P4620 was used. Figure 6.21 illustrates the fabrication steps. The details of each step are explained below. The surface preparation before coating is an essential step for proper adhesion. Weak resist adhesion could result in the resist pattern peeling off after development, or unwanted lateral etching through the gap under the resist (Fig. 6.22). Surface moisture is a major factor that degrades resist adhesion. Therefore, surface preparation consists of dehydration through baking to remove surface moisture then the addition of an adhesion-promoter, hexamethyl disilizane (HMDS). The substrate dehydration and vapor deposition of HMDS were performed in a YES HMDS prime oven.

The selectivity of the photo resist is around 20 to 30. Therefore, the etching of 300

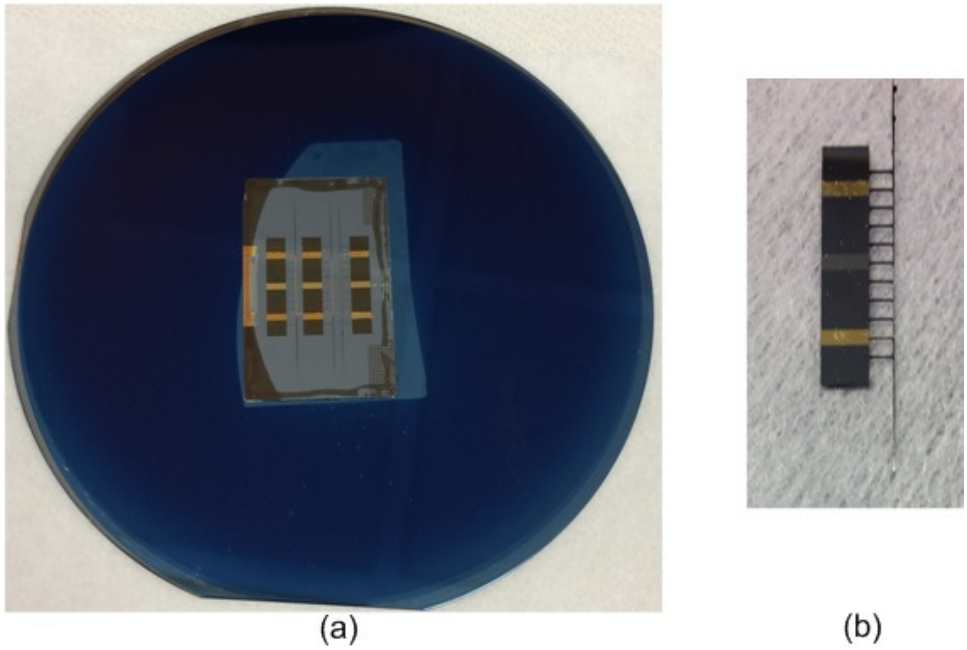

Figure 6.27: (a) Sample before etching mounted on aluminum-oxide-coated wafer. (b) Fabricated sample.

um silicon requires a photo resist thicker than 15 um. For this resist, the maximum thickness of the single coat is around 17 μm, and the required thickness can be achieved by a single-coating. However, the solvent content of the resist is vaporized more rapidly and more efficiently by successive spinning and baking processes. Therefore, a thick resist of around 24 μm was achieved by spinning the photo resist, then baking it on a hot plate, then repeating the spin-bake cycle. For both spinning processes, the photoresist was first spread at a speed of 500 RPM for 10 seconds, followed by a spin at a speed of 2000 RPM for 25 seconds. Different durations and temperatures were tested for the two baking processes.

AZ P4620 is a DNQ-novolac photo resist, consisting of novolac resin, an organic solvent, and diazonaphtoquinone (DNQ) photoactive compounds. The excess solvent should be removed by softbaking after the photo resist coating. If the softbake is short and/or the temperatures are too low, the dork erosion will increase, and the high remaining solvent concentration may cause bubbles during exposure or dry etching (see Fig. 6.23). The solvent will out gas and the resist layer will be filled with micro cavities (see Fig. 6.23(a)). On the other hand, high temperatures or long baking times will thermally decompose a significant amount of the photo active compound, lowering the development rate signifi-

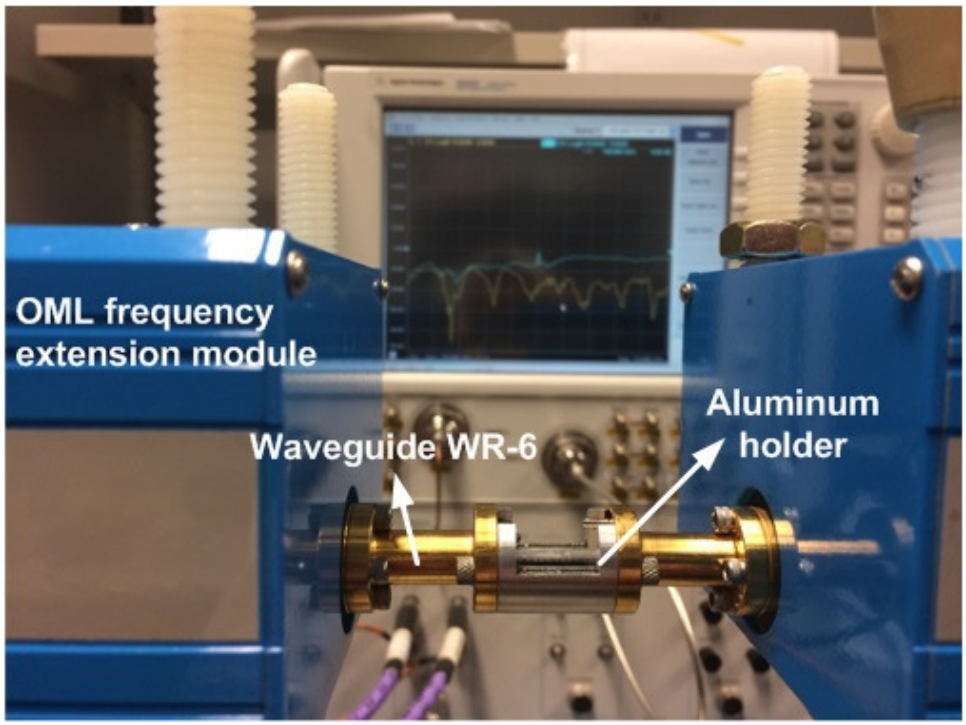

Figure 6.28: Measurement setup.

cantly [].

The best result was achieved with a soft bake temperature and time of 110° and 80 seconds for the first layer and 115° and 10 minutes for the second layer. Lower temperatures resulted in bubbling, and higher temperatures resulted in very difficult or even impossible development.

A certain water content in the DNQ-based resist is required during exposure to attain a high development rate []. Softbaking, however, makes the resist film almost water-free. Thus, the required water is gradually drawn from the air into the resist film. Therefore, a delay between baking and exposure is necessary for rehydration of the photoresist film. This time depends on the photoresist's thickness, air temperature and humidity.

After more than 3 hours rehydration time, the photoresist was exposed to a UV light wavelength of 405 nm with an intensity of 25 mW/cm^2 for 58.4 seconds. Exposure time was adjusted to achieve steep resist sidewalls. Exposure doses that are too high cause undesired exposure by scattering, diffraction and reflection. As a result, too much of the resist is dissolved during development. On the other hand, the resist is not developed successfully

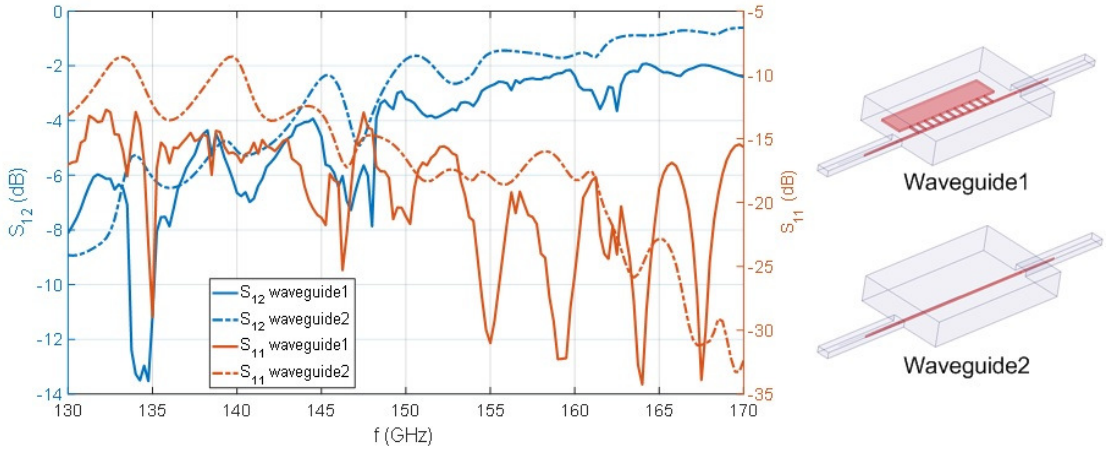

Figure 6.29: Simulated S-parameters of silicon image waveguide with length of $l_{si} = 20$ mm, width of $w_{si} = 125\mu$m, thickness of $h_{si} = 300\mu$m and taper length of $l_{taper} = 5.5$mm, with and without attached supporting block.

with a low-exposure dose. Figure 6.24 shows microscope images of the developed two-layer patterned photoresists with different exposure times of 75 seconds and 58.4 seconds. As can be seen, the shorter exposure time results in straighter sidewalls.

As discussed above, achieving straight vertical walls with thick photo resist is difficult. Another method is to create a thinner photoresist layer, but to also improve the selectivity of the mask by hardening the photoresist with post baking after development. A post-development bake (or "hard bake") of the photoresist pattern is a common method for stabilizing a printed pattern so that it will withstand the harsh environments of etching. This final bake step removes residual solvent, water, and gasses and improves adhesion of the photoresist to the substrate and its resistance to RIE etches. Post baking increased the selectivity of the photo resist to around 100.

The photoresist was spun to a thickness of approximately 11 um, then cooked at 110 for 90 seconds. After more than 3 hours delay for rehydration, the coated photo resist was exposed to UV light for 29.2 seconds and developed in 4:1 diluted AZ 400 for 2:40 minutes. Then, it was baked for 5 minutes on a hot plate at 110°C. Figure 6.25 shows both profiles (measured by the Bruker profilometer) and microscope images of the developed patterned photoresists before and after the post bake (inset). As depicted in this figure, the profile pattern is a little distorted due to thermal reflow.

The ultimate purpose of the hard bake is full removal of the solvent. However, since the

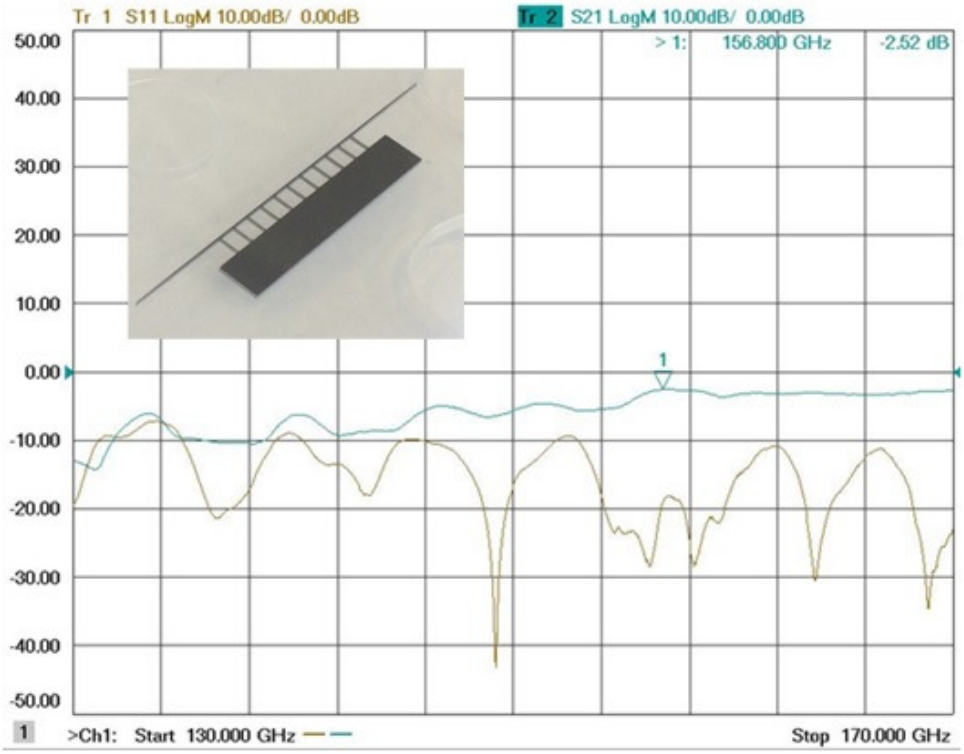

Figure 6.30: Measured S-parameters of fabricated silicon waveguide with no grating and graphene layer.

diffusion rate of the solvent is extremely low in solid photoresist, in order to achieve full removal for a thick photo resist the photoresist is baked at temperatures higher than the glass transition temperature of the resin. The resist is thus transformed from a glassy state into a soft rubbery state and starts flowing. In this semi-liquid state, the diffusion rate is significantly improved. Therefore, hard baking is usually done at or slightly above the glass transition temperature, so the flow of the resist degrades the resist profile significantly.

Thermal deformation of positive photoresist patterns during high temperature treatments is significantly reduced by deep UV curing of the resist surface to form a hard outer shell. In this method, the outer layer of the photoresist image is exposed to UV radiation in the range of 200-320 nm. The novolak resin in the photoresist is highly absorptive at this wavelength band. Therefore, the short wavelength UV lights penetrate only about 100 nm into the resist film. The thin cured layer allows hard baking of the photo resist at temperatures up to 200°C without any deformation. After deep UV curing, strippers cannot remove the resist and O_2 plasma etching is required to completely remove it.

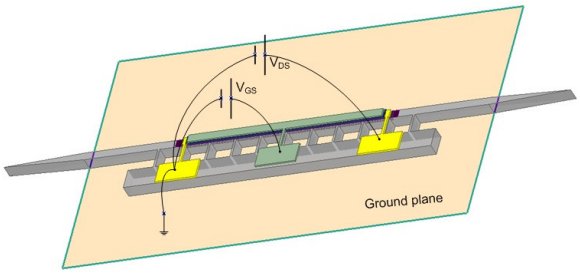

Figure 6.31: DC bias circuit.

The novolak-based AZ P4620 resist has a glass transition temperature of around 125°C. Since there was no access for this thesis to a deep-UV cure system, temperatures smaller than the glass- transition temperature were tested for hard baking. A 110°C and 5 min bake resulted in only a small distortion of the pattern profile and sidewalls, and the photoresist was hardened enough to withstand etching of 300 μm silicon.

It is better to shorten the delay between hard baking and etching so as to prevent rehydration of the resist. As mentioned in the beginning of the chapter, the Bosch process on an ICP-RIE system was used to fabricate rectangular dielectric waveguides. The etch rate depends on the amount of exposed silicon area on the wafer. A larger exposed area leads to a lower etch rate. Therefore, the samples were mounted on aluminium-oxide-coated wafers before being put inside the ICP-RIE system (for etching)(Fig. 6.27(a)).

The Bosch recipe parameters were modified to 90° sidewalls. Figure 6.26(a) shows an SEM image of the etched waveguide cross section etched by the standard Bosch silicon etching process in Oxford Plasmalab System 100 ICP380 DRIE at a temperature of T=0°C. As can be seen, the sidewall angle is less than 90° and the etch rate in the horizontal direction is not zero. Therefore, the passivation step time was increased from 5 seconds to 7 seconds while keeping all other parameters unchanged. Figure 6.26(b) shows a SEM image of the etched waveguide cross section fabricated by the above mentioned modification which resulted in perfectly vertical sidewalls. For both figures 6.26 (a) and (b), the one-layer AZ-P4620 masks were fabricated with the same recipe except that for Fig. 6.26(b) the mask was hard-baked after the development.

A resist strip is the final operation after the etching process is completed. The etched silicon waveguides were dipped in heated PG remover for one hour. If that did not remove the resist layer, it was etched using two minutes of oxygen plasma ashing at 180 degrees. Figure 6.27(b) shows the image of the fabricated sample. The next step is to connect the biasing voltage and conduct measurements.

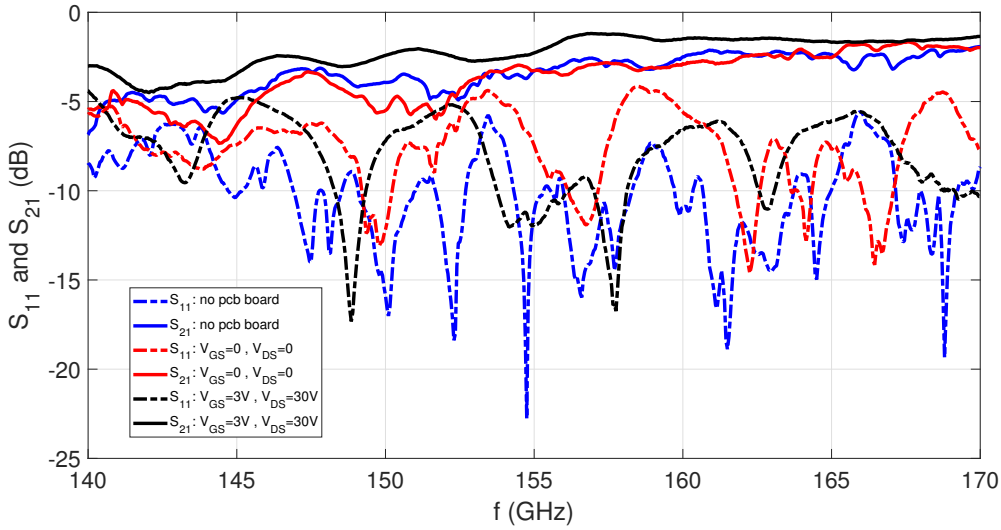

Figure 6.32: Measured S-parameters of fabricated graphene TWA over the frequency range of 140-170 GHz.

6.4 Measurement results

The fabricated structures were measured using a 1-50 GHz Agilent network analyzer connected to two OML millimeter-wave frequency extension modules, covering the frequency range of 110-170 GHz (see Fig. 6.28). The frequency extension modules were placed on micro positioning stages, with 4-axis degrees of freedom: x, y, z, and ϕ.

A metallic fixture, manufactured by Computer Numerical Control (CNC) machinery, was used to hold the silicon waveguide. The holder acts as the ground plane of this image waveguide. Therefore, it should be aligned precisely with respect to the metallic waveguide ground of the OML modules. To bring these structures into alignment, the micro positioning stages were used with the help of alignment holes and pins on the holder and waveguide flanges, respectively.

The ports of the OML modules are WR-06, standard metallic waveguides. The dielectric-to-metallic waveguide transition was realized by a tapered section of the silicon waveguide inserted into the metallic waveguide (see inset of Fig. 6.29). The tapered length was optimized to achieve good insertion loss. The silicon waveguide was supported from one side by means of a silicon supporting block that connected to the waveguide by narrow beams (Fig.6.19). Figure 6.29 shows the simulation results for a silicon waveguide with

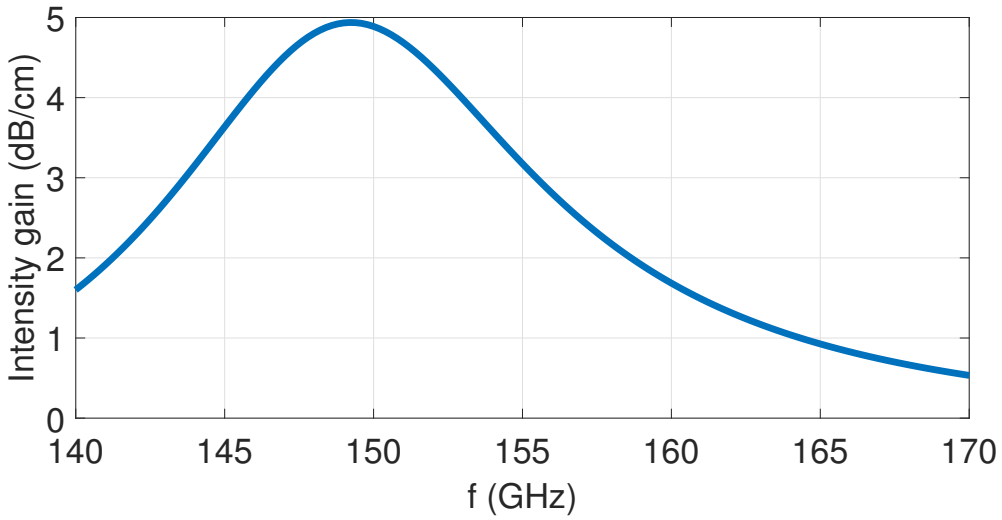

Figure 6.33: Calculated intensity gain versus frequency obtained from theoretical analysis for a TWA structure with the same dimensions as the fabricated sample with $E_f = 0.3$ eV and $V_d = 3 \times 10^5 m/s$.

and without a supporting block attached to it. Since the widths of the supporting beams are very small, $w_{beam} = 50\mu$m, negligible power transfers to the supporting structure. The measurement results for the fabricated silicon waveguide with no grating and graphene layer are shown in Fig. 6.30.

The next step is to perform measurement on the fabricated graphene TWA prototype of with $a = 125\mu$m, $b = 620\mu$m, $t_g = 540nm$, and $m_d = 0.28$. The DC bias circuit is shown in Fig. 6.31. The measurements results before attaching the DC biasing printed circuit board (PCB), after attaching the PCB but before applying the DC voltages, and after applying the DC voltages $V_{GS} = 3V$ and $V_{DS} = 30V$, are shown in Fig. 6.32. After applying the DC voltages, the S_{21} increased by a value between 0 to 2.7 dB at the frequency range of 140-170 GHz. The fabricated graphene TWA has a maximum gain of 2.7 dB/cm at 151.5 GHz. As predicted by the theoretical analysis (see Fig. 6.33), the maximum gain is obtained close to the cutoff frequency. Figure 1.33 shows the calculated intensity gain versus frequency obtained from theoretical analysis for a graphene TWA structure with the same dimensions as the fabricated sample, assuming $E_f = 0.3$ eV and $V_d = 3 \times 10^5$ m/s.

6.5 Conclusion

In this section, the procedure used to fabricate a novel integrated graphene-based travelling wave amplifier is described. This research uses newly developed silicon waveguide-based technology in the THz range of frequencies and integrates it with both nanofabrication and graphene technology. The fabrication procedure has more than ten major steps, including EBL, graphene transfer, dry etching, optical lithography and lift off. The challenges of each step are described and detailed solutions provided.

Two methods for fabricating the grating structure are proposed and tested based on already-established nanofabrication techniques. The details of the more reliable approach, which results in a uniform 1 cm long grating with nano scale dimensions, are given. Furthermore, two established methods for fabricating the graphene contacts are described one based on optical lithography and the other on a shadow mask. The first method consisting of optical lithography, deposition and lift-off, is used to fabricate the prototype structures. Because of the very weak bond of graphene to the substrate and metallic contacts, the application of ultrasound for cleaning and lift-off often damages the graphene and the contacts above it. On the other hand, removing the electron and photo resist residues on graphene is also difficult and affects the performance of the device. However, with the method utilized a precise alignment is achieved. Thus, an alternative method which avoids the problems with resist residues and difficult lift-off processes, is adopted. In this method, a shadow mask is used instead of patterned photo resist masks to fabricate the contacts on graphene. However, shadow mask alignment is more difficult than the alignment in photolithography and not as accurate. The alignment technique must be improved if this method is to be applied for future samples.

For fabrication of the 300 m thick silicon image waveguide, two methods are discussed: hard mask and thick photoresist mask. The advantages and disadvantages of each method are discussed and tested. Ultimately, a reliable fabrication process that yielded straight vertical walls with no lateral etching was developed.

The first fabricated prototype structure is measured using an Keysight network analyzer. Measuring the s-parameters of the waveguide before and after applying the DC bias voltages shows a maximum of 2.7 dB/cm gain for a 30 V/cm electric field at 151.5 GHz. Here, for the first time, measurements have confirmed that graphene can be used for travelling wave amplification. Although the amount of gain measured for this first prototype structure is small, this work establishes a clear beginning. Room for improvement remains, and will be discussed under future work (Section 7.1).

Chapter 7

Conclusion

In summary, a novel solid-state TWA using graphene as a conducting layer is proposed, thoroughly studied, successfully fabricated, and characterized in this thesis. Both theoretical and measurement results show that graphene is a good candidate for solid-state mm-wave and THz TWAs. The proposed graphene TWA is suitable for integration in future monolithic integrated THz circuits.

In this thesis, for the first time, travelling wave amplification in graphene was explored by developing two different models to define the conductivity for drifting charge carriers in graphene. In the first approach, a quantum mechanical model is developed to obtain the frequency and wave number dependent conductivity of graphene with drifting charge carriers under a non-equilibrium condition (Chapter 3). The second model used is a classical hydrodynamic model (Chapter 4) derived with a relativistic fluid approach in which the electrons in graphene are modelled as a 2D Fermi liquid. Based on this hydrodynamic model, the induced current is calculated for harmonic perturbation of both stationary and uniformly moving charged carriers, and the linear conductivity is obtained.

The conductivity relations obtained from both methods show that, for a slow electromagnetic wave with a phase velocity smaller than the drift velocity of the carriers, graphene changes from a lossy medium to a gain medium that converts power from the DC source to the electromagnetic field. Although the two methods are quite different, one being more classical and the other more quantum mechanical, the behaviour of the conductivity functions with respect to the frequency and wavenumber are remarkably similar.

In Chapter 5, grating structures on silicon slab and silicon rod waveguides are designed as slow wave structures for the proposed TWA. The Floquet mode solution of the first-order space harmonic(satisfying the travelling wave amplification requirement, $V_{ph} < V_d$),

is presented. Coupled wave analysis is used to obtain the interaction impedance and the overall gain of the graphene TWA. The estimation of an attainable gain for an optimized slow waveguide under reasonable bias is 10.5 dB/cm at 1 THz.

To simplify and speed up the fabrication process, the prototype structure is fabricated for a frequency range of 110-170 GHz. Therefore, a rod silicon waveguide with a thin grating layer on top is designed at a frequency of 150 GHz. A new approximate theoretical method is developed for analyzing the hybrid space-harmonics in gratings on top of rectangular dielectric waveguides. This method gives an explicit expression for the interaction impedance of slow wave grating structures, which is then used to design the waveguide and the grating. To verify the proposed approximation approach, the results obtained with this method are compared with simulation results obtained from FEM-based ANSYS electronics software.

The fabrication of the prototype structure consisted of fabricating three integrated main structures: the grating, the graphene layer attached to DC bias contacts, and the silicon waveguide. For each of these devices, reliable fabrication recipes are developed and combined to create the first graphene TWA integrated in a mm-wave silicon waveguide.

The first fabricated sample is measured using a Keysight network analyzer. The measurements show a maximum gain of $\sim$2.7 dB/cm for a 30 V/cm electric field at 151.5 GHz and thus, both theoretical and experimental results confirm that the graphene layer can be used for travelling wave amplification.

Future stages of this research are presented in the next section.

7.1 Future work

1) Non-linear analysis of large signal interactions with drifting plasma wave in graphene

In the current work, only the linear response of graphene was studied. The non-linear responses of graphene can be obtained by considering higher order terms in hydrodynamic equations. In such a method, the effect of the DC current on the non-linear conductivity of graphene could be explored.

2) Combining numerical methods with the proposed Fourier mode analysis to achieve more accurate estimation of parameters such as interaction impedance and gain.

In Chapter 5, an approximate analytical method was proposed to calculate the coupling factor between the drifting space charge wave in graphene and first-order space harmonic of the slow-wave grating structure. Based on the Fourier solution approach, a recursive formula was obtained in which the first-order space harmonic of the grating is determined in terms of the zeroth order harmonic. For thin gratings, the corresponding mode of the structure with no grating is a good approximation for the zeroth order harmonic. Therefore, in the proposed method, a good estimation of the waveguide mode will significantly improve the accuracy of the solution for the first-order space harmonic. The approximate results are shown to be in very good agreement with the simulation results for the slab waveguide for which an accurate analytical modal solution is available (Fig. 5.3). However, for rectangular waveguides, where there is no analytical solution, there is a discrepancy. This is especially true near cutoff points where the estimation of the modes obtained from the improved Marcatili approach have the lowest accuracy (Fig. 5.24).

Therefore, to obtain more accurate results, rigorous numerical methods should be used to obtain the field of a rectangular waveguide with no grating and then this result could be used in the proposed method to accurately estimate the field of the first-order space harmonic of the grating.

In this way the lengthy computation time required to analyze long gratings ($\sim 1-3\lambda$) with very fine feature size ($1/10000\lambda$) could still be avoided, and much more accurate results could be achieved.

3) Increase the graphene maximum achievable charge density and drift velocity

The maximum achievable value of the Fermi energy level is limited by the breakdown field strength of the gate dielectric. For example, for SiO_2 the dielectric strength is around 10^7 V/cm [**?**] and thus the maximum Fermi energy level value that can be achieved is around 300 meV (Fig. 2.4). However, with very specific dielectric materials such as ion-gel [142] and solid polymer electrolyte [143], it is possible to achieve Fermi energy levels as high as 1-2 eV. Figure 5.5 shows that increasing the Fermi level will increase the gain significantly.

Another important parameter that determines the maximum achievable gain is the drift velocity (see Fig. 5.6). The mobility, and thus the drift velocity, of graphene is very sensitive to the density of defects. Therefore, applying a better fabrication method for graphene will result in higher gain.

4) Improving the measurement setup to perform more accurate measurements

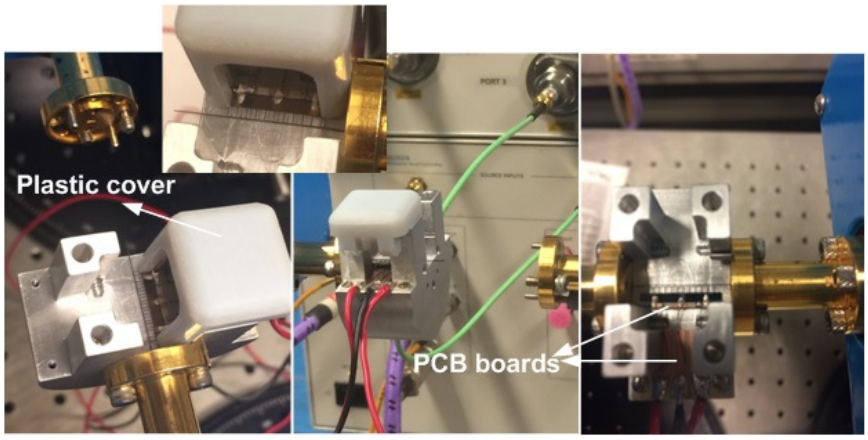

Figure 7.1: New metallic holder with 3D printed plastic cover.

After attaching the PCB, the sample should be fixed on the holder; otherwise, it will not sit flat on the ground surface. In the setup used to obtain the measurement results in this thesis, the sample was held in place by needle-sharp tweezers. This was not efficient as the sample moved after each measurement and had to be realigned until the maximum S_{21} value was obtained.

Therefore, a new metallic holder with a 3D printed plastic cover was manufactured (see Fig. 7.1). With this setup, the waveguide can be aligned once and stay fixed in place with the help of the plastic cover, while the DC biasing voltages are swept during measurements.

5) Fabricating a graphene-based structure for a higher range of frequencies

The proposed graphene-based TWA was demonstrated up to 170 GHz. The design of the structure should be refined to perform at higher frequencies.

6) Fabricating a THz beam amplifier with planar 2D structure

Future work could explore other types of graphene TWAs (see Fig. 7.2). In this configuration, the graphene sheet is placed on top of a periodic grating structure. The slow wave in the periodic grating is excited by the graphene SPP wave. The slow wave is amplified and fed to the grating antenna through a tapered grating. Fabricating such a structure will be easier than the architecture proposed in this thesis.

In Chapter 2, it was shown that the propagation constant of the SPP waves can be as large as 50 times the free space wavenumber (see Fig. 2.7). However, the propagation constant of the slow wave in the grating structure of the TWA is significantly larger than the propagation constant of the SPP wave in graphene. Therefore, a coupling structure

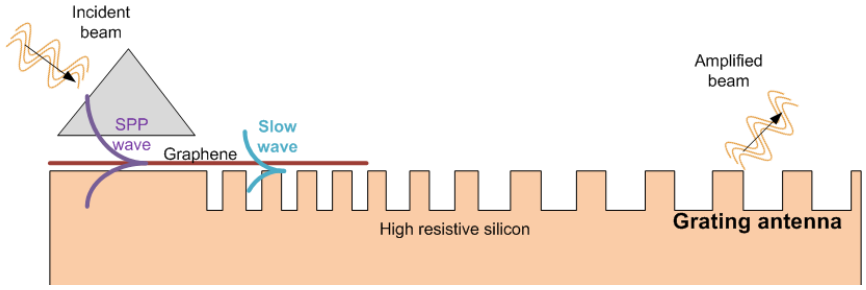

Figure 7.2: Proposed alternative graphene TWA.

should be designed to gradually match the SPP wave to the slow wave of the grating. The amplification should be large enough to compensate for the coupling loss. The development of such a structure will allow for the amplification of THz beams for a wide range of applications, such as THz spectroscopy and imaging applications.

APPENDICES

Appendix A

Tight-binding approach

In a periodic lattice structure the wave function of electrons should satisfy Blochs theorem

$$T_{\mathbf{a_i}}\Psi = e^{i\mathbf{k}.\mathbf{a_i}}\Psi \tag{A.1}$$

where $T_{\mathbf{a_i}}$ is a is the translation operator along the lattice vector $\mathbf{a_i}$ (see Fig. 2.1). The wave function is commonly defined as a linear combination of plane waves. In this case, we cannot easily relate the wavefunction to the atomic orbitals. Also the scale of computation is large since we have to use the large number of plane waves to reach desired accuracy. Another wave function form which is used in the tight binding method is based on the atomic orbitals in the unit cell [77]. Therefore, the tight binding Bloch function is defined as [77]

$$\Phi_j\left(\mathbf{k},\mathbf{r}\right) = \frac{1}{\sqrt{N}}\sum_{\mathbf{R}}^{N} e^{i\mathbf{k}.\mathbf{R}}\phi_j\left(\mathbf{r}-\mathbf{R}\right) \quad (j=1,...,n), \tag{A.2}$$

where $\mathbf{R}$ is the position of the atoms in the lattice, ϕ_j is the jth atomic orbital in the unit cell and N is the total number of unit cells. Therefore, we just have n Bloch functions (n denotes the number of atomic orbitals in the unit cell). The eigenfunctions are then determined as the linear combination of Bloch functions [77]:

$$\Psi_j\left(\mathbf{k},\mathbf{r}\right) = \sum_{j'=1}^{n} C_{jj'}\left(\mathbf{k}\right)\Phi_{j'}\left(\mathbf{k},\mathbf{r}\right), \tag{A.3}$$

and the energy eigenvalues are given as [77]

$$E_i(\mathbf{k}) = \frac{\int \Psi_i^* H \Psi_i d\mathbf{r}}{\int \Psi_i^* \Psi_i d\mathbf{r}} = \frac{\sum_{j,j'=1}^{n} H_{jj'}(\mathbf{k}) C_{ij}^* C_{ij'}}{\sum_{j,j'=1}^{n} S_{jj'}(\mathbf{k}) C_{ij}^* C_{ij'}}, \tag{A.4}$$

where H is the Hamiltonian of the system. By setting a partial derivative of E_i related to C_{ij}^* equal to zero, in order to minimize E_i, we obtain the following equation [77]:

$$HC_i = E_i(\mathbf{k}) SC_i, \quad C_i = \begin{pmatrix} C_{i1} \\ \vdots \\ C_{in} \end{pmatrix}, \tag{A.5}$$

where the elements of matrices H and S, known respectively as the transfer integral matrices and overlap integral matrices, are determined as follow [77]:

$$H_{jj'}(\mathbf{k}) = \langle \Phi_j | H | \Phi_{j'} \rangle \tag{A.6}$$

$$S_{jj'}(\mathbf{k}) = \langle \Phi_j \mid \Phi_{j'} \rangle \tag{A.7}$$

The transfer and the overlap matrix elements are often considered as parameters, and their values are determined so that the calculated band structure of the solid matches the one obtained either experimentally or from first principles calculations. It is deduced from A.5 that in order to have a nontrivial solution the following condition should be satisfied:

$$\det[H - E_i(\mathbf{k}) S] = 0 \tag{A.8}$$

This equation is called the secular equation. By solving the secular equation for the given $\mathbf{k}$, the n eigenvalues of E_i are obtained.

A.1 Electronic structure of graphene

Carbon atoms have four valence electrons, which occupy 2s, 2px, 2py, and 2pz orbitals. In graphene the 2s orbital and two 2p orbitals are mixed with each other, forming three σ bonds. These bonds are completely filled, thus forming a deep valance band. The unaffected p orbital, which is perpendicular to the planer structure, leads to the formation of a half filled π band. The π energy bands are covalent bands that play the most significant

role in the solid state properties of graphene. Therefore, we have two Bloch functions, constructed from the atomic orbitals of two carbon atoms A and B in the unit cell:

$$\Phi_j(\mathbf{r}) = \sum_{\mathbf{R}_\alpha} e^{i\mathbf{k}.\mathbf{R}_\alpha} \phi_j(\mathbf{r} - \mathbf{R}_\alpha), \quad (\alpha = A, B) \tag{A.9}$$

where the summation is taken over the position of the A or B atoms in the structure. The Hamiltonian matrix is obtained by substituting A.9 in A.6. For diagonal elements we have [77]:

$$\begin{aligned} H_{AA}(\mathbf{r}) = H_{BB}(\mathbf{r}) &= \tfrac{1}{N} \sum_{\mathbf{R}} \sum_{\mathbf{R}'} e^{i\mathbf{k}(\mathbf{R}-\mathbf{R}')} \langle \phi(\mathbf{r} - \mathbf{R}') | H | \phi(\mathbf{r} - \mathbf{R}) \rangle \\ &= \tfrac{1}{N} \sum_{\mathbf{R}=\mathbf{R}'} \varepsilon_{2p} + \tfrac{1}{N} \sum_{\mathbf{R}=\mathbf{R}'\pm\mathbf{a_i}} e^{\pm i\mathbf{k}.\mathbf{a_i}} \langle \phi(\mathbf{r} - \mathbf{R}') | H | \phi(\mathbf{r} - \mathbf{R}) \rangle \\ &\quad + (terms\, equal\, to\, or\, more\, dis\tan t\, than\, \mathbf{R} = \mathbf{R}' \pm 2\mathbf{a_i}) \\ &= \varepsilon_{2p} + (terms\, equal\, to\, or\, more\, dis\tan t\, than\, \mathbf{R} = \mathbf{R}' \pm \mathbf{a_i}) \end{aligned} \tag{A.10}$$

where ϵ_{2p} is the orbital energy of the 2p level. Also for off diagonal elements $H_{AB} = H_{BA}^*$ we consider only the contribution of the nearest neighbour A and B atoms.

$$H_{AB} = H_{BA}^* = t(e^{j\mathbf{k}.\delta_1} + e^{j\mathbf{k}.\delta_2} + e^{j\mathbf{k}.\delta_3}) = tf(\mathbf{k}) \tag{A.11}$$

where $t = \langle \phi_A(r - R) | H | \phi_B(r - R \pm a) \rangle$ is the transfer integral, also known as the nearest neighbor-hopping energy. Similarly the overlap matrix S_{ij} can be calculated (eq. A.7). Assuming a normalized atomic wavefunction, we have $S_{AA} = S_{BB} = 1$ and $S_{AB} = S_{BA}^* = sf(\mathbf{k})$, where $s = \langle \phi_A(\mathbf{r} - \mathbf{R}) \mid \phi_B(\mathbf{r} - \mathbf{R} \pm \delta_\mathbf{i}) \rangle$ is the overlap integral between the nearest A and B atoms. Therefore, the Hamiltonian, H, and overlap, S, matrices are

$$H = \begin{pmatrix} \varepsilon_{2p} & tf(\mathbf{k}) \\ tf^*(\mathbf{k}) & \varepsilon_{2p} \end{pmatrix} \tag{A.12}$$

and

$$S = \begin{pmatrix} 1 & sf(\mathbf{k}) \\ sf^*(\mathbf{k}) & 1 \end{pmatrix} \tag{A.13}$$

Substituting the above defined matrices in the secular equation (eq. A.8) and solving it for each $\mathbf{k}$ the two eigenvalues $E(\mathbf{k})$ are obtained as a function of $\mathbf{k}$ [77]:

$$E(\mathbf{k}) = \frac{\varepsilon_{2p} \pm t\,|f(\mathbf{k})|}{1 \pm s\,|f(\mathbf{k})|} \tag{A.14}$$

where $f(\mathbf{k})$ is defined in eq. A.11 The + sign gives the upper anti-bonding π^* band, and the sign gives the lower bonding π band. These two bands touch at six Dirac points. By ignoring the overlap integral between adjacent atoms orbitals and considering the next nearest neighbour-hopping energy, t', the energy bands are obtained as follows [3]:

$$\begin{aligned} E_{\pm}(\mathbf{k}) &= \pm t\sqrt{3+g(\mathbf{k})} - t'g(\mathbf{k}) \\ g(\mathbf{k}) &= 2\cos\left(\sqrt{3}k_y a\right) + 4\cos\left(\tfrac{\sqrt{3}}{2}k_y a\right)\cos\left(\tfrac{3}{2}k_x a\right) \end{aligned} \tag{A.15}$$

in which $a = |\mathbf{a_i}|$.

Appendix B

Coupled-mode analysis of Floquet eigenmodes

The wave equation in the presence of an external current is

$$\nabla \times \nabla \times \mathbf{E} - \omega^2 \mu \epsilon \mathbf{E} = -j\omega\mu\mathbf{J} \tag{B.1}$$

Assume an external current distribution:

$$\mathbf{J} = \mathbf{J_e}(x, y)e^{-j\beta z} \tag{B.2}$$

which will excite eigenmodes of the periodic waveguide. For a particular Floquet mode E_A:

$$\mathbf{E_A}) = \Sigma_m \mathbf{E_{A_m}}(x, y)e^{-j\beta_m z} \tag{B.3}$$

$$\beta_m = \beta_0 + m\frac{2\pi}{d} \quad m = 0, \pm 1, \pm 2, \cdots \tag{B.4}$$

if for its first-order space harmonic $\beta_1 \simeq \beta$, then this mode will be predominantly excited and its amplitude will grow slowly. Therefore, the solution of equation B.1 can be written as:

$$\mathbf{E} = K(z)\mathbf{E_A} \tag{B.5}$$

where $K(z)$ is a slowly varying function.By replacing $\mathbf{E}$ in eq. B.1 with $\mathbf{E}$ from eq. B.5, after some mathematical manipulation we get:

$$K''(z)\left(\mathbf{E_A} - E_{Az}\hat{z}\right) + K'(z)\left(\frac{\partial}{\partial z}\mathbf{E_A} - \hat{z}\times(\nabla\times\mathbf{E_A}) - \hat{z}\nabla\cdot\mathbf{E_A}\right) = j\omega\mu\mathbf{J} \tag{B.6}$$

The z component of the first term is zero. Multiplying eq. B.5 by $\mathbf{E_A^*}$ and integrating over all space yields:

$$K'(z)\int_0^d dz\int\int_{-\infty}^{\infty} dxdy\mathbf{E_A^*}\cdot\mathbf{L_A} = j\omega\mu\int_0^d dz\int\int_{-\infty}^{\infty} dxdy\mathbf{E_A^*}\cdot\mathbf{J} \tag{B.7}$$

where

$$\mathbf{L_A} = \frac{\partial}{\partial z}\mathbf{E_A} - \hat{z}\times(\nabla\times\mathbf{E_A}) - \hat{z}\nabla\cdot\mathbf{E_A} \tag{B.8}$$

In deriving eq. B.7, $K'(z)$ variation over one period of d is assumed to be negligible. Therefore, it is pulled out of the integral. We assume that the Floquet mode $\mathbf{E_A}$ and the current $\mathbf{J}$ are nearly phase matched through the first-order space harmonic.

$$\Delta\beta_1 = \beta - \beta_0 - \frac{2\pi}{d} \approx 0 \tag{B.9}$$

Therefore, we can assume that the function $e^{\mp j\Delta\beta_1 z}$ is nearly constant over the period of d. By this assumption, we can rewrite eq. B.7 as follows [73]:

$$K'(z)\int_0^d dz\int\int_{-\infty}^{\infty} dxdy\mathbf{E_A^*}\cdot\mathbf{L_A} = j\omega\mu e^{-j\Delta\beta_1 z}\int_0^d dz e^{j\Delta\beta_1 z}\int\int_{-\infty}^{\infty} dxdy\mathbf{E_A^*}\cdot\mathbf{J} \tag{B.10}$$

For the left hand integral of eq. B.10, after some mathematical interpolation and substituting the magnetic field from the Maxwell's equation, we get:

$$\int_0^d \int \int_{-\infty}^{\infty} dzdxdy \mathbf{E}_\mathbf{A}^* \cdot \mathbf{L}_\mathbf{A} = -j\omega\mu \int_0^d \int \int_{-\infty}^{\infty} dzdxdy\hat{z} \cdot (\mathbf{E}_\mathbf{A}^* \times \mathbf{H}_\mathbf{A} + \mathbf{E}_\mathbf{A} \times \mathbf{H}_\mathbf{A}^*)$$
$$= -4j\omega\mu d P_A \tag{B.11}$$

Here P_A is the total average z-directed power carried by mode E_A. For very thin gratings, we can assume that most of the power is carried by the fundamental harmonic and $P_A \simeq P_{A0}$.

The Floquet expansion of the $\mathbf{E_A}$ mode (eq. B.3) is substituted in the right hand integral of eq. B.10 to perform the z integration. Only the term with the first-order space harmonic does not vanish in the z integration. Therefore, eq. B.10 yields [73]:

$$K'(z) = -\frac{e^{-j\Delta\beta_1 z}}{4P_{A0}} \int_{-\infty}^{\infty} \int_{-\infty}^{\infty} dxdy \mathbf{E_{A_1}}^*(x,y) \cdot \mathbf{J}_e(x,y) \tag{B.12}$$

$$K(z) = -j\frac{e^{-j\Delta\beta_1 z}}{4P_{A0}\Delta\beta_1} \int_{-\infty}^{\infty} \int_{-\infty}^{\infty} dxdy \mathbf{E}_{\mathbf{A_1}}^*(x,y) \cdot \mathbf{J_e}(x,y) \tag{B.13}$$

Substituting $K(z)$ in eq. B.5 for the particular synchronous space harmonic field, $E_1(x,z)$, we find

$$E_1(x,z) = \frac{-j}{4P_{A0}\Delta\beta_1} \mathbf{E_{A_1}}(x,y) e^{-j\beta z} \int_{-\infty}^{\infty} \int_{-\infty}^{\infty} dxdy \mathbf{E_{A_1}}^*(x,y) \cdot \mathbf{J_e}(x,y) \tag{B.14}$$

Appendix C

Marcatili's method

The electromagnetic waves propagating along a straight waveguide are classified into TE, TM or hybrid modes according to the presence or absence of the longitudinal field components E_z and H_z components. The dielectric rectangular waveguide can only supports hybrid modes with both E_z and H_z present. We consider a monochromatic wave with angular frequency ω, propagating in the z direction with a propagation constant β. In an homogeneous region j, with the relative dielectric constant of $\epsilon_r = \epsilon_{rj} = cons$, it is possible to describe the full electromagnetic fields in terms of the longitudinal field components in each region j:

$$E_x = \frac{-j\beta_z}{K_j^2}\frac{\partial E_z}{\partial x} - \frac{j\omega\mu}{K_j^2}\frac{\partial H_z}{\partial y} \tag{C.1a}$$

$$E_y = \frac{-j\beta_z}{K_j^2}\frac{\partial E_z}{\partial y} + \frac{j\omega\mu}{K_j^2}\frac{\partial H_z}{\partial x} \tag{C.1b}$$

$$H_x = \frac{j\omega\epsilon}{K_j^2}\frac{\partial E_z}{\partial y} - \frac{j\beta_z}{K_j^2}\frac{\partial H_z}{\partial x} \tag{C.1c}$$

$$H_y = \frac{-j\omega\epsilon}{K_j^2}\frac{\partial E_z}{\partial x} - \frac{j\beta_z}{K_j^2}\frac{\partial H_z}{\partial y} \tag{C.1d}$$

Here, all components satisfy the reduced wave equation (here given only for E_z)

$$\nabla_t^2 E_z + K_j^2 E_z = 0 \tag{C.2}$$

where $K_j^2 = k_0^2 \epsilon_{rj} - \beta_z^2$ and ∇_t is the transverse Laplacian.

In Marcatili's method, the modes are divided in two families. In one family, where most of the electric field is polarized in the x-direction, they are designated as Ex_{nm} modes, and the other, where most of its electric field is in the y-direction, they are designated as Ey_{nm} modes. The subscripts n and m represent, respectively, the number of extrema that the field components for this mode have along the x and y directions. The dominant components of the Ex_{nm} modes are Ex, Ez, Hy, and Hz, with negligible Hx and Ey components. The dominant components of the Ey_{nm} modes are Ey, Ez, Hx, and Hz, with negligible Ex and Hy components.

Our analysis considers only the Ex_{11} mode, with the electric field predominantly polarized in the x-direction. This mode is a TM-like mode at the surface of the graphene layer. From symmetry, the same equations can be used for the TE-like mode with dominant electric field in the y-direction by exchanging the width and the height values of the waveguide. However, the coupling between the space charge density wave in graphene and the TE-like mode (Ey_{nm}) is not significant, since the z-directed plasma wave is modulated only by the z component of the field.

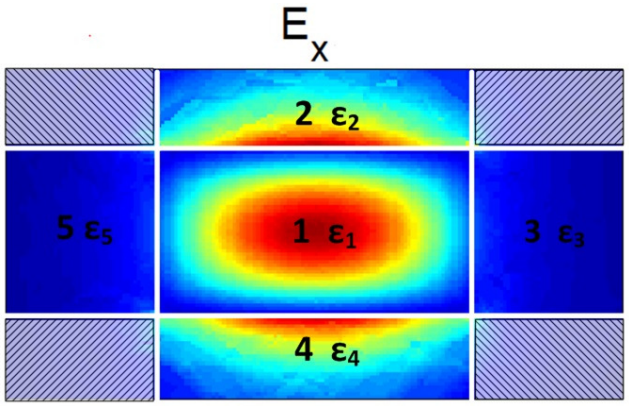

Figure C.1: Cross section of the waveguide. Regions $1-5$ along with the corner regions are indicated. The color plot represents the dominant electric field component E_x, of the fundamental TM-like mode.

In the Marcatili approach the behavior of the electromagnetic wave in the rectangular waveguide is described based on the separation of spatial variables in the core region. Furthermore, the effect of the corners is neglected since the field is small in these areas. The modal field then described as standing waves in the core of the waveguide and an exponentially decaying field outside the core (see Fig. C.1). We assume $\epsilon_1 = \epsilon_{Si}$ and $\epsilon_2 =$

$\epsilon_3 = \epsilon_4 = \epsilon_5 = \epsilon_{air}$. Hereafter, we use the symmetry conditions to reduce the calculation domain to regions 1,2 and 3. Therefore,the longitudinal components are expressed as:

$$e_{z0} = \begin{cases} A_2 e^{-\gamma_x(x-b/2)} \cos(k_y y) & x > b/2, -a/2 < y < a/2 \\ A_1 \sin(k_x x) \cos(k_y y) & -b/2 < x < b/2, -a/2 < y < a/2 \\ A_3 \sin(k_x x) e^{\gamma_y(y-a/2)} & -b/2 < x < b/2, a/2 < y \end{cases} \tag{C.3}$$

$$h_{z0} = \begin{cases} B_2 e^{-\gamma_x(x-b/2)} \sin(k_y y) & x > b/2, -a/2 < y < a/2 \\ B_1 \cos(k_x x) \sin(k_y y) & -b/2 < x < b/2, -a/2 < y < a/2 \\ B_3 \cos(k_x x) e^{\gamma_y(y-a/2)} & -b/2 < x < b/2, a/2 < y \end{cases} \tag{C.4}$$

The transversal electromagnetic field components are obtained from equations C.1 in which

$$K_j^2 = k_x^2 + k_y^2. \tag{C.5}$$

From the wave equation we have:

$$\gamma_x^2 = (\epsilon_{Si} - \epsilon_{air}) k_0^2 - k_x^2 \tag{C.6a}$$

$$\gamma_y^2 = (\epsilon_{Si} - \epsilon_{air}) k_0^2 - k_y^2. \tag{C.6b}$$

The E_z and H_z field components are defined such that the dominant electric field component Ex is described by a cosine function in both x and y directions.

The field proposed here is not an exact solution of Maxwell's equations. The proposed solution obeys Maxwell's equations in all regions individually. However, the approximation errors occur at the interfaces between the waveguide core and its cladding. At these interfaces, all boundary conditions cannot be satisfied at the same time, results in the discontinuity of some of the tangential components.

In a symmetric structure with homogeneous cladding around the core of the waveguide, there are eight equations from the electromagnetic boundary conditions (two interfaces, with four tangential field components). There are only eight free parameteres (Amplitudes of Ez and Hz components in regions $1-3$, k_x and k_y). Therefore, the system is overdetermined. As a result, no solution exactly obeys the electromagnetic boundary conditions at all interfaces simultaneously. In the following, we explain different possibilities for choosing the free parameters so as to obtain a low mismatch of the fields at the boundaries.

Applying the electromagnetic boundary conditions at the $1-2$ interface results in:

$$B_1 = \frac{\omega\epsilon_0\epsilon_{r1}k_y}{\beta_z k_x}A_1 \tag{C.7a}$$

$$A_2 = A_1 sin(k_x b/2) \tag{C.7b}$$

$$B_2 = B_1 cos(k_x b/2) \tag{C.7c}$$

$$tan(k_x b/2) = \frac{\epsilon_{r1}\gamma_x}{\epsilon_{r2}k_x} \tag{C.7d}$$

The dominant electric field component is orthogonal to these interfaces, so in an infinitely wide rectangle ($b \to \infty$) this mode will behave like a TM mode in a slab waveguide. The magnetic field component, H_x, is zero in regions 1, 2 and 4 as follows from equation C.1c. The last equation, C.7d, is the dispersion equation for a TM mode in a slab waveguide.

Applying the electromagnetic boundary conditions at the $1-3$ interface to which the dominant electric field is parallel results in:

$$B_1 = \frac{\beta_z k_y}{\omega\mu_0 k_x}A_1 \tag{C.8a}$$

$$A_3 = A_1 cos(k_y a/2) \tag{C.8b}$$

$$B_3 = B_1 sin(k_y a/2) \tag{C.8c}$$

$$tan(k_y a/2) = \frac{\gamma_y}{k_y} \tag{C.8d}$$

As follows from equation C.1b the electric field component E_y is zero in regions 1, 3 and 5. Equation C.8d is the same as the eigenvalue equation of a TE mode in a slab waveguide.

Obeying all electromagnetic boundary conditions at the 1-2 interface demands different amplitude coefficients than those obtained from the 1-3 interface boundary conditions. Therefore, there is no exact solution. In Appendix D, we explain the difference between Marcatili's approach and improved methods in choosing the free parameters and the boundary conditions to be satisfied and how the choice of improved methods results in a lower mismatch than Marcatili's approach [121].

In the Marcatili approach, one of the non-dominant transverse field components is set to zero. For a Ex_{nm} mode either H_x or E_y can be set to zero. The first case is called as Marcatili's $H_x = 0$ and the second one is called Marcatili's $E_y = 0$ method. The amplitudes

coefficients of E_z and H_z components for the Marcatili $H_x = 0$ method are obtained as follow:

$$B_1 = \frac{\omega\epsilon_0\epsilon_{r1}k_y}{\beta_z k_x}A_1 \tag{C.9a}$$

$$A_2 = A_1 sin(k_x b/2) \tag{C.9b}$$

$$B_2 = A_1\frac{\omega\epsilon_0\epsilon_{r2}k_y}{\beta_{z0}\gamma_x}sin(k_x b/2) \tag{C.9c}$$

$$A_3 = A_1\frac{\epsilon_{r1}k_y}{\epsilon_{r2}\gamma_y}sin(k_y a/2) \tag{C.9d}$$

$$B_3 = A_1\frac{\omega\epsilon_0\epsilon_{r1}k_y}{\beta_z k_x}sin(k_y a/2) \tag{C.9e}$$

$$\tan(k_x b/2) = \frac{\epsilon_{r1}\gamma_x}{\epsilon_{r2}k_x} \qquad H_y \textit{ continuous @ 1-2} \tag{C.9f}$$

$$\tan(k_y a/2) = \frac{\gamma_y}{k_x} \qquad E_x \textit{ continuous @ 1-3 } (\frac{k_x^2}{k_0^2\epsilon_{ri}} << 1) \tag{C.9g}$$

With this set of A_i and B_i coefficients, all electromagnetic boundary conditions at the 12 and 14 interface are satisfied. However, at the 13 and 15 interfaces, while the $H_x = 0$ and H_z are matched, the dominant transverse field component E_x and E_z are not matched.

Similarly, another approximate solution, Marcatili's $E_y = 0$, is obtained by setting

$E_y = 0$.

$$B_1 = A_1 \frac{\beta_z k_y}{\omega \mu k_x} \tag{C.10a}$$

$$A_2 = A_1 sin(k_x b/2) \tag{C.10b}$$

$$B_2 = A_1 \frac{\beta_z k_y}{\omega \mu \gamma_x} sin(k_x b/2) \tag{C.10c}$$

$$A_3 = A_1 \frac{k_y}{\gamma_y} sin(k_y a/2) \tag{C.10d}$$

$$B_3 = A_1 \frac{\beta_z k_y}{\omega \mu k_x} sin(k_y a/2) \tag{C.10e}$$

$$\tan(k_x b/2) = \frac{\epsilon_{r1} \gamma_x}{\epsilon_{r2} k_x} \qquad (\frac{k_y^2}{k_0^2} << 1) \tag{C.10f}$$

$$\tan(k_y a/2) = \frac{\gamma_y}{k_y} \tag{C.10g}$$

With these coefficients, $E_y = 0$ and E_z are matched, but H_z and H_y, the dominant magnetic field component, are not. Although the field amplitudes are different to the case where $H_x = 0$ in all regions, the eigenvalue equations are identical for both Marcatii's $H_x = 0$ and Marcatili's $E_y = 0$ methods.

The $\frac{k_x^2}{k_0^2 \epsilon_{ri}}$ value is negligible for low-index-contrast waveguides. However, this is not a good assumption for high-index-contrast waveguides, leads to a larger mismatch in the continuity of the dominant electric field components.

Appendix D

Improved Marcatili's method

In this appendix, we present an improvement of Marcatili method that gives a better description of fields in the rectangular waveguide. We have two options for improving the matching of the boundary conditions. In one option, the continuity of all boundary conditions at the interface **normal** to the dominant electric field component is satisfied; at the other interface only the dominant field components are forced to be continuous. In the other option, the continuity of all boundary conditions at the interface **parallel** to the dominant electric field component is satisfied; at the other interface only the dominant field components are forced to be continuous.

In the Marcatility $H_x = 0$ the continuity of tangential magnetic component H_x which is not a dominant magnetic field, is satisfied trivially at all interfaces. However as we discussed in Appendix C, the continuity of dominant electric field component is sacrificed. The more reasonable choice in choosing boundary condition is to demand the continuity of the dominant electric and magnetic fields at the $1-2$ and $1-3$ interface at the cost of the weak magnetic field component being not continuous across the $1-3$ interface. This method is called improved $H_x = 0$. With this modification, the A_i and B_i coefficients for this method are [121]:

$$B_1 = A_1 \frac{\omega \epsilon_0 \epsilon_{r1} k_y}{\beta_z k_x} \tag{D.1a}$$

$$A_2 = A_1 sin(k_x b/2) \tag{D.1b}$$

$$B_2 = A_1 \frac{\omega \epsilon_0 \epsilon_{r1} k_y}{\beta_z k_x} cos(k_x b/2) \tag{D.1c}$$

$$A_3 = A_1 \left(1 + \frac{k_0^2(\epsilon_{r1} - \epsilon_{r2})}{\beta_z^2}\right) cos(k_y a/2) \tag{D.1d}$$

$$B_3 = A_1 \frac{\omega \epsilon_0 \epsilon_{r1} k_y}{\beta_z k_x} sin(k_y a/2) \tag{D.1e}$$

$$\tag{D.1f}$$

Similarly for the Marcatili $E_y = 0$ method, the discontinuity of the dominant magnetic field is removed at the cost of the weak electric field component E_y being not continuous across the $1-2$ and $1-4$ interfaces. After applying all boundary conditions at the $1-3$ interface, and continuity of H_y and Ez at the $1-2$ interface, the amplitude coefficients of the electrical and magnetic field components are obtained as [121]:

$$B_1 = A_1 \frac{\beta_z k_y}{\omega \mu k_x} \tag{D.2a}$$

$$A_2 = A_1 sin(k_x b/2) \tag{D.2b}$$

$$B_2 = A_1 \frac{\beta_z k_y}{\omega \mu k_x} \left(1 + \frac{k_0^2(\epsilon_{r1} - \epsilon_{r2})}{\beta_z^2}\right) cos(k_x b/2) \tag{D.2c}$$

$$A_3 = A_1 cos(k_y a/2) \tag{D.2d}$$

$$B_3 = A_1 \frac{\beta_z k_y}{\omega \mu k_x} sin(k_y a/2) \tag{D.2e}$$

$$\tag{D.2f}$$

References

[1] T Otsuji and M Shur, "Terahertz plasmonics: Good results and great expectations," *Microwave Magazine, IEEE*, vol. 15, no. 7, pp. 43–50, 2014.

[2] Carter M Armstrong, "The truth about terahertz," *IEEE SPECTRUM*, vol. 49, no. 9, pp. 36–41, 2012.

[3] AH Castro Neto, F Guinea, NMR Peres, Kostya S Novoselov, and Andre K Geim, "The electronic properties of graphene," *Reviews of modern physics*, vol. 81, no. 1, pp. 109, 2009.

[4] Craig Kulesa, "Terahertz spectroscopy for astronomy: From comets to cosmology," *Terahertz Science and Technology, IEEE Transactions on*, vol. 1, no. 1, pp. 232–240, 2011.

[5] Mattias Beck, Daniel Hofstetter, Thierry Aellen, Jérôme Faist, Ursula Oesterle, Marc Ilegems, Emilio Gini, and Hans Melchior, "Continuous wave operation of a mid-infrared semiconductor laser at room temperature," *Science*, vol. 295, no. 5553, pp. 301–305, 2002.

[6] Eric R Mueller, "Optically-pumped thz laser technology," *Coherent-DEOS product Note*, pp. 1–10, 2001.

[7] Jam Farhoomand and Herbert M Pickett, "Stable 1.25 watts cw far infrared laser radiation at the 119 μm methanol line," *International journal of infrared and millimeter waves*, vol. 8, no. 5, pp. 441–447, 1987.

[8] Benjamin S Williams, "Terahertz quantum-cascade lasers," *Nature photonics*, vol. 1, no. 9, pp. 517, 2007.

[9] S Fathololoumi, E Dupont, CWI Chan, ZR Wasilewski, SR Laframboise, D Ban, A Mátyás, C Jirauschek, Q Hu, and HC Liu, "Terahertz quantum cascade lasers operating up to 200 k with optimized oscillator strength and improved injection tunneling," *Optics express*, vol. 20, no. 4, pp. 3866–3876, 2012.

[10] Alain Maestrini, Imran Mehdi, J Ward, R Lin, B Thomas, C Lee, J Gill, G Chattopadhyay, E Schlecht, and P Siegel, *A 2.5-2.7 THz room temperature electronic source*, Pasadena, CA: Jet Propulsion Laboratory, National Aeronautics and Space Administration, 2011.

[11] TW Crowe, JL Hesler, C Pouzou, WL Bishop, and GS Schoenthal, "Development and characterization of a 2.7 thz lo source," in *Proc. 22nd Int. Symp. on Space Terahertz Technol*, 2011, pp. 26–28.

[12] Qun Xiao, Jeffrey L Hesler, Thomas W Crowe, Robert M Weikle, Yiwei Duan, Bascom S Deaver, et al., "High-efficiency heterostructure-barrier-varactor frequency triplers using aln substrates," in *Microwave Symposium Digest, 2005 IEEE MTT-S International*. IEEE, 2005, pp. 4–pp.

[13] Xiaobing Mei, Wayne Yoshida, Mike Lange, Jane Lee, Joe Zhou, Po-Hsin Liu, Kevin Leong, Alex Zamora, Jose Padilla, Stephen Sarkozy, et al., "First demonstration of amplification at 1 thz using 25-nm inp high electron mobility transistor process," *Electron Device Letters, IEEE*, vol. 36, no. 4, pp. 327–329, 2015.

[14] Nezih Tolga Yardimci, Semih Cakmakyapan, Soroosh Hemmati, and Mona Jarrahi, "A high-power broadband terahertz source enabled by three-dimensional light confinement in a plasmonic nanocavity," *Scientific reports*, vol. 7, no. 1, pp. 4166, 2017.

[15] Sergey Lepeshov, Andrei Gorodetsky, Alexander Krasnok, Nikita Toropov, Tigran A Vartanyan, Pavel Belov, Andrea Alú, and Edik U Rafailov, "Boosting terahertz photoconductive antenna performance with optimised plasmonic nanostructures," *Scientific reports*, vol. 8, 2018.

[16] Mona Jarrahi, "Advanced photoconductive terahertz optoelectronics based on nano-antennas and nano-plasmonic light concentrators," *IEEE Transactions on Terahertz Science and Technology*, vol. 5, no. 3, pp. 391–397, 2015.

[17] Nezih T Yardimci, Shang-Hua Yang, Christopher W Berry, and Mona Jarrahi, "High-power terahertz generation using large-area plasmonic photoconductive emitters," *IEEE Transactions on Terahertz Science and Technology*, vol. 5, no. 2, pp. 223–229, 2015.

[18] L Solymar and EA Ash, "Some travelling-wave interactions in semiconductors theory and design considerations," *International Journal of Electronics*, vol. 20, no. 2, pp. 127–148, 1966.

[19] ME Hines, "Theory of space-harmonic traveling-wave interactions in semiconductors," *Electron Devices, IEEE Transactions on*, vol. 16, no. 1, pp. 88–97, 1969.

[20] Masao Sumi, "Travelling-wave amplification by drifting carriers in semiconductors," *Applied Physics Letters*, vol. 9, no. 6, pp. 251–253, 1966.

[21] Masao Sumi and Toshimasa Suzuki, "Evidence for directional coupling between semiconductor carriers and slow circuit waves," *Applied Physics Letters*, vol. 13, no. 9, pp. 326–327, 1968.

[22] Abdul Manaf Hashim, Seiya Kasai, Tamotsu Hashizume, and Hideki Hasegawa, "Integration of interdigital-gated plasma wave device for proximity communication system application," *Microelectronics Journal*, vol. 38, no. 12, pp. 1263–1267, 2007.

[23] Patrik Pousi, Dmitri Lioubtchenko, Sergey Dudorov, and Antti V Räisänen, "Dielectric rod waveguide travelling wave amplifier based on algaas/gaas heterostructure," in *Microwave Conference, 2008. EuMC 2008. 38th European*. IEEE, 2008, pp. 1082–1085.

[24] John Robinson Pierce, *Travelling-wave tubes*, Van Nostrand; Macmillan, 1950.

[25] Masao Sumi and Toshimasa Suzuki, "Evidence for directional coupling between semiconductor carriers and slow circuit waves," *Applied Physics Letters*, vol. 13, no. 9, pp. 326–327, 1968.

[26] JC Freeman, VL Newhouse, and RL Gunshor, "Interactions between slow circuit waves and drifting carriers in insb and ge at 4.2 k," *Applied Physics Letters*, vol. 22, no. 12, pp. 641–643, 1973.

[27] Avraham Gover and Amnon Yariv, "Monolithic solid-state traveling-wave amplifier," *Journal of Applied Physics*, vol. 45, no. 6, pp. 2596–2600, 1974.

[28] A Gover and A Yariv, "Intraband radiative transitions and plasma electromagnetic-wave coupling in periodic semiconductor structure," *Journal of Applied Physics*, vol. 46, no. 9, pp. 3946–3950, 1975.

[29] VE Lyubchenko, "Travelling wave amplification in gaas image waveguide at v-band," *Electronics Letters*, vol. 30, no. 11, pp. 869–870, 1994.

[30] Philip Richard Wallace, "The band theory of graphite," *Physical Review*, vol. 71, no. 9, pp. 622, 1947.

[31] SV Morozov, KS Novoselov, MI Katsnelson, F Schedin, DC Elias, JA Jaszczak, and AK Geim, "Giant intrinsic carrier mobilities in graphene and its bilayer," *Physical review letters*, vol. 100, no. 1, pp. 016602, 2008.

[32] Jian-Hao Chen, Chaun Jang, Shudong Xiao, Masa Ishigami, and Michael S Fuhrer, "Intrinsic and extrinsic performance limits of graphene devices on sio2," *Nature nanotechnology*, vol. 3, no. 4, pp. 206–209, 2008.

[33] Kirill I Bolotin, KJ Sikes, Zd Jiang, M Klima, G Fudenberg, J Hone, P Kim, and HL Stormer, "Ultrahigh electron mobility in suspended graphene," *Solid State Communications*, vol. 146, no. 9, pp. 351–355, 2008.

[34] Michael S Fuhrer, Chun Ning Lau, and Allan H MacDonald, "Graphene: materially better carbon," *MRS bulletin*, vol. 35, no. 4, pp. 289–295, 2010.

[35] Alexander A Balandin, Suchismita Ghosh, Wenzhong Bao, Irene Calizo, Desalegne Teweldebrhan, Feng Miao, and Chun Ning Lau, "Superior thermal conductivity of single-layer graphene," *Nano letters*, vol. 8, no. 3, pp. 902–907, 2008.

[36] Changgu Lee, Xiaoding Wei, Jeffrey W Kysar, and James Hone, "Measurement of the elastic properties and intrinsic strength of monolayer graphene," *science*, vol. 321, no. 5887, pp. 385–388, 2008.

[37] S Mohsen Raeis-Zadeh, Behrooz Semnani, and Safieddin Safavi-Naeini, "Plasmon-drag-assisted terahertz generation in a graphene layer incorporating an asymmetric plasmon nanostructure," *Physical Review B*, vol. 94, no. 12, pp. 121411, 2016.

[38] Behrooz Semnani, Amir Hamed Majedi, and Safieddin Safavi-Naeini, "Nonlinear quantum optical properties of graphene," *Journal of Optics*, vol. 18, no. 3, pp. 035402, 2016.

[39] Q. Bao and K.P. Loh, "Graphene photonics, plasmonics, and broadband optoelectronic devices," *ACS nano*, vol. 6, no. 5, pp. 3677–3694, 2012.

[40] F Schedin, AK Geim, SV Morozov, EW Hill, P Blake, MI Katsnelson, and KS Novoselov, "Detection of individual gas molecules adsorbed on graphene," *Nature materials*, vol. 6, no. 9, pp. 652–655, 2007.

[41] Andre K Geim and Konstantin S Novoselov, "The rise of graphene," *Nature materials*, vol. 6, no. 3, pp. 183–191, 2007.

[42] Francesco Bonaccorso, Z Sun, T Hasan, and AC Ferrari, "Graphene photonics and optoelectronics," *Nature photonics*, vol. 4, no. 9, pp. 611–622, 2010.

[43] Kostya S Novoselov, Andre K Geim, Sergei V Morozov, DA Jiang, Y_ Zhang, Sergey V Dubonos, Irina V Grigorieva, and Alexandr A Firsov, "Electric field effect in atomically thin carbon films," *science*, vol. 306, no. 5696, pp. 666–669, 2004.

[44] Xuesong Li, Weiwei Cai, Jinho An, Seyoung Kim, Junghyo Nah, Dongxing Yang, Richard Piner, Aruna Velamakanni, Inhwa Jung, Emanuel Tutuc, et al., "Large-area synthesis of high-quality and uniform graphene films on copper foils," *science*, vol. 324, no. 5932, pp. 1312–1314, 2009.

[45] Kwanghyun Yoo, Yusuke Takei, Bo Hou, Shohei Chiashi, Shigeo Maruyama, Kiyoshi Matsumoto, and Isao Shimoyama, "Direct physical exfoliation and transfer of graphene grown via ethanol chemical vapor deposition," in *Micro Electro Mechanical Systems (MEMS), 2011 IEEE 24th International Conference on*. IEEE, 2011, pp. 99–102.

[46] Nazy Ranjkesh, Mohamed Basha, Aidin Taeb, Alireza Zandieh, Suren Gigoyan, and Safieddin Safavi-Naeini, "Silicon-on-glass dielectric waveguidepart i: For millimeter-wave integrated circuits," *IEEE Trans. THz Sci. Technol.*, vol. 5, no. 2, pp. 268–279, 2015.

[47] Aidin Taeb, Luyao Chen, Suren Gigoyan, Mohamed Basha, Gholamreza Rafi, Sujeet Chaudhuri, and Safieddin Safavi-Naeini, "A silicon image guide (sig) technology platform for high performance sub-millimeter-wave passive structures," in *Microwave Symposium (IMS), 2016 IEEE MTT-S International*. IEEE, 2016, pp. 1–4.

[48] N Ranjkesh, A Taeb, A Abdellatif, S Gigoyan, M Basha, and S Safavi-Naeini, "Millimeter-wave silicon-on-glass integrated technology," in *Microwave and RF Conference (IMaRC), 2014 IEEE International*. IEEE, 2014, pp. 233–236.

[49] Michael H Lim, TE Murphy, J Ferrera, JN Damask, and Henry I Smith, "Fabrication techniques for grating-based optical devices," *Journal of Vacuum Science & Technology B: Microelectronics and Nanometer Structures Processing, Measurement, and Phenomena*, vol. 17, no. 6, pp. 3208–3211, 1999.

[50] CM Sotomayor Torres, S Zankovych, J Seekamp, AP Kam, C Clavijo Cedeno, T Hoffmann, J Ahopelto, F Reuther, K Pfeiffer, G Bleidiessel, et al., "Nanoimprint lithography: an alternative nanofabrication approach," *Materials Science and Engineering: C*, vol. 23, no. 1-2, pp. 23–31, 2003.

[51] C Vieu, F Carcenac, A Pepin, Y Chen, M Mejias, A Lebib, L Manin-Ferlazzo, L Couraud, and H Launois, "Electron beam lithography: resolution limits and applications," *Applied surface science*, vol. 164, no. 1-4, pp. 111–117, 2000.

[52] K Nagashio, T Nishimura, K Kita, and A Toriumi, "Metal/graphene contact as a performance killer of ultra-high mobility graphene analysis of intrinsic mobility and contact resistance," in *Electron Devices Meeting (IEDM), 2009 IEEE International*. IEEE, 2009, pp. 1–4.

[53] Seyoung Kim, Junghyo Nah, Insun Jo, Davood Shahrjerdi, Luigi Colombo, Zhen Yao, Emanuel Tutuc, and Sanjay K Banerjee, "Realization of a high mobility dual-gated graphene field-effect transistor with al 2 o 3 dielectric," *Applied Physics Letters*, vol. 94, no. 6, pp. 062107, 2009.

[54] Yanqing Wu, Yu-ming Lin, Ageeth A Bol, Keith A Jenkins, Fengnian Xia, Damon B Farmer, Yu Zhu, and Phaedon Avouris, "High-frequency, scaled graphene transistors on diamond-like carbon," *Nature*, vol. 472, no. 7341, pp. 74, 2011.

[55] Jingping Liu, Safieddin Safavi-Naeini, and Dayan Ban, "Fabrication and measurement of graphene p–n junction with two top gates," *Electronics Letters*, vol. 50, no. 23, pp. 1724–1726, 2014.

[56] Nazy Ranjkesh, Aidin Taeb, Naimeh Ghafarian, Suren Gigoyan, Mohamed A Basha, and Safieddin Safavi-Naeini, "Millimeter-wave suspended silicon-on-glass tapered antenna with dual-mode operation," *IEEE Transactions on Antennas and Propagation*, vol. 63, no. 12, pp. 5363–5371, 2015.

[57] Hossein Mosallaei and Yahya Rahmat-Samii, "Periodic bandgap and effective dielectric materials in electromagnetics: characterization and applications in nanocavities and waveguides," *IEEE Transactions on Antennas and Propagation*, vol. 51, no. 3, pp. 549–563, 2003.

[58] T Delort and D Maystre, "Finite-element method for gratings," *JOSA A*, vol. 10, no. 12, pp. 2592–2601, 1993.

[59] Guillaume Demésy, Frédéric Zolla, André Nicolet, Mireille Commandré, and Caroline Fossati, "The finite element method as applied to the diffraction by an anisotropic grating," *Optics Express*, vol. 15, no. 26, pp. 18089–18102, 2007.

[60] Hung-Yu David Yang, Rodolfo Diaz, and Nicolaos G Alexopoulos, "Reflection and transmission of waves from multilayer structures with planar-implanted periodic material blocks," *JOSA B*, vol. 14, no. 10, pp. 2513–2521, 1997.

[61] ST Peng, Theodor Tamir, and Henry L Bertoni, "Theory of periodic dielect waveguides," *IEEE transactions on microwave theory and techniques*, vol. 23, no. 1, pp. 123–133, 1975.

[62] ST Peng, "Rigorous formulation of scattering and guidance by dielectric grating waveguides: general case of oblique incidence," *JOSA A*, vol. 6, no. 12, pp. 1869–1883, 1989.

[63] Henry L Bertoni, Theodor Tamir, et al., "Frequency-selective reflection and transmission by a periodic dielectric layer," *IEEE Transactions on antennas and propagation*, vol. 37, no. 1, pp. 78–83, 1989.

[64] J Crisostomo, WA Costa, and AJ Giarola, "Electromagnetic wave propagation in multilayer dielectric periodic structures," *IEEE transactions on antennas and propagation*, vol. 41, no. 10, pp. 1432–1438, 1993.

[65] Angela Coves, Benito Gimeno, Jordi Gil, Miguel V Andrés, AA San Blas, and Vicente E Boria, "Full-wave analysis of dielectric frequency-selective surfaces using a vectorial modal method," *IEEE Transactions on antennas and propagation*, vol. 52, no. 8, pp. 2091–2099, 2004.

[66] John M Jarem and Partha P Banerjee, *Computational methods for electromagnetic and optical systems*, CRC Press, 2016.

[67] Ahmed Mohamed Attiya and Ahmed A Kishk, "Modal analysis of a two-dimensional dielectric grating slab excited by an obliquely incident plane wave," *Progress In Electromagnetics Research*, vol. 60, pp. 221–243, 2006.

[68] Herwig Kogelnik, "Coupled wave theory for thick hologram gratings," *Bell System Technical Journal*, vol. 48, no. 9, pp. 2909–2947, 1969.

[69] MG Moharam, Eric B Grann, Drew A Pommet, and TK Gaylord, "Formulation for stable and efficient implementation of the rigorous coupled-wave analysis of binary gratings," *JOSA a*, vol. 12, no. 5, pp. 1068–1076, 1995.

[70] Jose Ricardo Descardeci and Juan Ramon Mosig, "Simple techniques to enhance convergence of integrals used in the frequency domain moment method for rectangular microstrip antennas," in *Electrotechnical Conference, 2006. MELECON 2006. IEEE Mediterranean*. IEEE, 2006, pp. 310–313.

[71] Krzysztof A Michalski, "Extrapolation methods for sommerfeld integral tails," *IEEE Transactions on Antennas and Propagation*, vol. 46, no. 10, pp. 1405–1418, 1998.

[72] Salvatore Solimeno, *Guiding, diffraction, and confinement of optical radiation*, Elsevier, 2012.

[73] Avraham Gover, "Wave interactions in periodic structures and periodic dielectric waveguides," 1976.

[74] LA Falkovsky and AA Varlamov, "Space-time dispersion of graphene conductivity," *The European Physical Journal B*, vol. 56, no. 4, pp. 281–284, 2007.

[75] and Lars Fritz Markus Muller, Jorg Schmalian, "Graphene: A nearly perfect fluid," *Phys. Rev. B*, vol. 103, no. 2, pp. 025301(4), 2009.

[76] NMR Peres, "Colloquium: The transport properties of graphene: An introduction," *Reviews of Modern Physics*, vol. 82, no. 3, pp. 2673, 2010.

[77] Riichiro Saito, Gene Dresselhaus, Mildred S Dresselhaus, et al., *Physical properties of carbon nanotubes*, vol. 4, World Scientific, 1998.

[78] Andre K Geim and Konstantin S Novoselov, "The rise of graphene," *Nature materials*, vol. 6, no. 3, pp. 183–191, 2007.

[79] MI Katsnelson, KS Novoselov, and AK Geim, "Chiral tunnelling and the klein paradox in graphene," *Nature physics*, vol. 2, no. 9, pp. 620, 2006.

[80] S Das Sarma, Shaffique Adam, EH Hwang, and Enrico Rossi, "Electronic transport in two-dimensional graphene," *Reviews of Modern Physics*, vol. 83, no. 2, pp. 407, 2011.

[81] M. Jablan, H. Buljan, and M. Soljačić, "Plasmonics in graphene at infrared frequencies," *Physical Review B*, vol. 80, no. 24, pp. 245435, 2009.

[82] A. Tsuneya, "Screening effect and impurity scattering in monolayer graphene," *Journal of the Physical Society of Japan*, vol. 75, no. 7, pp. 074716, 2006.

[83] LA Falkovsky and AA Varlamov, "Space-time dispersion of graphene conductivity," *The European Physical Journal B-Condensed Matter and Complex Systems*, vol. 56, no. 4, pp. 281–284, 2007.

[84] LA Falkovsky, "Optical properties of graphene," in *Journal of Physics: Conference Series*. IOP Publishing, 2008, vol. 129, p. 012004.

[85] FT Vasko and V. Ryzhii, "Photoconductivity of intrinsic graphene," *Physical Review B*, vol. 77, no. 19, pp. 195433, 2008.

[86] EH Hwang and S.D. Sarma, "Dielectric function, screening, and plasmons in two-dimensional graphene," *Physical Review B*, vol. 75, no. 20, pp. 205418, 2007.

[87] E.D. Palik, *Handbook of optical constants of solids*, vol. 1, Academic press, 1998.

[88] Gabriele Giuliani and Giovanni Vignale, *Quantum theory of the electron liquid*, Cambridge university press, 2005.

[89] Mikhail Iosifovich Katsnelson, *Graphene: carbon in two dimensions*, Cambridge University Press, 2012.

[90] VF Gantmakher and YB Levinson, *Carrier scattering in metals and semiconductors*, Elsevier, 2012.

[91] R. Bistritzer and A. H. MacDonald, "Hydrodynamic theory of transport in doped graphene," *Phys. Rev. B*, vol. 80, no. 8, pp. 085109(7), 2009.

[92] D Svintsov, V Vyurkov, S Yurchenko, T Otsuji, and V Ryzhii, "Hydrodynamic model for electron-hole plasma in graphene," *Journal of Applied Physics*, vol. 111, no. 8, pp. 083715, 2012.

[93] Rafael Roldán, J-N Fuchs, and MO Goerbig, "Collisionless hydrodynamics of doped graphene in a magnetic field," *Solid State Communications*, vol. 175, pp. 114–118, 2013.

[94] M Mendoza, HJ Herrmann, and S Succi, "Hydrodynamic model for conductivity in graphene," *Scientific reports*, vol. 3, 2013.

[95] Naimeh Ghafarian, Hamed Majedi, and Safieddin Safavi-Naeini, "Millimetre-wave and terahertz amplification in a travelling wave graphene structure," *IEEE Journal of Selected Topics in Quantum Electronics*, vol. 23, no. 1, pp. 179–187, 2017.

[96] Massimiliano Di Ventra, *Electrical transport in nanoscale systems*, vol. 14, Cambridge University Press Cambridge, 2008.

[97] Robert A Alberty, "Use of legendre transforms in chemical thermodynamics (iupac technical report)," *Pure and Applied Chemistry*, vol. 73, no. 8, pp. 1349–1380, 2001.

[98] Nazy Ranjkesh, Mohamed Basha, Aidin Taeb, Alireza Zandieh, Suren Gigoyan, and Safieddin Safavi-Naeini, "Silicon-on-glass dielectric waveguidepart i: For millimeter-wave integrated circuits," *IEEE Transactions on Terahertz Science and Technology*, vol. 5, no. 2, pp. 268–279, 2015.

[99] Nazy Ranjkesh, Mohamed Basha, Aidin Taeb, and Safieddin Safavi-Naeini, "Silicon-on-glass dielectric waveguidepart ii: For thz applications," *IEEE Transactions on Terahertz Science and Technology*, vol. 5, no. 2, pp. 280–287, 2015.

[100] A Yariv and A Gover, "Equivalence of the coupled-mode and floquet-bloch formalisms in periodic optical waveguides," *Applied Physics Letters*, vol. 26, no. 9, pp. 537–539, 1975.

[101] John Robinson Pierce, "Coupling of modes of propagation," *Journal of Applied Physics*, vol. 25, no. 2, pp. 179–183, 1954.

[102] William Henry Louisell, *Coupled mode and parametric electronics*, Wiley, 1960.

[103] Amnon Yariv, "Coupled-mode theory for guided-wave optics," *IEEE Journal of Quantum Electronics*, vol. 9, no. 9, pp. 919–933, 1973.

[104] Dietrich Marcuse, "Mode conversion caused by surface imperfections of a dielectric slab waveguide," *Bell Labs Technical Journal*, vol. 48, no. 10, pp. 3187–3215, 1969.

[105] H Kogelnik and CV Shank, "Coupled-wave theory of distributed feedback lasers," *Journal of applied physics*, vol. 43, no. 5, pp. 2327–2335, 1972.

[106] Harold Stoll and Amnon Yariv, "Coupled-mode analysis of periodic dielectric waveguides," *Optics Communications*, vol. 8, no. 1, pp. 5–8, 1973.

[107] NA Amin, Mohammad Taghi Ahmadi, Zaharah Johari, JF Webb, SM Mousavi, and Razali Ismail, "Drift velocity and mobility of a graphene nanoribbon in a high magnitude electric field," in *Proceedings of the Fourth Global Conference on Power Control and Optimization*. AIP Publishing, 2011, vol. 1337, pp. 177–179.

[108] M Bresciani, A Paussa, P Palestri, D Esseni, and L Selmi, "Low-field mobility and high-field drift velocity in graphene nanoribbons and graphene bilayers," in *Electron Devices Meeting (IEDM), 2010 IEEE International*. IEEE, 2010, pp. 32–1.

[109] Vincent E Dorgan, Myung-Ho Bae, and Eric Pop, "Mobility and saturation velocity in graphene on sio 2," *Applied Physics Letters*, vol. 97, no. 8, pp. 082112–082112, 2010.

[110] A Sv Sudbo, "Improved formulation of the film mode matching method for mode field calculations in dielectric waveguides," *Pure and Applied Optics: Journal of the European Optical Society Part A*, vol. 3, no. 3, pp. 381, 1994.

[111] JE Goell, "A circular-harmonic computer analysis of rectangular dielectric waveguides," *Bell Labs Technical Journal*, vol. 48, no. 7, pp. 2133–2160, 1969.

[112] OV Ivanova, Manfred Hammer, Remco Stoffer, and E Van Groesen, "A variational mode expansion mode solver," *Optical and Quantum Electronics*, vol. 39, no. 10-11, pp. 849–864, 2007.

[113] Arti Vaish and Harish Parthasarathy, "Analysis of a rectangular waveguide using finite element method," *Progress In Electromagnetics Research*, vol. 2, pp. 117–125, 2008.

[114] Edgard Schweig and William B Bridges, "Computer analysis of dielectric waveguides: A finite-difference method," *IEEE transactions on microwave theory and techniques*, vol. 32, no. 5, pp. 531–541, 1984.

[115] Kin Seng Chiang, "Effective-index method for the analysis of optical waveguide couplers and arrays: an asymptotic theory," *Journal of lightwave technology*, vol. 9, no. 1, pp. 62–72, 1991.

[116] Enrique AJ Marcatili, "Dielectric rectangular waveguide and directional coupler for integrated optics," *Bell Labs Technical Journal*, vol. 48, no. 7, pp. 2071–2102, 1969.

[117] Clifford R Pollock and Michal Lipson, *Integrated photonics*, vol. 20, Springer, 2003.

[118] Cavour Yeh and Fred I Shimabukuro, *The essence of dielectric waveguides*, Springer, 2008.

[119] D Marcuse, "Theory of dielectric optical waveguides (academic, new york, 1974)," *Google Scholar*, pp. 181–193.

[120] Robert G Hunsperger and Jurgen R Meyer-Arendt, "Integrated optics: theory and technology," *Applied Optics*, vol. 31, pp. 298, 1992.

[121] Wouter J Westerveld, Suzanne M Leinders, Koen WA van Dongen, H Paul Urbach, and Mirvais Yousefi, "Extension of marcatili's analytical approach for rectangular silicon optical waveguides," *Journal of Lightwave Technology*, vol. 30, no. 14, pp. 2388–2401, 2012.

[122] Aidin Taeb, "A new silicon-based dielectric waveguide technology for millimeter-wave/terahertz devices and integrated systems," 2015.

[123] Nazy Ranjkesh, Hadi Amarloo, Suren Gigoyan, Naimeh Ghafarian, Mohamed Ali Basha, and Safieddin Safavi-Naeini, "1.1 thz u-silicon-on-glass (u-sog) waveguide: A low-loss platform for thz high-density integrated circuits," *IEEE Transactions on Terahertz Science and Technology*, 2018.

[124] Chris Mack, *Fundamental principles of optical lithography: the science of microfabrication*, John Wiley & Sons, 2008.

[125] Kazuo Nojiri, *Dry etching technology for semiconductors*, Springer, 2015.

[126] Franz Laermer, Sami Franssila, Lauri Sainiemi, and Kai Kolari, "Deep reactive ion etching," in *Handbook of Silicon Based MEMS Materials and Technologies (Second Edition)*, pp. 444–469. Elsevier, 2015.

[127] Ji Won Suk, Alexander Kitt, Carl W Magnuson, Yufeng Hao, Samir Ahmed, Jinho An, Anna K Swan, Bennett B Goldberg, and Rodney S Ruoff, "Transfer of cvd-grown monolayer graphene onto arbitrary substrates," *ACS nano*, vol. 5, no. 9, pp. 6916–6924, 2011.

[128] A Pirkle, J Chan, A Venugopal, D Hinojos, CW Magnuson, S McDonnell, L Colombo, EM Vogel, RS Ruoff, and RM Wallace, "The effect of chemical residues on the physical and electrical properties of chemical vapor deposited graphene transferred to sio2," *Applied Physics Letters*, vol. 99, no. 12, pp. 122108, 2011.

[129] Xuelei Liang, Brent A Sperling, Irene Calizo, Guangjun Cheng, Christina Ann Hacker, Qin Zhang, Yaw Obeng, Kai Yan, Hailin Peng, Qiliang Li, et al., "Toward clean and crackless transfer of graphene," *ACS nano*, vol. 5, no. 11, pp. 9144–9153, 2011.

[130] Shaffique Adam, EH Hwang, VM Galitski, and S Das Sarma, "A self-consistent theory for graphene transport," *Proceedings of the National Academy of Sciences*, vol. 104, no. 47, pp. 18392–18397, 2007.

[131] EH Hwang, S Adam, and S Das Sarma, "Carrier transport in two-dimensional graphene layers," *Physical review letters*, vol. 98, no. 18, pp. 186806, 2007.

[132] Runbo Shi, Huilong Xu, Bingyan Chen, Zhiyong Zhang, and Lian-Mao Peng, "Scalable fabrication of graphene devices through photolithography," *Applied Physics Letters*, vol. 102, no. 11, pp. 113102, 2013.

[133] Shishir Kumar, Nikos Peltekis, Kangho Lee, Hye-Young Kim, and Georg Stefan Duesberg, "Reliable processing of graphene using metal etchmasks," *Nanoscale research letters*, vol. 6, no. 1, pp. 390, 2011.

[134] Rene HJ Vervuurt, Bora Karasulu, Marcel A Verheijen, Wilhelmus (Erwin) MM Kessels, and Ageeth A Bol, "Uniform atomic layer deposition of al2o3 on graphene by reversible hydrogen plasma functionalization," *Chemistry of Materials*, vol. 29, no. 5, pp. 2090–2100, 2017.

[135] Xinran Wang, Scott M Tabakman, and Hongjie Dai, "Atomic layer deposition of metal oxides on pristine and functionalized graphene," *Journal of the American Chemical Society*, vol. 130, no. 26, pp. 8152–8153, 2008.

[136] Babak Fallahazad, Seyoung Kim, Luigi Colombo, and Emanuel Tutuc, "Dielectric thickness dependence of carrier mobility in graphene with hfo 2 top dielectric," *Applied Physics Letters*, vol. 97, no. 12, pp. 123105, 2010.

[137] Yong Hyun Park, Mi Hye Kim, Soo Bin Kim, Hae Jun Jung, Kwanbyung Chae, Yeong Hwan Ahn, Ji-Yong Park, Fabian Rotermund, and Sang Woon Lee, "Enhanced nucleation of high-k dielectrics on graphene by atomic layer deposition," *Chemistry of Materials*, vol. 28, no. 20, pp. 7268–7275, 2016.

[138] Bongki Lee, Seong-Yong Park, Hyun-Chul Kim, KyeongJae Cho, Eric M Vogel, Moon J Kim, Robert M Wallace, and Jiyoung Kim, "Conformal al2o3 dielectric layer deposited by atomic layer deposition for graphene-based nanoelectronics," *Applied Physics Letters*, vol. 92, no. 20, pp. 203102, 2008.

[139] Taekyung Lim, Dongchool Kim, and Sanghyun Ju, "Direct deposition of aluminum oxide gate dielectric on graphene channel using nitrogen plasma treatment," *Applied Physics Letters*, vol. 103, no. 1, pp. 013107, 2013.

[140] Bruno Dlubak, Piran R Kidambi, Robert S Weatherup, Stephan Hofmann, and John Robertson, "Substrate-assisted nucleation of ultra-thin dielectric layers on graphene by atomic layer deposition," *Applied Physics Letters*, vol. 100, no. 17, pp. 173113, 2012.

[141] Kirt R Williams and Richard S Muller, "Etch rates for micromachining processing," *Journal of Microelectromechanical systems*, vol. 5, no. 4, pp. 256–269, 1996.

[142] Chi-Fan Chen, Cheol-Hwan Park, Bryan W Boudouris, Jason Horng, Baisong Geng, Caglar Girit, Alex Zettl, Michael F Crommie, Rachel A Segalman, Steven G Louie, et al., "Controlling inelastic light scattering quantum pathways in graphene," *Nature*, vol. 471, no. 7340, pp. 617, 2011.

[143] Dmitri K Efetov and Philip Kim, "Controlling electron-phonon interactions in graphene at ultrahigh carrier densities," *Physical review letters*, vol. 105, no. 25, pp. 256805, 2010.